# Coherent structures from MHD to sub-ion scales in turbulent solar wind

Alexander Vinogradov

## To cite this version:

Alexander Vinogradov. Coherent structures from MHD to sub-ion scales in turbulent solar wind. Plasmas. Sorbonne Université, 2023. English. NNT : 2023SORUS612 . tel-04496391

**HAL Id: tel-04496391**

**https://theses.hal.science/tel-04496391v1**

Submitted on 8 Mar 2024

**HAL** is a multi-disciplinary open access archive for the deposit and dissemination of scientific research documents, whether they are published or not. The documents may come from teaching and research institutions in France or abroad, or from public or private research centers.

L'archive ouverte pluridisciplinaire **HAL**, est destinée au dépôt et à la diffusion de documents scientifiques de niveau recherche, publiés ou non, émanant des établissements d'enseignement et de recherche français ou étrangers, des laboratoires publics ou privés.

THÈSE DE DOCTORAT DE SORBONNE UNIVERSITÉ

Spécialité : Astronomie & Astrophysique
Ecole Doctorale d'Astrophysique d'Île de France ED127

réalisée au LESIA - Observatoire de Paris

présentée par **Alexander Vinogradov**

pour obtenir le grade de :
DOCTEUR DE SORBONNE UNIVERSITÉ

# Coherent structures from MHD to sub-ion scales in turbulent solar wind

soutenue le 5 December 2023
devant le jury composé de :

| | | |
|---|---|---|
| Mme | Laurence Rezeau | Présidente |
| Mme | Annick Pouquet | Rapportrice |
| M. | Marco Velli | Rapporteur |
| M. | Thierry Passot | Examinateur |
| M. | Pierre Lessafre | Examinateur |
| Mme | Olga Alexandrova | Directrice de thèse |
| M. | Anton Artemyev | invité |
| M. | Pascal Démoulin | invité |

# Acknowledgements

I am grateful to Olga Alexandrova for the opportunity to work on this thesis under her supervision. Thanks to her, I have deepened my understanding of the domain, learned how to analyse and present my scientific results concisely.

I greatly appreciate the help of Pascal Demoulin. I enjoyed working with him: his erudition, enthusiasm and passion for physics encouraged me; his empathy made me feel integrated. Overall, Pascal's contribution was crucial for the completion of the thesis.

I would like to thank my colleagues for their participation and valuable input. I have been working with Anton Artemyev since my master's and throughout the PhD thesis - his advises and comments were always helpful, especially regarding the classification of coherent structures. It was a pleasure to meet and discuss my results with André Mangeney, creative, full of ideas. I am grateful to Milan Maksimovic for his comments to improve the article and general support. I enjoyed our friendly and scientific discussions with Arnaud Zaslavsky as well as playing football on Saturdays.

I would like to express my gratitude to the members of the jury committee: Marco Velli, Anick Pouquet, Laurence Rezeau, Thierry Passot, and Pierre Lessafre for reviewing my thesis and providing thoughtful comments.

I am grateful to Thierry Fouchet for his kind assistance as the Director of Doctoral school. Thanks to Goran Greblo and Sudagar Vassin for their help in resolving technical issues seamlessly.

During my thesis I was surrounded by many nice people. In particular Kristina Rackovic-Babic and Étienne Beriot, with whom I shared the office, but also with Erwan Rouille, Emilie Mauduit, Lea Griton, Fillipe Zarka, Nicole Vilmer, Ludvig Klein, Brigitte Schmieder, David Paipa, Adam Boudouma, Ahmed Houeibib, Julien Girard, David Vaz de Mascarenhas, Fernando Gutierrez-Canales, Daniel Reese, Janis Dalbins, Jean-Baptiste Dakeyo, Jessica Martin, Mingzhe Lui, Alan Loh, Pietro Dazzi, Karine Issautier, Pearse Murphy, Zhang Xiang, Claire Baskevitch, Baptiste Cecconi, Carine Briand, Luca Barbieri, Quentin Duchene, Florence Henry. Thank you all for your friendship.

I am also grateful to my parents for their support. I was very happy that you made it to France to attend my defense. Masha, I will always remember the wonderful time we spent together in Paris. Je t'aime! This thesis is just the beginning of my journey in science. A journey of a thousand miles that begins with a first step.

# Contents

# Abstract

Turbulence is a nonlinear process of cross-scale energy transfer in a fluid. The solar wind is an example of a turbulent plasma available for investigation owing to in-situ spacecraft measurements. Solar wind fluctuations are highly irregular and chaotic. Above an incoherent background fluctuations high-amplitude coherent structures, localized in space, are present.

In this thesis we brought a piece of a new knowledge about the properties of coherent structures in the solar wind at close distance from the Sun (0.17 au). We confirm, with Parker Solar Probe (PSP) data, that coherent structures are present not only at MHD and ion scales, but also at sub-ion scales. We could identify these structures thanks to Morlet wavelet transform. For the first time, we apply a multi-scale analysis in physical space from MHD down to sub-ion scales.

Using plasma and magnetic field time profiles, we analyze several events in details. The amplitude of MHD scale coherent structures is high, comparable in magnitude with the local mean magnetic field. We show examples of MHD coherent structures with different geometries, such as current sheets and Alfvén vortices. Some of MHD coherent structures are located within switchbacks or their boundaries. MHD structures contain a number of embedded substructures at ion and sub-ion scales. The latter have smaller amplitudes and are not seen in the raw data, but can be observed after filtration in frequencies and zooming in time. These structures have a typical magnetic field profiles representing an incompressible Alfvén vortex at ion scales and compressible vortex at sub-ion scales. We also study the fragmentation of coherent structures, showing that the number of isolated intermittent events is larger at smaller scales, while the filling factor decrease from 12% at MHD scales to 7% at ion and 6% sub-ion scales.

Another important point of this thesis is a contribution to our understanding of Alfvén vortices. We refined the derivation of an Alfvén vortex model by providing a detailed discussion of the underlying assumptions. We also generalize the model to describe multipole Alfvén vortices. Finally, we explicit how the modes describing multipole vortices of different order could be combined, or not. This provides more general Alfvén vortex solutions than derived before.

Finally, we derive a new method of classification of coherent structures in the solar wind. This method involves the statistical comparison of the observed structures with expectations of models (using the amplitude anisotropy of magnetic fluctuations). The results with PSP data are dominantly consistent with the crossings of the Alfvén vortex model. Only a small fraction of the structures corresponds to current sheets and magnetic holes, in contrast with the previous results of visual classification.

The results presented in this thesis open a new window of turbulence analysis by showing the importance of Alfvén vortices from MHD down to sub-ion scales. It will be worth to extend this study to different types of winds and to different solar distances, in particular to constrain how these vortices are created and how they evolve in the solar wind. Extending the analysis to higher frequencies will also provide information on their dissipation at electronic scales, so their contribution to solar wind heating.

# Résumé

La turbulence est un processus non linéaire de transfert d'énergie à plusieurs échelles dans un fluide. Le vent solaire est un exemple de plasma turbulent que l'on peut étudier grâce à des mesures effectuées in situ par des engins spatiaux. Les fluctuations du vent solaire sont très irrégulières et chaotiques. Des structures cohérentes de grande amplitude, localisées dans l'espace, sont présentes au-dessus d'un fond de fluctuations incohérentes.

Dans cette thèse, nous apportons de nouvelles connaissances sur les propriétés des structures cohérentes dans le vent solaire à une distance proche du Soleil (0.17 au). Nous confirmons, avec les données de la sonde Parker Solar Probe (PSP), que des structures cohérentes sont présentes non seulement aux échelles MHD et ioniques, mais aussi aux échelles sub-ioniques. Nous avons pu identifier ces structures grâce à la transformée en ondelettes de Morlet. Pour la première fois, nous appliquons une analyse multi-échelle dans l'espace physique depuis les échelles MHD jusqu'aux échelles sub-ioniques.

En utilisant les profils temporels du plasma et du champ magnétique, nous analysons plusieurs événements en détail. L'amplitude des structures cohérentes aux échelles MHD est élevée, comparable en magnitude au champ magnétique moyen local. Nous montrons des exemples de structures cohérentes MHD, telles que des nappes de courant et des vortex d'Alfvén. Certaines structures cohérentes MHD sont situées à l'intérieur des switchbacks ou à leurs frontières. Les structures MHD contiennent un certain nombre de sous-structures aux échelles ioniques et sub-ioniques. Ces structures ont un profil de champ magnétique typique d'un vortex d'Alfvén incompressible (à l'échelles cinétique des ions) et d'un vortex compressible (aux échelles sub-ioniques). Nous avons également étudié la fragmentation des structures cohérentes, montrant que les événements intermittents isolés aux petites échelles sont plus nombreux, tandis que le facteur de remplissage diminue de 12% aux échelles MHD à 7% aux échelles ioniques et 6% aux échelles sub-ioniques.

Un autre point important de cette thèse est une contribution à notre compréhension des vortex d'Alfvén. Nous avons affiné la dérivation d'un modèle de vortex d'Alfvén en fournissant une discussion détaillée des hypothèses. Nous généralisons également le modèle pour décrire les vortex d'Alfvén multipolaires. Enfin, nous expliquons comment les vortex multipolaires, décrits par des modes d'ordre différent, peuvent être superposé. Cela permet d'obtenir des solutions plus générales pour les vortex d'Alfvén que celles obtenues précédemment.

Enfin, nous proposons une nouvelle méthode de classification des structures cohérentes dans le vent solaire. Cette méthode implique la comparaison statistique des structures observées avec les attentes des modèles. Les résultats obtenus avec les données PSP sont principalement cohérents avec le croisement par PSP du modèle de vortex d'Alfvén. Seule une petite fraction des structures correspond à des nappes de courant et à des trous magnétiques, contrairement aux résultats précédents obtenus avec une classification visuelle.

Les résultats présentés dans cette thèse ouvrent une nouvelle fenêtre d'analyse de la turbulence en montrant l'importance des vortex d'Alfvén de la MHD jusqu'aux échelles du sub-ioniques. Il sera important d'étendre cette étude à différents types de vents et à différentes distances solaires, en particulier pour contraindre la façon dont ces vortex sont créés et comment ils évoluent dans le vent solaire. L'extension de l'analyse à des fréquences plus élevées fournira également l'information sur leur dissipation aux échelles électroniques, et donc sur leur contribution au chauffage du vent solaire.

# Chapter 1

# Introduction

The corona is the upper layer of the Solar atmosphere. The temperature of the corona is so high ($T \sim 10^6$ K) that the gravity of the Sun cannot confine it. Therefore there is a continuous flow of the plasma expanding into the interplanetary medium. This flow, called the solar wind, is accelerating and exceeds the characteristic speeds of the slow magnetosonic wave at a distance of about 2-4 solar radii, $R_\odot$[1]. It next exceeds the speed of Alfvén waves and fast magnetosonic waves at a distance of about $10 - 20\ R_\odot$. Thus, at larger radial distances, $R \gtrsim 10\ R_\odot$, the solar wind is both supersonic and superalfvénic. More precisely, the speed profile versus distance depends on the type of solar wind. The slow wind accelerates slowly and it has not yet fully reached its maximum speed at 1 au[2], while the faster wind accelerates strongly close to the Sun and reaches a nearly constant speed above $\sim 0.5$ au (Dakeyo et al., 2022). At the distance of 1 au the solar wind speed is ranging from 300 km/s to 800 km/s.

The large-scale structure of the solar wind is determined by the magnetic field in the corona. The latter changes with the phase of the solar cycle which period is about 11 years for activity and about 22 years for its global magnetic field. In Figure 1.1 the solar corona and the properties of the solar wind are shown during three phases of solar activity. The background image of the Sun shows the corona on the solar disc in the extreme ultraviolet observed by the Solar and Heliospheric Observatory (SOHO) spacecraft. Out of the disc, the corona is observed by (i) the Mauna Loa K coronameter (700–950 nm), and (ii) the SOHO C2 white light coronagraph. The white light intensity of the corona is proportional to the plasma density and trace the magnetic field. The superimposed plot shows the solar wind velocity measured by Ulysses at the distance of a few au from the Sun as a function of latitude. The magnetic field polarity measured by Ulysses is shown in color: inward in blue and outward in red, correspondingly.

During the phase of the minimum activity, see Figure 1.1(a), the solar wind can be

---

[1] The Solar radius is $R_\odot \simeq 7 \times 10^5$ km.

[2] The Sun-Earth distance is 1 au $\simeq 1.5 \times 10^8$ km.

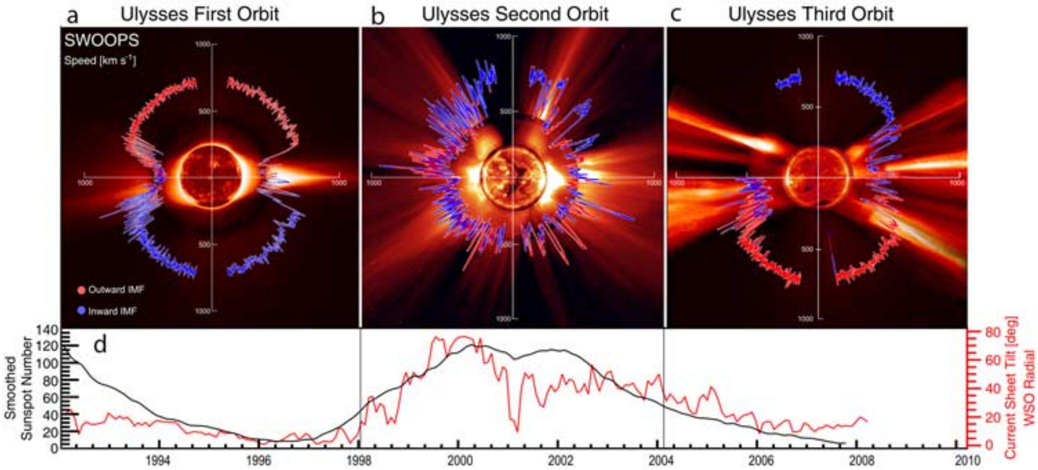

Figure 1.1: Three phases of the Solar cycle: minimum, maximum and a new minimum after the magnetic field inversion. In panels (a-c) the background image shows the solar corona as observed on the disc by the Extreme ultraviolet Imaging Telescope (EIT) on board of the Solar and Heliospheric Observatory (SOHO) spacecraft, and outside the solar disc by the Mauna Loa K coronameter (700–950 nm) and by the SOHO C2 white light coronagraph. The superposed line shows the solar wind velocity as a function of latitude from Ulysses measurements at radial distance $R$ ranging from 1.35 au to 5.4 au. The color of the line indicates the inward (in blue) or outward (in red) direction of the interplanetary magnetic field. Bottom panel shows the number of sunspots as the function of time. Adapted from McComas et al. (2008)

categorised into two different types. At high latitudes ($> 25°$) the solar wind is fast ($V \sim 700$ km/s) and it originates from the large polar coronal holes. At low latitudes ($< 25°$) the solar wind is typically slow ($V \lesssim 400$ km/s). The origin of the slow solar wind is more debated. There are multiple possible sources: from the streamer belt, from the boundaries of coronal holes or from the vicinity of active regions (Rouillard et al., 2021). In the minimum of the solar activity the number of sunspots is small, see panel (d) of Figure 1.1, so the magnetic activity is low with only a few active regions on the Sun at a given time. Then, the solar magnetic field is mainly a dipole with open field at both poles. This explains the observed simple configuration observed around the solar minimum in Figure 1.1(a,c).

The phase of maximum Solar activity is shown in Figure 1.1(b). The structure of the coronal magnetic field becomes complex. Indeed, many magnetic flux tubes emerge at the photospheric level with a dominant bipolar magnetic configuration. They are forming active regions which have typical scales of about $10^5$ km. The strongest magnetic fields are concentrated within active regions and more specifically in sunspots. Then, especially around the solar maximum, the coronal magnetic field has a complex structure with the presence of many magnetic bipoles. This has implications on the sources of the solar wind, with coronal holes forming a complex pattern and extending to lower latitude (even crossing the solar equator). This complexity is shown in panel (b) by the observed extreme ultraviolet emission (on the solar disc) and the scattered white light (outside the solar disc). Both emissions trace the underlying magnetic field since the plasma is mainly frozen-in.

In Figure 1.1(c) the next minimum activity phase of the solar cycle is shown, after the reversal of the solar magnetic field polarity. The plasma emission has retrieved a more organized configuration with nearly radial structures observed at low latitudes (where slow solar wind is present). At higher latitude, two polar coronal holes are formed, with low emissivity as the plasma density is much weaker there. The main difference with the previous solar minimum, panel (a), is the reversal of the magnetic field.

The large-scale coronal observations with coronagraphs, as outside the solar disk in Figure 1.1, and the magnetic field computations of the coronal field from the observed photospheric magnetic field, both give the impression of a nearly radial magnetic field at distances $R \in [3, 30]\ R_{\odot}$. At larger distances, Parker theory predicts the formation of a spiral field due to the solar rotation Parker (1958). This is a simple magnetic field configuration where the magnetic field points outward, or inward, in extended longitude sectors ($\Delta\varphi$ may vary between $10^{\circ}$ and $90^{\circ}$ as a function of solar activity). These magnetic sectors are found with *in-situ* magnetic field measurements. When a spacecraft changes sector, it crosses a large-scale current sheet, that is called *Heliospheric current sheet.* Here, the radial magnetic field component $B_R$ changes sign over the thickness of the current sheet $\simeq 10^4$ km. The Heliospheric current sheet separates long-lasting ($\sim$ days to week at 1 au) sectors of uniform $B_R$ sign.

At shorter time scales ($\sim$ minutes), there are abrupt $B_R$ reversals, at odds with previous simple expectations. These strong magnetic reversals are known as *Switchbacks.* They were first observed by Ulysses spacecraft at $1-5$ au and studied by a number of authors, e.g., Balogh et al. (1999); Yamauchi et al. (2004); Landi et al. (2006); Neugebauer and Goldstein (2013); Matteini et al. (2014). More recently, Parker Solar Probe (PSP) revealed that the Switchbacks are dominant features closer to the Sun (e.g., Bale et al., 2019; Kasper et al., 2019; Krasnoselskikh et al., 2020; Dudok de Wit et al., 2020; Froment et al., 2021).

The sketch in the top panel of the Figure 1.2 shows a simple representation of switchbacks (Bale et al., 2019). The bottom panels show a typical example of a switchback observed by Froment et al. (2021) using PSP data. The radial magnetic field $B_R$ is changing sign from negative to positive at the leading edge of the switchback. The second $B_R$ reversal at $t$ ~23:25:10 UT shows the trailing edge of the switchback. The duration of the switchback is around 120 s, corresponding to the scale of $2 \cdot 10^5$ km.

Important information about the switchbacks can be retrieved from the suprathermal *strahl* (beam) electrons. These energetic electrons are non collisionnal. Since the magnetic field strength decreases with distance from the Sun, the velocity distribution of strahl

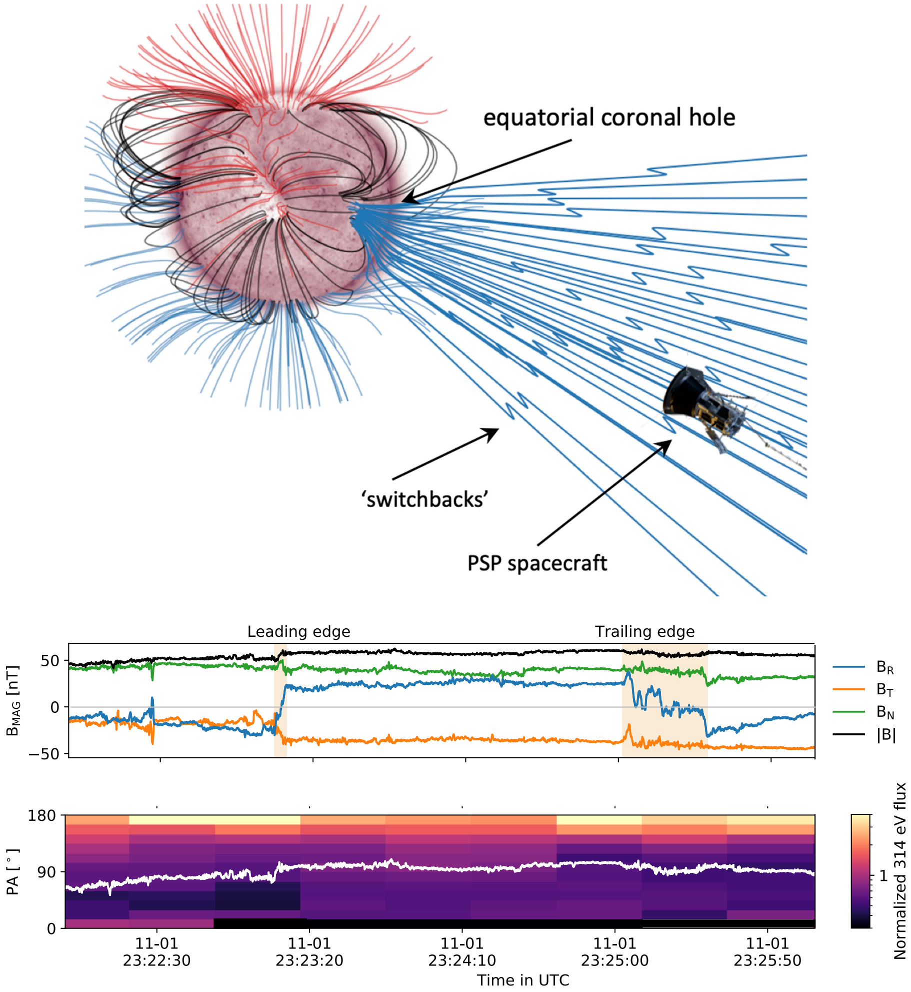

Figure 1.2: The top panel is based on a magnetic field extrapolation of the observed photospheric magnetic field. Magnetic field lines are drawn in blue/red colors according to the magnetic polarity for the open field. The blue field lines are connected to open field region originating from an equatorial coronal hole. The sketch adds up the PSP spacecraft and the field line reversals to illustrate what switchbacks are. This panel is adapted from Bale et al. (2019). The bottom panels show the magnetic field measured by PSP and the normalized pitch angle distribution of 314 eV electrons. It represents the observed energy flux of electrons in function of their velocity inclination angle with respect to the local mean magnetic field $\mathbf{B}_0$ ($0^\circ$ = aligned and $180^\circ$ = anti aligned with $\mathbf{B}_0$). Adapted from Froment et al. (2021).

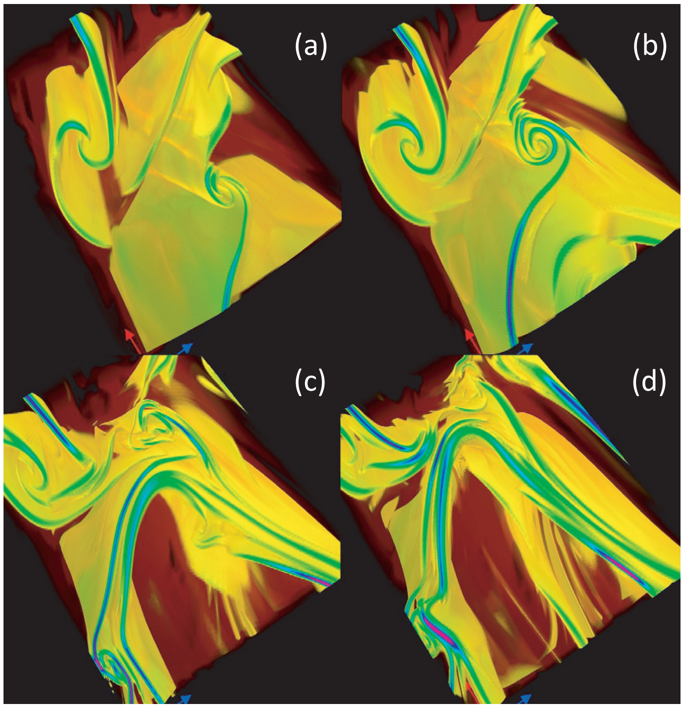

Figure 1.3: The four panels show the evolution of the current density in a direct numerical simulation of high resolution, with $1536^3$ nodes, of MHD turbulence. The time is running from panel (a) to (d) from $t \sim 1.6$ to 2.8 in normalized units, with the initial conditions set at $t = 0$. The current density is shown in color with intensity growing from brown, yellow, green up to blue. The corresponding movie is available at https://stacks.iop.org/NJP/10/125007/mmedia. Adapted from Mininni et al. (2008).

electrons becomes focused along the magnetic field due to conservation of the magnetic moment. The strahl electrons are always propagating anti-sunward along open magnetic field lines, unless they are locally folded backward. Indeed, they are following open field lines outward, propagating always along (or reverse) to the magnetic field. Depending on the polarity of the magnetic field line at the source, the angle between the velocity of the electrons and the magnetic field, called pitch angle, equals to 0° in the case of positive polarity of the magnetic field, or 180° in the case of negative polarity. During the entire interval analysed by Froment et al. (2021), the strahl electrons had a pitch angle of 180° (see an example in the bottom panel of Figure 1.2), so the plasma is connected on the Sun to a region of a negative magnetic polarity. This indicates that the magnetic field reversal is indeed due to the strong bending of the open magnetic lines, as shown in the sketch of the top panel of Figure 1.2, and not to a change of connection to a positive magnetic polarity source on the Sun.

The magnetic field in the solar wind is in fact even more complex than these switchback reversals. The solar wind is known to be turbulent. Fluctuations of different physical quantities, like magnetic and electric fields, velocity, density and temperature form well defined power-law spectra, covering wide range of time scales (or frequencies), e.g., Alexandrova et al. (2013). For example, magnetic fluctuations follow the power low spectrum $\sim f^{-5/3}$ in the range of frequencies $f \in [10^{-3}, 10^{-1}]$ Hz, at 1 au (Coleman, 1968; Kiyani et al., 2009; Bruno and Carbone, 2013). This range corresponds to the MHD inertial range cascade that transfers the energy from large to small scales. We discuss in more details spectral properties of solar wind magnetic fluctuations in Chapter 2 of this manuscript.

MHD simulations of solar wind turbulence with smooth initial conditions show the development of high amplitude localized coherent structures (Sulem et al., 1985; Carbone et al., 1990; Biskamp, 2003). Figure 1.3 is a visualisation of freely decaying MHD turbulence simulation performed by Mininni et al. (2008). It shows the evolution of the coherent structures in time. Panel (a) shows coherent structures in the form of vortices and current sheets that have developed in the simulation by this time. The current sheet (in the bottom) and the vortex (in the center) are non-uniformly advected from the bottom towards the top (panel (b)). The current density increases in the current sheet as it is deformed while still remaining globally stable. The vortex is also stable until it is sandwiched between the almost static current sheet on top and the advected current sheet moving from the bottom (panel (c)). Finally, the vortex is destroyed (panel (d)).

This simulation illustrates several important points about the evolution of coherent structures, which cannot be directly verified *in-situ* with data from a single spacecraft. First, coherent structures can be advected, but remain stable until they encounter and interact with other coherent structures or they get thin enough to reach dissipation scales. Second, there are MHD coherent structures with different geometries: flat or cylindrical. *In-situ* data permit to test these results with 1D cuts though the encountered plasma over a broad range of scales that numerical simulations could not presently achieve. In complement numerical simulations provide the 3D context of the complex temporal evolution, and allow to test the key physical ingredients which are code in.

In this thesis we investigate coherent structures using the Parker Solar Probe measurements in the solar wind at 0.17 au from the Sun.

In Chapter 2 we review the turbulence theories and the associated *in-situ* observational results in the solar wind. First we discuss the spectrum of magnetic fluctuations at 1 au that is naturally divided into frequency ranges corresponding to MHD, ion, and subion scales. Second, we discuss the solar wind intermittency properties which have been known before the present work. Finally we show our results from the first PSP perihelion at 0.17 au from the Sun.

Chapter 3 is devoted to the models of different coherent structures in the solar wind. In Sections 3.1-3.2 we summarize the observational properties of current sheets and magnetic holes. The Alfvén vortices were less investigated so far, then in Section 3.3 we provide a deeper analysis of the equations describing these cylindrical Alfvénic structures with (anti-)aligned current and vorticity. We provide the derivation of the Alfvén vortex model and generalize previous studies to describe the case of multipole vortices. We also clarify when different modes can be superposed.

In Chapter 4, first, we describe the method designed to detect coherent structures in turbulent signal of *in-situ* solar wind data in a wide range of scales (section 4.1). Then, in Section 4.2, we show four examples of embedded coherent structures from MHD to sub-ion scales in the form of sharp discontinuities (current sheets) and vortices. At MHD scales the amplitude of coherent structures is high $\delta B/B_0 \sim 1$, with $B_0$ being the local mean magnetic field. The embedded ion scales structures have amplitudes, which can go up to $\delta B/B_0 \sim 0.4$. At sub-ion scales, the amplitudes are still important for such small scales, $\delta B/B_0 \sim 0.05$. These sub-structures are not seen in the raw data, but can be observed after filtration (in scales or frequencies) and zooming (in time).

In section 4.3, we present statistical study of hundreds to ten thousands of events detected at different scale-ranges (precisely, at MHD, ion, and sub-ion ranges of scales) during the analyzed time interval at 0.17 au. The amplitude anisotropy of magnetic fluctuations and the degree of compressibility allows to determine the dominant type of structures within each range of scales. We also study the fragmentation of coherent structures, (i.e. formation of many secondary sub-structures). We show that the number of isolated intermittent events is larger at smaller scales, while the filling factor is nearly scale independent.

Finally in Chapter 5 we conclude and outline some perspectives.

# Chapter 2

# Statistical properties of the solar wind turbulence

In this chapter first we review the concepts, theories and *in-situ* observations of turbulence in the solar wind. First, we review the main results on the turbulent spectrum. Then, we describe the intermittency properties which are intrinsic to any turbulent flow. Finally, we summarize our results from the first PSP perihelion at the distance of 0.17 au from the Sun.

## 2.1 Turbulent cascade

### 2.1.1 Theoretical prediction of energy spectrum

The first phenomenological description of the turbulence was proposed by Richardson (1922). These ideas were further developed by Kolmogorov (1941), who introduced the first theory of hydrodynamic turbulence. This theory considers the incompressible fluid Navier-Stokes equations:

$$\partial_t \mathbf{V} + \mathbf{V} \cdot \nabla \mathbf{V} = \nabla p/\rho + \nu \nabla^2 \mathbf{V} \tag{2.1}$$

$$\nabla \cdot \mathbf{V} = 0 \tag{2.2}$$

where $\mathbf{V}$, $p$, $\rho$ and $\nu$ are the velocity, pressure, density and viscosity of the fluid, respectively. Let us suppose that the energy is injected to the system at large scales $L$ and that $V$ is the velocity of the injected flow. If the fluid is characterized by a high Reynolds number $R = VL/\nu \gg 1$, the injection scale $L$ is much larger than the dissipation scale $l_d$. The intermediate range of scales ($L > l > l_d$), where the viscous term is negligible compared to the nonlinear term, is called the inertial range. The injected perturbations at scale $L$ evolve nonlinearly causing the transfer (cascade) of the energy to the smaller scales. The ensemble of eddies is formed over the whole inertial range of scales ($L > l > l_d$). Finally the smallest eddies ($l \sim l_d$) are dissipated by the viscous term.

Since turbulent flows are chaotic, the Kolmogorov theory was focused on the statistical properties of the velocity fluctuations. The fluctuations in the vicinity of a point $\mathbf{r}$ can be quantified with the increments of velocity, defined as follows:

$$\delta v(\mathbf{r}, \mathbf{l}) = |\mathbf{v}(\mathbf{r} + \mathbf{l}) - \mathbf{v}(\mathbf{r})| \tag{2.3}$$

where $\mathbf{v}(\mathbf{r}+\mathbf{l})$ and $\mathbf{v}(\mathbf{r})$ are velocities at two points separated by a distance $\mathbf{l}$, with $\mathbf{r}$ defining the spatial location. Kolmogorov assumed that the turbulent fluctuations, associated with eddies, are isotropic and homogeneous, i.e. their statistical properties are invariant with rotation and translation in space. If the eddies of significantly different scales interact, the velocity fluctuation of a larger eddie acts on a smaller one nearly as a uniform sweeping. Therefore it is assumed that only the eddies of similar scales interact nonlinearly. The energy of an eddie of a scale $l$ is transferred to the smaller scales in a nonlinear time which is supposed to be of the order of the eddy turnover time: $\tau_{NL} = l / \langle \delta v(l) \rangle$. The average $\langle ... \rangle$ is taken over the positional argument $\mathbf{r}$. In the stationary state of the turbulent cascade, the scale-to-scale energy transfer rate $\epsilon$ must be constant for $l \in (l_d, L)$ and equal to the dissipation rate at the scale $l_d$. Using the above assumptions, this transfer rate writes

$$\epsilon \sim \langle \delta v(l) \rangle^2 / \tau_{NL} \sim \langle \delta v(l) \rangle^3 / l \, .$$

With $\epsilon$ constant, the theory of Kolmogorov predicts the scaling for velocity fluctuations $\delta v$ (Kolmogorov, 1941; Frisch, 1995):

$$\langle \delta v(l) \rangle \sim l^{1/3} \tag{2.4}$$

It implies that the energy of velocity fluctuations per wavenumber $k = 2\pi l^{-1}$, $E \sim \langle \delta v(l)^2 \rangle / k$, called also power spectrum density) follows:

$$E \sim k^{-5/3} \quad \text{for} \quad L^{-1} < k < l_d^{-1} \quad \text{(inertial range).} \tag{2.5}$$

Similar to neutral fluids, plasmas can also be turbulent. The main difference is the impact of the magnetic field and its coupling to the plasma. The inertial range cascade is established between the energy injection scale $L$ and the dissipation scale $l_d$.

The solar wind is weekly compressible. The amplitude of density fluctuations in the solar wind is 10% of the average density value at the wide range of radial distances (Roberts et al., 1987; Cuesta et al., 2023). So, to a first approximation the inertial range fluctuations in the solar wind can be described by the ideal incompressible MHD equations:

$$\rho(\partial_t + \mathbf{V} \cdot \nabla)\mathbf{V} = -\nabla p + \frac{1}{\mu_0}(\nabla \times \mathbf{B}) \times \mathbf{B} \tag{2.6}$$

$$\partial_t \mathbf{B} - \nabla \times (\mathbf{V} \times \mathbf{B}) = 0 \tag{2.7}$$

$$\nabla \cdot \mathbf{V} = 0 \tag{2.8}$$

$$\nabla \cdot \mathbf{B} = 0 \tag{2.9}$$

where $\mathbf{B}$ is the magnetic field vector.

From the induction equation in the limit of perfectly conducting plasma (Equation (2.7)), so in the inertial range, it can be shown that the movement of the magnetic flux tubes is frozen into the fluid (see, for example, the textbook Landau et al., 1995, §65). Next, in contrast with neutral fluids, the magnetic field strongly impacts the dynamics of the plasma by means of the Lorentz force (the second term on the right side of the momentum Equation (2.6)). The Lorentz force can be expanded as follows:

$$\frac{1}{\mu_0}(\nabla \times \mathbf{B}) \times \mathbf{B} = \frac{(\mathbf{B} \cdot \nabla)\mathbf{B}}{\mu_0} - \nabla \left( \frac{B^2}{2\mu_0} \right) \tag{2.10}$$

where the first term is the magnetic tension and the second term is the gradient of magnetic pressure. The magnetic tension acts as a restoring force for the transverse perturbation of the plasma frozen in the magnetic field. The associated wave mode is known as the Alfvén wave (Alfvén, 1942). Within a magnetized plasma with homogeneous properties ($\mathbf{B}_0$ and $\rho$ constant), an Alfvén wave is following the linear dispersion relation:

$$\omega_A = \pm |k_\parallel| \, V_A \tag{2.11}$$

where $k_\parallel$ is the component of the wave-vector parallel to the magnetic field, and $V_A = \mathbf{B}_0/\sqrt{\mu_0 \rho}$ is the Alfvén speed. The energy of the wave is transported along the background magnetic field, since the group velocity $\mathbf{V}_{gr,A}$ is parallel to $\mathbf{B}_0$:

$$\mathbf{V}_{gr,A} = \frac{\partial \omega_A(\mathbf{k})}{\partial \mathbf{k}} = \pm V_A \, \mathbf{e}_\parallel \tag{2.12}$$

where the positive (negative) sign corresponds to parallel (anti-parallel) propagation, and $\mathbf{e}_\parallel$ is the unit vector along $\mathbf{B}_0$. The fluctuations of the velocity and magnetic field are orthogonal to $\mathbf{B}_0$ and they are correlated as follows:

$$\delta V_\perp / V_A = \pm \delta B_\perp / B_0 \tag{2.13}$$

An Alfvén wave traveling in a uniform background is dispersionless and incompressible. Any Alfvén wave, even with a finite amplitude, is an exact solution of the ideal MHD equations. Because of its dispertionless nature, it can propagate, without changing its shape/waveform, parallel or anti-parallel to the background magnetic field. They do not damp like fast and slow magnetosonic waves (Barnes, 1966, 1979). Solar wind fluctuations reveal a high degree of Alfvénicity, so with Equation (2.13) approximately satisfied (for positive or negative sign). The Alfvénicity is especially prominent in the fast solar wind close to the Sun (Belcher and Davis Jr., 1971; Matthaeus and Goldstein, 1982; Bruno et al., 1985). Alfvénicity is also present in a fraction of the slow solar wind which has characteristics similar to the fast solar wind except that it is slow (e.g. D'Amicis et al., 2019).

Elsässer variables $\mathbf{z}^{\pm}$ are convenient to describe the dynamics of Alfvén waves parallel and anti-parallel to $\mathbf{B}_0$ since $\mathbf{z}^{+}$ (or $\mathbf{z}^{-}$) describes one propagating Alfvén wave. They are defined as follows (Elsasser, 1950; Dobrowolny et al., 1980; Bruno and Carbone, 2013):

$$\mathbf{z}^{\pm} = \mathbf{V} \pm \mathbf{B}/\sqrt{4\pi\rho} \tag{2.14}$$

Using Equation (2.14), MHD Equations (2.6-2.9) can be rewritten in a compact form:

$$\partial_t \mathbf{z}^{\pm} \pm (\mathbf{V}_A \cdot \nabla)\mathbf{z}^{\pm} + (\mathbf{z}^{\mp} \cdot \nabla)\mathbf{z}^{\pm} = -\nabla \cdot P_{tot} \tag{2.15}$$

$$\nabla \cdot \mathbf{z}^{\pm} = 0 \tag{2.16}$$

where $\mathbf{V}_A = \mathbf{B}_0/\sqrt{\mu_0 \rho}$ is the vector of the local Alfvén speed; $P_{tot} = (p + \frac{B^2}{2\mu_0})/\rho$ is the total pressure divided by the mass density $\rho$ (supposed to be constant). The first two terms on the left hand side describe the propagation of finite amplitude Alfvén waves.

The nonlinear term $(\mathbf{z}^{\mp} \cdot \nabla)\mathbf{z}^{\pm}$ does not affect an alone parallel Alfvén wave

$$\mathbf{z}^{-} = f(x - V_A t),\ \mathbf{z}^{+} = 0 \tag{2.17}$$

as well as a single anti-parallel Alfvén wave

$$\mathbf{z}^{-} = 0,\ \mathbf{z}^{+} = g(x + V_A t) \tag{2.18}$$

where $x$ is the coordinate along $\mathbf{B}_0$ and $f, g$ are arbitrary functions. In Equations (2.17) and (2.18), $x$ is the coordinate along $\mathbf{B}_0$. The term $(\mathbf{z}^{\mp} \cdot \nabla)\mathbf{z}^{\pm}$ is responsible for nonlinear interactions between $\mathbf{z}^{+}$ and $\mathbf{z}^{-}$. The interaction of counter-propagating waves via this term leads to the cascade of energy across the scales, so it is essential for the Alfvénic turbulence.

In the plasma turbulence phenomenology (Iroshnikov, 1963; Kraichnan, 1965) the eddies represent Alfvén wave packets. The 'average shape' of the eddies is assumed to be isotropic with respect to the magnetic field, i.e. the longitudal scale and the transverse scales are equal $l_{\perp} = l_{\|} = l$ (this is a strong hypothesis not well satisfied in the solar wind, see below). The magnetic field fluctuation of a large eddie determines the local mean magnetic field $\mathbf{B}_0$ for the smaller eddies, along which they propagate. Then, the nonlinear interaction occurs only between counter-propagating eddies of similar scale $l$ during the Alfvén time $\tau_A = l/V_A$. This time is shorter than the non linear time, $\tau_{NL} = l/\langle \delta v(l) \rangle$, for the fluid case because in the inertial range typically $\langle \delta v(l) \rangle < V_A$ (at most $\langle \delta v(l) \rangle \sim V_A$ in the containing energy range, Matteini et al., 2019). As a result, the scale-to-scale energy transfer rate is reduced compared to the case of an unmagnetized plasma. Each interaction leads to a small distortion of the involved wave packet. So the wave packet decays only after a sequence of $N \sim (\tau_{NL}/\tau_A)^2$ interactions (Biskamp, 1993, chapter 7), where $\tau_{NL}$ denotes the characteristic time taken for the nonlinear term to change the velocity substantially in the absence of magnetic fields. This implies a different slope of the energy spectrum. More precisely, as for velocity increments (Equation (2.3)) one introduces the magnetic field increments:

$$\delta B(l) = |\mathbf{B}(\mathbf{r} + \mathbf{l}) - \mathbf{B}(\mathbf{r})| \,, \tag{2.19}$$

Using the above assumptions, the transfer rate writes

$$\epsilon \sim (\langle \delta v(l) \rangle^2 + \langle \delta B(l) \rangle^2) \,/\, (N \, \tau_A) \sim 2 \langle \delta v(l) \rangle^4 \,/\, (l \, V_A) \,.$$

since in the Iroshnikov-Kraichnan theory the velocity and magnetic field fluctuations follow the same scaling. With $\epsilon$ constant, the theory predicts the scaling for velocity and magnetic fluctuations:

$$\langle \delta v(l) \rangle \sim \langle \delta B(l) \rangle \sim l^{1/4} \sim k^{-1/4} \tag{2.20}$$

and this theory predicts the power energy spectrum, $E \sim (\langle \delta v(l)^2 \rangle + \langle \delta B(l)^2 \rangle) \,/\, k$ :

$$E \sim k^{-3/2} \quad \text{for} \quad L^{-1} < k < l_d^{-1} \quad \text{(inertial range),} \tag{2.21}$$

which is less steep than the Kolmogorov spectrum (Equation (2.5)).

In fact, *in-situ* measurements have shown that the solar wind turbulent fluctuations are anisotropic with respect to the local mean magnetic field $\mathbf{B}_0$ (e.g. Horbury et al., 2008; Podesta, 2009; Wicks et al., 2010). In the Goldreich and Sridhar (1995) model, the eddies are assumed to have different longitudinal scale $l_\parallel$ and transverse scale $l_\perp$ with respect to $\mathbf{B}_0$. There are two characteristic times: the nonlinear turnover time $\tau_{NL} = l_\perp / \delta v_\perp$ and the linear Alfvén time $\tau_A = l_\parallel / V_A$ (i.e. the time of interaction of the counter-propagating Alfvén wave packets). The shape of the eddies is defined from the requirement that those two times are set equal $\tau_{NL} = \tau_A$ (critical balance condition). This assumption implies that the shape of the eddies are more elongated along $\mathbf{B}_0$ at smaller scales. More precisely, assuming Kolmogorov velocity scaling, Equation (2.4), we get that the longitudinal and transverse scales of the eddies follow the scaling $l_\perp \sim l_\parallel^{3/2}$ (a comparable scaling, $l_\perp \sim l_\parallel^{4/3}$, is obtained if the Iroshnikov-Kraichnan theory, Equation (2.20), is rather used). Goldreich and Sridhar (1995) phenomenology predicts that the energy spectrum have different slopes along and across $\mathbf{B}_0$:

$$E_\perp \sim k_\perp^{-5/3}, \quad E_\parallel \sim k_\parallel^{-2} \quad \text{for} \quad L^{-1} < k_\perp, k_\parallel < l_d^{-1} \quad \text{(inertial range).} \tag{2.22}$$

This implies a strongly decreasing energy spectrum along $\mathbf{B}_0$, then the cascade of energy occurs mostly in directions orthogonal to $\mathbf{B}_0$. The discussion of critical balance, and it's limitations can be found in Oughton and Matthaeus (2020).

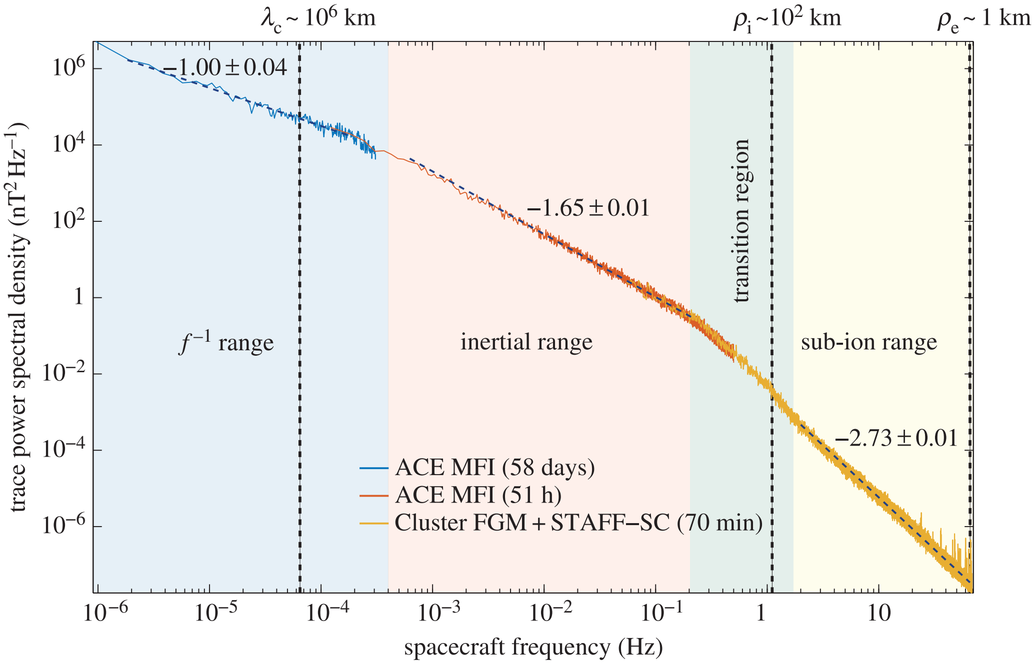

Figure 2.1: Spectrum of the solar wind magnetic fluctuations at 1 au. ACE MFI data during the interval of 58 days are used to cover the $f^{-1}$ range (blue band) and the inertial range (red band) of the spectrum. The high-frequency part of the spectrum, corresponding to ion kinetic scales (green band) and sub-ion scales (yellow band), is obtained from Cluster burst mode measurements (adapted from Kiyani et al., 2015). The top axis shows the spatial scales calculated using Taylor's hypothesis, see Appendix A.

### 2.1.2 Solar wind spectrum at 1 au

An example of spectrum for the magnetic fluctuations in the solar wind at 1 au is shown in Figure 2.1. The spectrum covers a wide frequency range (8 order of magnitude in frequency). Using the Taylor hypothesis, see Appendix A, the corresponding spatial scales are shown in the top of the panel.

In the frequency range $f < 4 \cdot 10^{-4}$ Hz (shown in blue) the magnetic spectrum follows a $f^{-1}$ power law. This range is called the 'energy containing range'. The clear $f^{-1}$ behavior of the spectrum is observed both in the fast solar wind (Bruno et al., 2009) and in the highly Alfvénic slow solar wind (D'Amicis et al., 2019).

There are different suggestions about the origin of the $f^{-1}$ range. Matthaeus and Goldstein (1986) proposed that the $f^{-1}$ results from the superposition of uncorrelated samples of winds with a log-normal distribution of correlation lengths. The samples reflect the features of the turbulence in the solar photosphere. Alternative mechanism could be that the large-scale solar wind inhomogeneities may generate the reflected backward secondary Alfvén waves. Then, their interaction with the primary outcoming waves leads to the $f^{-1}$ spectrum (Velli et al., 1989; Verdini et al., 2012). Another interpretation suggests that the $f^{-1}$ range is related with the low magnetic compressibility Matteini et al. (2019). As known from the solar wind observations, the modulus of the magnetic field is nearly constant $\delta|\mathbf{B}|/B_0 \sim 0$ (Belcher and Davis Jr., 1971). The requirement $|B| = const$ implies that the amplitude of turbulent fluctuations has to saturate at the scale $l$ where $|\delta B(l)|/B_0 \sim 1$. Then, redoing the analysis to deduce Equation (2.21), setting $\langle \delta B(l) \rangle$ independent of $l$ to express the amplitude saturation, leads to $E \sim k^{-1}$. Assuming Taylor hypothesis, the spectrum follows $f^{-1}$. The slow solar wind commonly has a lower power level in the fluctuations and a higher compressibility with respect to the fast wind. Therefore, the theory of Matteini et al. (2019) allows to explain why the $f^{-1}$ range is predominantly observed in the fast solar wind.

At higher frequencies, the spectral slope changes from ≈ -1 to ≈ -1.65 (Figure 2.1). This occurs at a scale comparable to the magnetic field correlation length (Matthaeus et al., 2005). This transition is shown by the vertical dashed line at around $6 \times 10^{-5}$ Hz, or $10^6$ km. This break point corresponds to the largest scale of the inertial range (and the smallest scale of the energy containing range). Comparing the magnetic spectra at different distances from the Sun, the spatial scale corresponding to this spectral break is changing. The scale is larger when measured further away from the Sun (Denskat and Neubauer, 1982; Bavassano et al., 1982; Bruno et al., 2009; Chen et al., 2020).

This observed spectrum evolution was interpreted as follows. In order that the cascade could develops in the inertial range, the typical time for the nonlinear interaction $\tau_{NL} = l/\langle \delta v(l) \rangle$ should be smaller than the expansion time $\tau_{exp} = R/V$ , where $R$ is the radial distance from the Sun, $V$ is the solar wind speed (Mangeney et al., 1991; Salem, 2000). Then, the length $L$ corresponding to the transition between energy containing and inertial ranges is $L \sim R \langle \delta v(L) \rangle / V$. Since $\langle \delta v(L) \rangle \sim V_A$ in the energy containing range (Matteini et al., 2019), then the largest scale of the inertial range, $L$, increases with radial distance as $L \sim R V_A / V$. $V_A$, $V$, are respectively slowly decreasing, increasing, with $R$. Then, $L$ is expected to increase slightly less than $R$. This explains the observed evolution with $R$ of the turbulent spectrum.

The red band in Figure 2.1 shows the inertial frequency range $4 \cdot 10^{-4} < f < 0.2$ Hz. The spectral slope $\alpha_B$ of magnetic fluctuations at 1 au is $\sim -5/3$ as for the Kolmogorov spectrum (Equation (2.5)) and as $E_\perp$ in Equation (2.22) for Goldreich and Sridhar spectrum (Salem, 2000; Podesta et al., 2007; Salem et al., 2009). However, velocity fluctuations at 1 au have a different spectral slope $\alpha_V \sim -3/2$. So surprisingly, $\alpha_B$ is as the fluid spectra of Kolmogorov while $\alpha_V$ is as the magnetized plasma spectrum of Iroshnikov-Kraishnan. Moreover, the spectral indices of velocity and magnetic field fluctuations change with the radial distance from the Sun. Close to the Sun the spectral slope $\sim -3/2$ is observed for both fields (Chen et al., 2020; Wang et al., 2023). At distances $R \gtrsim 0.6$ au from the Sun the spectral slope of the magnetic field is steeper with $\alpha_B \sim -5/3$ or even steeper (Kiyani et al., 2015; Chen et al., 2020; Wang et al., 2023). Extending the study to a larger range of distances $1 < R < 5$ au, Roberts (2010) showed that the spectral slope of the spectrum of velocity fluctuations also changes from $\alpha_V \sim -3/2$ at 1 au to $\alpha_V \sim -5/3$ at 5 au. To the best of our knowledge these spectra evolution with solar radial distance is not understood.

An extra level of difficulty is that, in the solar wind, the inertial range fluctuations are dependent on the level of imbalance between the oppositely directed Alfvén waves. This is quantified by the normalized cross-helicity $\sigma_c$ defined as (Biskamp, 1993, section 7.3):

$$\sigma_c = 2\langle \delta\mathbf{v} \cdot \delta\mathbf{B} \rangle \,/\, \langle \delta\mathbf{v}^2 + \delta\mathbf{B}^2 \rangle \,. \tag{2.23}$$

The fluctuations are also dependent on the difference between the energy of magnetic and velocity fluctuations quantified by the normalised residual energy $\sigma_D$ defined as (Pouquet et al., 1976; Dobrowolny et al., 1980; Biskamp, 1993, section 7.4):

$$\sigma_D = (E_v - E_b)/(E_v + E_b) \,, \tag{2.24}$$

where $E_v$ and $E_b$ correspond to the velocity and magnetic field fluctuation energy. When the cross-helicity $\sigma_c$ of the turbulence is nonzero, it is necessary to take into account the cascades of both energy and cross-helicity (Lithwick et al., 2007; Perez and Boldyrev, 2009). A finite residual energy imbalance also affects the cascade (Schekochihin, 2020).

The models listed above are not sufficient to explain all the variety of observations. In particular they assume equal energy of waves traveling from and to the Sun. Within these models the spectrum of magnetic fluctuations and velocity fluctuations are the same, which does not correspond to observations at 1 au.

The green band in Figure 2.1 shows the transition range, where the spectrum gradually becomes steeper (Leamon et al., 1998). Several authors try to fit this range with a power-law (e.g., Bowen et al., 2020b) but this is not meaningful because of the presence of characteristic scales (as marked in Figure 2.1) as well as a small frequency range (approximately only a decade). The MHD inertial range is limited by ion kinetic scales: ion inertial length $d_i$ for $\beta_i = N_i k T_i/(B^2/2\mu_0) > 1$, or the ion Larmor radius $\rho_i$ for $\beta_i < 1$ (Alexandrova et al., 2013; Chen et al., 2014), where $\rho_i = V_{i\perp}/\omega_{ci}$ is the ion Larmor radius, $V_{i\perp} = \sqrt{2kT_{i\perp}/m_i}$ is the perpendicular ion thermal speed, $\omega_{ci} = \frac{eB}{m_i}$ is the ion cyclotron frequency, $d_i = c/\omega_{pi}$ is the ion inertial length, and $\omega_{pi} = \sqrt{\frac{n_i e^2}{\epsilon_0 m_i}}$ is the plasma frequency.

At the subion scales (i.e. for $l$ between $\rho_i, d_i$ and $\rho_e, d_e$) the spectrum follows a $f^{-2.8}$ power law (Alexandrova et al., 2009, 2012, 2021; Sahraoui et al., 2009; Kiyani et al., 2009; Chen et al., 2010; Sahraoui et al., 2013). This different spectral slope than in the inertial range means that different physics is operating on the turbulent cascade at subion scales. In contrast with the MHD turbulent cascade, where ions and electrons constitute a single fluid, sub-ion scale cascade is maintained by the motion of the electrons described as a magnetized fluid, while ions are static and demagnetized (Schekochihin et al., 2009).

Fluctuations at sub-ion scales are often associated with kinetic Alfvén waves (KAWs) which are the extension of the Alfvén wave mode for $k_\perp \rho_i > 1$ (Hasegawa and Chen, 1976;

Hollweg, 1999; Howes et al., 2006). In contrast with the Alfvén waves, KAWs are compressible, so the magnetic field magnitude is fluctuating. The degree of compressibility depends on $\beta_i$ and $\beta_e$ (ratio of ion and electron pressure, respectively, to magnetic pressure) (Schekochihin et al., 2009). There is a good correspondence between the observed compressibility of the magnetic field and the compressibility of oblique ($k_\perp \gg k_\|$) KAWs (Salem et al., 2012; Lacombe et al., 2017; Matteini et al., 2020). In Grošelj et al. (2019), kinetic scale fluctuations were studied using MMS and Cluster data and in 3D fully kinetic simulations. The spectral field ratios $\delta n/\delta b_\|$, $\delta n/\delta b_\perp$ and $\delta b_\|/\delta b_\perp$ as a function of $k_\perp d_i$ are analyzed for time intervals selected by the level of the local intermittency measure, LIM. As the LIM threshold increases, the spectral field ratios progressively differ, but only slightly, from the asymptotic prediction for KAWs. Thus, the authors conclude that KAW features are not exclusively limited to low-amplitude fluctuations but also valid for the high-amplitude ones. On this basis the authors claim that the kinetic turbulence cannot be described as a mixture of mutually exclusive waves and structures.

However, the KAWs are not the only possible explanation of these observations. The observed spectral ratio $\delta n/\delta b_\|$ at the sub-ion scales $k_\perp d_i \in (\sim 1, 10)$ is related to the pressure balance, see Eq. (6) in (Grošelj et al., 2019). Pressure balance is not an exclusive feature of KAW, but it is also fulfilled for mirror structures or kinetic slow modes and compressible Alfvén vortices (Jovanović et al., 2020). Another spectral ratio, $\delta b_\|/\delta b_\perp$, represents the magnetic compressibility. The $\delta b_\|/\delta b_\perp$ observed in (Grošelj et al., 2019) can be explained by the Hall effect for highly oblique wavevectors in the sub-ion range Matteini et al. (2020) (Section 5.1). These conditions are fulfilled, in particular, for the ion-scale Alfvén vortices (Jovanović et al., 2020), which are well defined coherent structures and not wave packets. Therefore, the conclusion of (Grošelj et al., 2019), that the subion-scale turbulent structures may be viewed as KAW wave packets is questionable.

The alternative point of view is that coherent structures are dominant at sub-ion scales. In favor of this idea, Papini et al. (2021) found in 2D Hall-MHD simulations, and then confirmed in 3D simulations (Papini et al., 2022), that most of the energy of subion-scale fluctuations is stored in localised coherent structures, while the energetic contribution of kinetic Alfvén waves is minor. This finding is in agreement with observational results where sub-ion scale current sheets have been found (Perri et al., 2012; Greco et al., 2016).

On scales of the order of the electron Larmor radius $l \sim \rho_e$, the spectrum changes from a power law to an exponential decrease (Alexandrova et al., 2009, 2012, 2021). This indicates that dissipation finally occurs on electron scales. The energy of turbulent fluctuations is transformed to heat, preventing the solar wind from cooling adiabatically as it expands away from the Sun (Coleman, 1968; Vasquez et al., 2007b; Hellinger et al., 2011; Smith and Vasquez, 2021). The precise mechanism of the dissipation is currently an open question. Several possible dissipation mechanisms are invoked, such as cyclotron damping, e.g., (Cranmer, 2000), Landau damping, e.g., (Leamon et al., 1999; Gary and Borovsky, 2004; Cranmer et al., 2007), magnetic reconnection, e.g., (Osman et al., 2011; Karimabadi et al., 2013), stochastic heating (McChesney et al., 1987; Johnson and Cheng, 2001; Chaston et al., 2004; Voitenko and Goossens, 2004; Chandran et al., 2010, 2013; Vech et al., 2017; Hoppock et al., 2018).

In the above models of the cascade, an unrealistic idealization of magnetized plasma is the use of both the self-similarity and homogeneity assumptions. Below, we describe the presence of coherent structures and the related intermittency effects.

## 2.2 Intermittency in turbulence

### 2.2.1 Theoretical background

The theories discussed above, in sub-Section 2.1.1, implicitly assume that the turbulence is spatially homogeneous and statistically self-similar at the different scales of the inertial range. However in neutral fluids (e.g., Frisch, 1995) as well as in the solar wind (e.g., Sorriso-Valvo et al., 1999) the turbulence shows a significant spatial structuration as well a departure from self-similarity, that is manifested in observations as the non-Gaussianity of turbulent fluctuations, e.g., (Bruno and Carbone, 2013; Matthaeus et al., 2015; Benzi and Toschi, 2023). This is related to the intermittency of the signal.

Intermittency can be defined as the irregular distribution of fluctuations in a turbulent medium associated with the formation of coherent structures localized in space and/or with complex patterns of energy dissipation (Carbone and Pouquet, 2009; Matthaeus and Velli, 2011). The standard tool to characterise the intermittency in hydrodynamics is the structure function $S_v^p(l)$ of velocity increments:

$$S_v^p(l) = \langle |v(r+l) - v(r)|^p \rangle \tag{2.25}$$

where $p = 0, 1, 2...$ is the order of the structure function. The average $\langle ... \rangle$ is taken over $\mathbf{r}$ and $l$ defines the analyzed scale.

In Kolmogorov (1941) model (in absence of intermittency) the structure functions follow the scaling:

$$S_v^p(l) = C\,\epsilon^{p/3}\,l^{p/3} \tag{2.26}$$

where $C$ is a constant, and $\epsilon$ is the global energy transfer rate.

The refined self-similarity hypothesis allows to include intermittency into the turbulent cascade model with an energy transfer $\epsilon(\mathbf{r})$ which is strongly dependent on the spatial location $\mathbf{r}$ (Kolmogorov, 1962). The scaling of the structure functions is refined as follows

$$S_v^p(l) = C\,\langle \epsilon(\mathbf{r})^{p/3} \rangle\, l^{p/3} \;=\; C\,\langle \epsilon(\mathbf{r}) \rangle^{p/3}\, l^{p/3-\xi(p)} \tag{2.27}$$

where the second equality takes into account a power law scaling with $l$. Equation (2.27) differs from the scaling of the structure functions in absence of intermittency (Equation (2.26)) since $\epsilon(\mathbf{r})$ is not uniform. The exponent $\xi(p)$ is the intermittency correction. When

$\xi(p)$ is linear in $p$, this is usually interpreted as mono-fractal behavior of turbulent fluctuations. While non-linearity of $\xi(p)$ is usually interpreted as multi-fractal cascade (Horbury and Balogh, 1997; Bruno and Carbone, 2013).

In order to obtain a specific form of $\xi(p)$, we need to make an additional assumption on the statistical properties of $\epsilon(\mathbf{r})$, as follows. In the so-called $\beta$ model it is assumed that the spectral energy transfer $\epsilon(\mathbf{r})$ is concentrated in small active regions (Frisch et al., 1978). The fraction of space where the cascade is active is decreasing from larger to smaller scales as a power of $l$ (Frisch, 1995; Biskamp, 1993). More precisely, at each step of the cascade, an eddie of scale $l_n$ splits into $2^D\beta$ eddies of scale $l_{n+1} = l_n/2$, $D = 3$ is the spatial dimension. Then, only a fraction $0 \leq \beta \leq 1$ of the volume is filled by the smaller eddies. Including this assumption to the model of hydrodynamic turbulent cascade, the scaling of the velocity structure function is modified as follows:

$$S_v^p(l) = C\,\epsilon^{p/3}\,l^{(p-\delta(p-3))/3} \tag{2.28}$$

where $\delta$ is related to the fractal dimention $D_F = D - \delta$, and $\beta = 2^{-\delta}$ is the intermittency parameter, with $\delta = 0$ for the original self-similar Kolmogorov model. In the simple $\beta$ model, the structure exponents depend linearly on the order of the structure functions. But in multifractal intermittency models, the dependence is nonlinear.

Next, there are different ways to include intermittency in an hydrodynamic cascade. For example in the $\mathcal{P}$-model (Meneveau and Sreenivasan, 1987) the energy distribution between the daughter eddies is assumed unequal. Rather, the model of She and Leveque (1994) is using an assumption on the geometry of the smallest dissipative structures supposing that they are essentially one-dimensional filaments. Further information are given in the reviews of Biskamp (1993, Chapter 7.7) and Bruno and Carbone (2013).

Similar developments can be applied to the turbulence models of magnetized plasma. The structure function of magnetic increments is defined in the same way as for velocity (Equation (2.25)):

$$S_b^p(l) = \langle |B(r+l) - B(r)|^p \rangle \tag{2.29}$$

In the Alfvénic turbulence model of Iroshnikov (1963) and Kraichnan (1965), so in the absence of intermittency, the velocity and magnetic field fluctuations are coupled and therefore the velocity and magnetic field structure functions follow the same scaling:

$$S_b^p(l) \sim S_v^p(l) \sim\, l^{p/4} \tag{2.30}$$

In Ruzmaikin et al. (1995) this model is refined using the same assumptions as in the hydrodynamic $\beta$ model of Frisch et al. (1978). Next, an extension analogous to the $\mathcal{P}$-model of Meneveau and Sreenivasan (1987) has been proposed by Carbone (1993). Finally, Grauer et al. (1994) proposed an extension of the original model where the smallest dissipative structures in the MHD inertial range are current sheets. All these models have been critically reviewed in Marsch and Tu (1997) and Horbury and Balogh (1997).

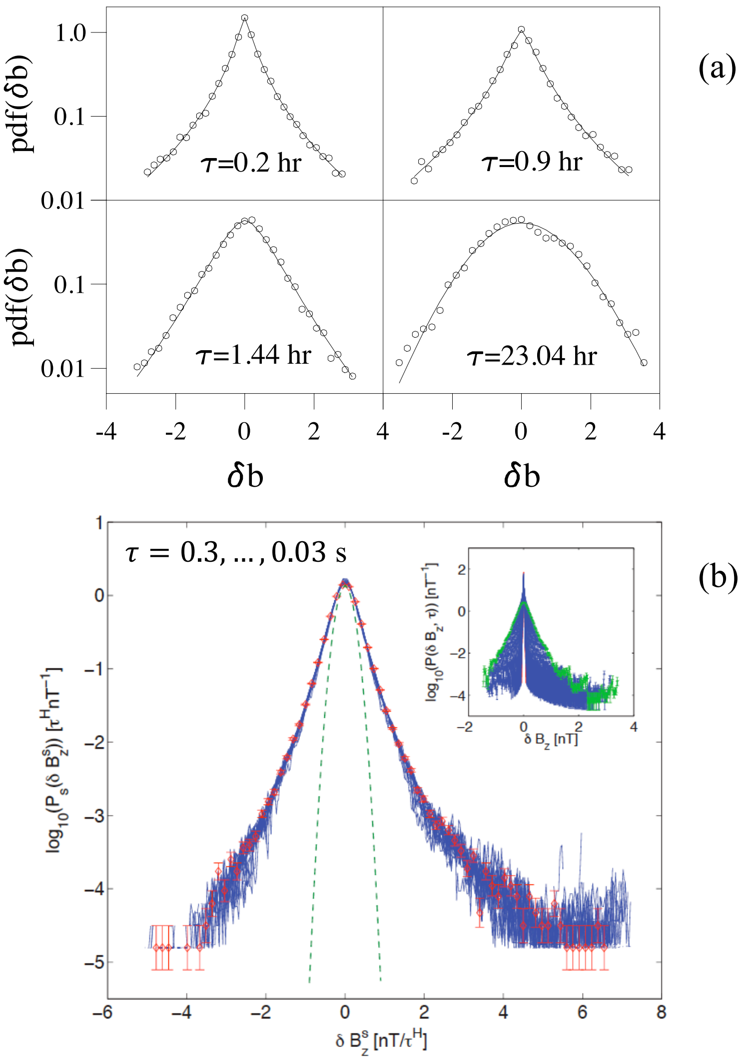

Figure 2.2: Panel (a): Distributions of the magnetic field increments, defined in Equation (2.19) but rewritten with the time $t$ and the time lag $\tau$ (replacing $\mathbf{r}$ and $\mathbf{l}$ respectively). These distributions are normalized by $[\langle \delta B_\tau^2 \rangle]^{1/2}$. Four time lags $\tau$, corresponding to the inertial range, are shown. Adapted from Sorriso-Valvo et al. (1999). Panel (b) main plot: distributions of sub-ion scale magnetic field increments rescaled in accordance with Equation (2.31): $\delta B_z^s = \delta B_z \tau^{-h}$. The inset shows the distributions before rescaling. Adapted from Kiyani et al. (2009).

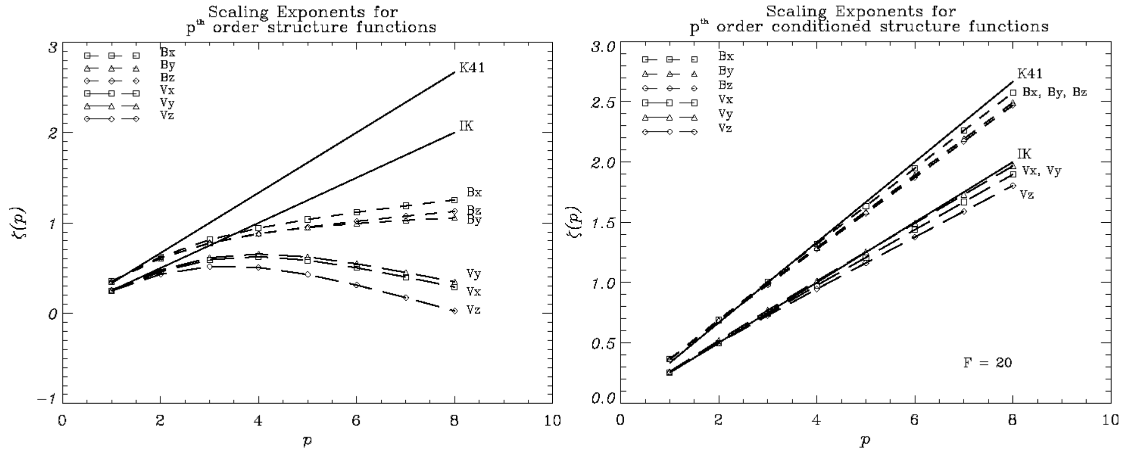

Figure 2.3: Left panel: the scaling exponents for the magnetic field and velocity structure functions. Right panel: conditioned structure exponents for the incoherent component of the signal. The term "conditioned" means that they are computed after removing the wavelet coefficients above the threshold, called F in the right panel, of 20 standard deviations for the fluctuation distribution. This implies that the coherent structures, with large deviation to the mean, are removed. Solid dashed lines in both panels show the prediction of the Kolmogorov (1941) model (Equation (2.26)), as well Iroshnikov (1963) and Kraichnan (1965) model (Equation (2.30)). The figure is adapted from Salem et al. (2007).

### 2.2.2 Intermittency in observations at 1 au

So far, intermittency in the solar wind has been mostly analyzed with *in-situ* observations at 1 au. We summarize below the main findings.

Figure 2.2(a), adapted from Sorriso-Valvo et al. (1999), shows distributions of the magnetic field increments in the solar wind at 1 au. The distributions are shown for 4 different time lags $\tau$ corresponding to scales $l$ in the inertial range. The distribution is Gaussian at the large scales ($\tau = 23$ h). At smaller scales of the inertial range ($\tau = 0.2$ h) non-Gaussian tails of the distribution are easily seen. This different shape of distribution functions of increments is usually interpreted as a signature of multi-fractal cascade.

At sub-ion scales the distributions of magnetic increments are also non-Gaussian, see Figure 2.2(b) inserted panel. Kiyani et al. (2009), at 1 au, and Chhiber et al. (2021), at 0.17 au, found that the distributions at different lags $\tau$ tend to a single function after applying the rescaling operation. In this case the authors rescale the statistics of the fluctuations in the following way:

$$\mathrm{PDF}(\delta B(\lambda\tau)) = \lambda^{h}\,\mathrm{PDF}\left(\delta B(\tau)\right) \tag{2.31}$$

where the scaling exponent $h$ is constant. This is one of the property of mono fractality. Rescaled distribution functions are shown in Figure 2.2(b) main plot. This means that subion scale fluctuations demonstrate non-Gaussian mono-fractal behavior.

A complementary approach is to study the structure functions. Figure 2.3 (left panel) shows, with dashed lines, the exponents of the velocity and magnetic field structure functions in the solar wind (Salem et al., 2007). For small $p$, the exponents increase with the order $p$ of the structure functions. For $p = 1$ and 2, scaling exponents of magnetic field structure functions are close to the linear prediction of the Kolmogorov (1941) model (Equation (2.26), shown with a solid line) and velocity exponents approach the Iroshnikov (1963) and Kraichnan (1965) model (Equation (2.30), solid line). However deviation between the observational curves and the models becomes apparent for structure function exponents of higher orders, $p \geq 3$. Different multifractal intermittency models can fit this nonlinear dependence $\xi(p)$ observed in the solar wind (these fits are not shown here, see for example the review of Horbury and Balogh (1997)). However among these models there is no model explaining better the observational results (Carbone et al., 1996; Bruno and Carbone, 2013).

Along with the above intermittency theories, the modern perception that intermittency means the presence of coherent structures has emerged, e.g., Frisch (1995); Veltri (1999). Hada et al. (2003) showed that the solar wind fluctuations are not random phased, but have a certain level of coherence. Using the wavelet techniques (Farge, 1992; Farge and Schneider, 2015; Lion et al., 2016), turbulent signal can be decomposed into the sum of coherent and incoherent components. The first corresponds to the high-amplitude localised in space events, known as coherent structures.

Figure 2.3 (right panel) shows the exponents of the conditioned structure functions. By 'conditioned' Salem et al. (2007) mean that the most energetic coherent structures are removed before computing the structure functions. Specifically, the Haar wavelet transform has been applied, then the standard deviations of the wavelet coefficients at each scale are used to select and remove the values higher than 20 standard deviations. In this way, the strongest intermittent events are removed, hence the term 'conditioned'. After applying this procedure, the exponents of the structure functions have a linear dependence on the order of the structure function $p$, as in models without intermittency. Therefore, surprisingly, the intermittency is due to the coherent structures that occupy a small fraction of the volume. The strongest events removed by Salem et al. (2007) occupy only $\sim 0.1$ to 1% of the volume depending if the structures are 2D or 3D. In conclusion, the multifractality is associated to the coherent structures. Taking them off, the monofractal scaling is observed.

Still, after removing the coherent structures, the magnetic field and velocity scaling exponents of the structure functions have different slopes (Figure 2.3 right panel). Magnetic fluctuations follow almost the Kolmogorov scaling, while velocity fluctuations fit the Iroshnikov-Kraishnan prediction. This difference, between properties of magnetic and velocity turbulent fluctuations observed in the solar wind, is still an open question.

To conclude, multifractal intermittency models are able to explain the observed nonlinear dependence of the structure functions exponents on the order of the structure function $p$. But, these models are based on phenomenological assumptions, and not on the governing physical Equations (2.6 - 2.9), so they are limited and insufficient. In contrast, the concept of coherent structures necessitates additional studies of their properties and formation.

In the following of this chapter, we summarize our results on statistical properties of turbulence (spectra and intermittency) as observed with Parker Solar Probe (PSP) at 0.17 au.

## 2.3 PSP results during the first perihelion

In this section we present statistical properties of turbulent magnetic field measurements of PSP during 5 hours time interval at 0.17 au. We analysed the time interval on November 6, 2018, [00:00, 05:00] UT during the first encounter, E1, of PSP with the Sun. We select this time interval because, (i) PSP is in the closest point to the Sun (perihelion) for this encounter; (ii) only for E1, there are merged data (Bowen et al., 2020a) of two magnetic field instruments MAG and SCM[1], that allow to study turbulent magnetic field from inertial scales to sub-ion scales.

The magnetic field during the chosen time interval is particularly highly-disturbed due to the presence of high-amplitude structures (including switchbacks, Bale et al., 2019; Perrone et al., 2020). The duration of the chosen interval is long enough to resolve the inertial range of MHD turbulence but short to see the $f^{-1}$ domain. During this time interval, PSP is nearly at the same radial distance from the Sun (0.17 au) and it is magnetically connected to the same coronal hole (Bale et al., 2019).

### 2.3.1 Spectra at 0.17 au

The spectrum of the selected time interval is shown in Figure 2.4(a). The orange line shows the total magnetic field power spectrum (also called Power Spectral Density or PSD):

$$E_{\text{total}}(f) = E_{B_R}(f) + E_{B_T}(f) + E_{B_N}(f), \tag{2.32}$$

where the spectrum of each component, $E_i(f)$, is calculated using Morlet wavelet coefficients, as was done, e.g., in Equation (2) of Alexandrova et al. (2008). In the studied time interval, this spectrum follows $\sim f^{-1.55}$ within the inertial range $10^{-2} < f < 1$ Hz, in agreement with previous studies close to the Sun (Chen et al., 2020; Wang et al., 2023). The ion transition range takes one decade in frequencies: it is observed nearly between the ion cyclotron frequency $f_{ci} = eB/2\pi m_i = 1.4$ Hz and the frequency of the Doppler-shifted ion gyroradius $f_{\rho i} = V/2\pi\rho_i = 11.4$ Hz, $V = 350$ [km/s] denotes the solar wind speed

---

[1] For later encounters, such data are not available because of a problem on one of the SCM axis, see https://fields.ssl.berkeley.edu/data/

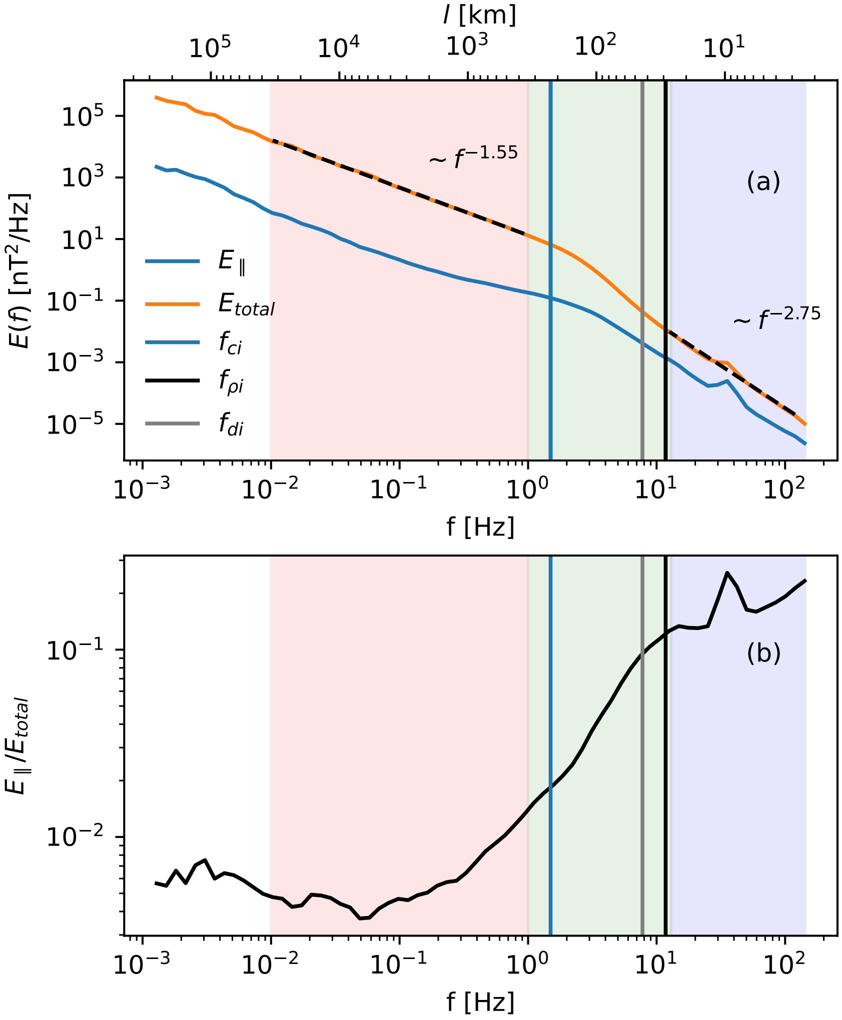

Figure 2.4: Results from PSP first perihelion. From top to bottom: (a) magnetic field total spectrum $E_{total}$ in orange and magnetic field modulus spectrum computed with the parallel fluctuations spectrum $E_{\|}$ (Equation (2.36)), and (b) the ratio $E_{\|}/E_{total}$. The vertical lines show the characteristic ion scales: ion cyclotron frequency $f_{ci}$ (in blue), and the frequencies computed with the Doppler shifted ion gyroradius $f_{\rho i}$ (in black) and the Doppler shifted ion inertial length $f_{di}$ (in grey). The frequency ranges are highlighted: MHD in red, ion scales in green and sub-ion scales in blue (Vinogradov et al., 2023).

(Figure 2.4). The frequency of the Doppler-shifted ion inertial length $f_{di} = V/2\pi d_i$ is in between these two frequencies. At $f > 13$ Hz (sub-ion scales), the spectral index stabilizes at $-2.75$, in agreement with what is observed at 0.3 and 1 au between proton and electron scales (Alexandrova et al., 2009; Chen et al., 2010; Alexandrova et al., 2012, 2021).

Based on the magnetic field spectral properties and characteristic plasma scales ($f_{ci}$, $f_{\rho i}$ and $f_{di}$) we define the following frequency ranges $\Delta f_j$, shown as transparent color bands in Figure 2.4:

$$\Delta f_j = \begin{cases} (10^{-2}, 1) \text{ Hz} & \text{MHD inertial range (in red)} \\ (1, 13) \text{ Hz} & \text{ion scales (in green)} \\ (13, 128) \text{ Hz} & \text{sub-ion range (in blue)} \end{cases} \tag{2.33}$$

The corresponding timescale ranges $\Delta\tau_j$ are

$$\tau_j : \begin{cases} \tau_{MHD} = (1, 100) \text{ s} \\ \tau_{ion} = (0.08, 1) \text{ s} \\ \tau_{subion} = (0.008, 0.08) \text{ s} \end{cases} \tag{2.34}$$

We investigate the compressibility of the magnetic fluctuations at different scales. Compressive fluctuations are approximated by the variation of the magnetic field modulus. This approximation is valid if the level of the fluctuations is significantly lower than the mean field $B_0$, i.e., $\delta B/B_0 \ll 1$. In this case, we have (Perrone et al., 2016):

$$\delta(|B|^2) = |\mathbf{B}_0 + \delta\mathbf{B}|^2 - |\mathbf{B}_0|^2 \approx 2\delta B_{\|} B_0 \approx \delta(B_{\|}^2) \tag{2.35}$$

In the inertial range and at higher frequencies the condition $|\delta B|/B_0 < 1$ is valid. So we calculate the parallel Power Spectral Density (PSD), $E_{\|}(\tau)$, as it was done in Perrone et al. (2016):

$$E_{\|}(\tau) = \frac{2\delta t^2}{T'} \sum_{t \in T'} |W[|B|](t, \tau)|^2 \tag{2.36}$$

In the above Equation 2.36, $W[|B|]$ denotes the wavelet transform of the magnetic field magnitude $|B|$, $\delta t$ is the time step, $T' =$ [00:22:49, 04:37:11] UT is the time interval, where the wavelet coefficients at the scales $\tau < \tau_{max} = 10^3$ s are not influenced by the edge effect, see Appendix B.

The PSD of compressive magnetic fluctuations, $E_{\|}$, is shown in Figure 2.4(a) with a blue line. The ratio of compressible fluctuations to the total PSD, $E_{\|}/E_{total}$, is shown in Figure 2.4(b). In the inertial range, parallel magnetic fluctuations are much less energetic than perpendicular ones ($\delta B_{\|} \ll \delta B_{\perp}$), as is usually observed in the solar wind. Then, $E_{\|} \ll E_{total}$, and $E_{total}(f)$ is nearly equal to $E_{\perp}(f)$. At the sub-ion scales, the fraction of the parallel $E_{\|}(\tau)/E_{total}(\tau)$ increases. This result is consistent with the results of Salem et al. (2012) and Lacombe et al. (2017) at 1 au.

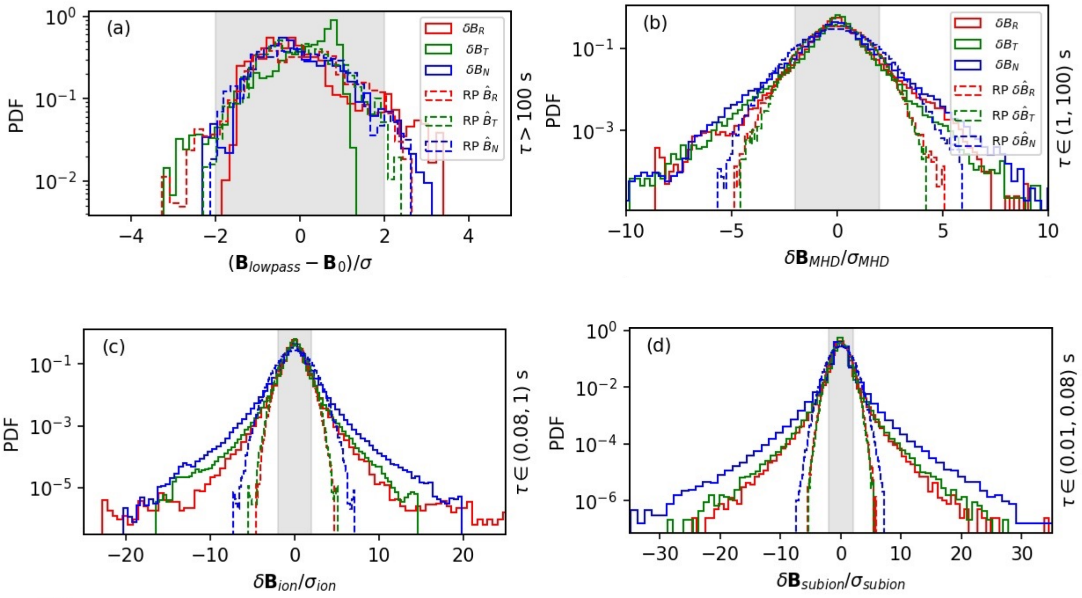

Figure 2.5: Histograms of magnetic field fluctuations (solid) compared to the signal with random phases (RP, dashed) for PSP data at 0.17 au. Panel (a) shows the centered lowpass-filtered fluctuations of the magnetic field. Panels (b-d) show bandpass-filtered fluctuations on MHD inertial, ion kinetic, and sub-ion scales, respectively. The horizontal axis is normalized to the standard deviation of the random-phased signal. The area within two standard deviations of the random-phased signal is highlighted in gray (Vinogradov et al., 2023).

### 2.3.2 Intermittency at 0.17 au

Studies of intermittency in the solar wind typically perform a statistical analysis of fluctuations properties. A simple way to quantify non-Gaussianity of fluctuations at a given scale is to calculate the kurtosis (or flatness) of their distribution. The kurtosis $\kappa_X$ of a random variable $X$ is defined with the normalized fourth moment:

$$\kappa_X = \frac{\langle X^4 \rangle}{\langle X^2 \rangle^2} \tag{2.37}$$

For a Gaussian distribution $\kappa_X = 3$. If the distribution has non-Gaussian tails, $\kappa_X > 3$.

The aim of this work is to identify coherent structures (or intermittent structures), responsible for the observed non-Gaussianity. Since intermittent structures have coupled phases across a wide range of scales, see (Lion et al., 2016) or (Vinogradov et al., 2023, Figure 3, see Appendix E), we decide to consider turbulent fluctuations within ranges of scales, defined in Equation (2.34) and not at a fixed scales, as it is usually done. Figure 2.5 shows the result of this approach. Panel (a) represents the distribution of the low-pass magnetic field components with their mean values subtracted. Panel (b) gives PDF's of magnetic fluctuations $\delta B_i$ (with $i = R, T, N$) at MHD sales $(1, 100)$ s, panel (c) gives the same representation but for ion sales $(0.08, 1)$ s and (d) gives PDF's of $\delta B_i$ at sub-ion scales $(0.008, 0.08)$ s. Solid lines corresponds to observations and dashed lines represent the PDF's of the random phase signal with the same energy as the original signal (see Chapter 4 for more details). The PDFs are normalized by the corresponding standard deviations of the random-phased signal.

As one can see from Figure 2.5, the random phase signal fluctuations have Gaussian distributions at all scales. However, the observed magnetic fluctuations show scale-dependent deviation from Gaussianity. Non-Gaussian tails are identified at MHD scales, and they become even more pronounced at ion and sub-ion scales. We quantify the extension of the tails by calculating kurtosis in each ranges, see horizontal dotted lines in Figure 2.6 and Table 1 in Vinogradov et al. (2023, within Appendix E). From Figure 2.6 and from the values of $K$, it is clear that non-Gaussianity increases across all scales from MHD to sub-ion scales, except for $K(B_R)$ at sub-ion scales, where a small decrease is observed. It is possible that this decrease comes from the fact that $B_R$ spectrum is the lowest in energy and may hit the instrumental noise level first (i.e., at lower frequencies than two other components), see Figure 2.7.

Let us now compare our approach with the classical one. Solid lines in Figure 2.6 show kurtosis calculated using increments of magnetic field components at different time scales

$$\Delta B_i^\tau(t) = B_i(t+\tau) - B_i(t), \quad i = R, T, N. \tag{2.38}$$

The x-axis is frequency, i.e., inversed time scales $f = 1/\tau$. The 3 panels correspond to 3 magnetic field components in $(R, T, N)$ reference frame.

In the inertial range the kurtosis of increments increases with frequency. This is consistent with the behavior of the distribution of increments previously observed at such scales, Figure 2.2(a). At ion scales, there is a change of behavior for the 3 magnetic field components: $K(B_R)$ show plateau starting from $f_{ci}$ and going up to sub-ion scales, $K(B_T)$ has a maximum around $f_{ci}$ and a decrease at higher frequencies, and $K(B_N)$ is similar to $K(B_R)$. We note a change of behavior at the highest frequencies for all components. The saturation of kurtosis at scales smaller than ion scales has been previously observed at 1 au and closer to the Sun (Chhiber et al., 2021). They interpreted it as the development of monofractal turbulence at the kinetic scales with a scale-independent fragmentation of current structures, as suggested by kinetic simulations (Karimabadi et al., 2013). We can interpret the saturation of increment-based-kurtosis in the following way: Since increments capture mostly planar structures (like current sheets), then their abscence at sub-ion scales (see below, sub-section 4.3.3) could imply a kurtosis that saturates at these scales.

A third approach is to use Morlet wavelet coefficients as proxies of turbulent fluctuations. Precisely, in this approach, we progressively remove more and more low frequencies

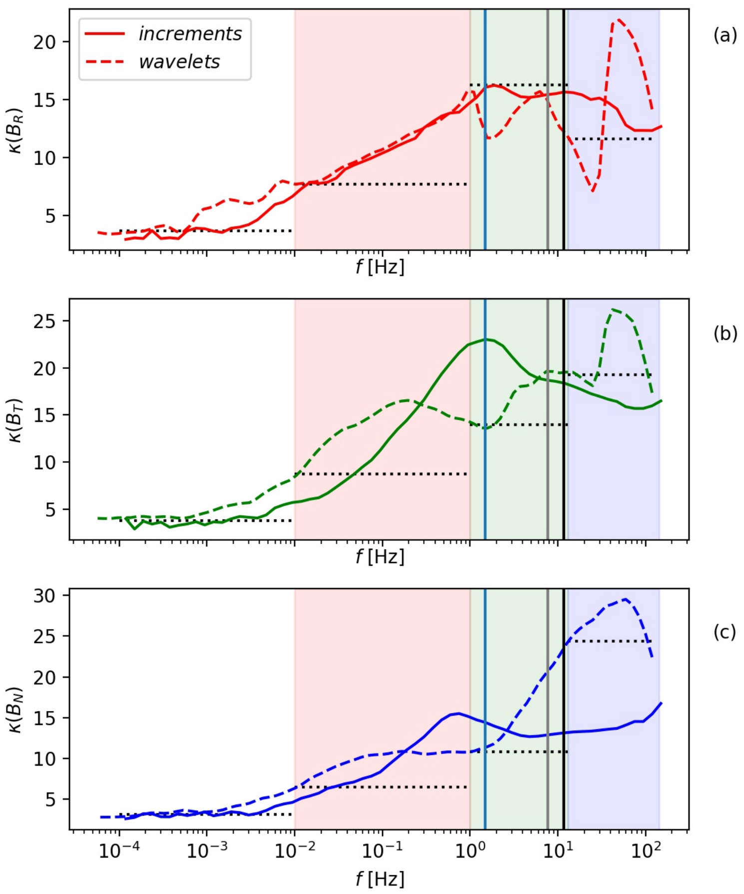

Figure 2.6: Kurtosis of magnetic field components $(B_R, B_T, B_N)$ are shown in panels (a,b,c), respectively. Kurtosis of increments is shown by solid lines. Kurtosis of the high-pass filtered signal, based on the Morlet wavelet coefficients according to the Equation (2.40), is shown by dashed lines. The vertical lines show the characteristic ion scales: ion cyclotron frequency $f_{ci}$ (in blue), and the frequencies computed with the Doppler shifted ion gyroradius $f_{\rho i}$ (in black) and the Doppler shifted ion inertial length $f_{di}$ (in gray). Horizontal black dotted lines show the values of kurtosis of the filtered fluctuations, shown in Figure 2.5.

of the magnetic field fluctuations to define the signal $B_\tau^{\leq}$. This is done by using Morlet wavelet inverse transform at scales $\tau_n$ smaller than $\tau$, see Equation (11) in Torrence and Compo (1998), or (12) in Perrone et al. (2016).

$$B_i^{<\tau} = \frac{\delta n \delta t^{1/2}}{C_\delta \psi_0(0)} \sum_{\tau_n < \tau} \frac{\Re(W[B_i](t, \tau_n))}{\tau_n^{1/2}}. \tag{2.39}$$

where $n$ is the scale index, $\delta n = 0.25$ is the parameter controlling the step in timescales, the $C_\delta = 0.776$ and $\psi_0(0) = \pi^{1/4}$ are Morlet transform constants Torrence and Compo (1998).

Then, we follow the definition of kurtosis by Frisch (1995, page 122, Equation (8.2)):

$$K^{<}(\tau) = \frac{\langle (B_\tau^{\leq})^4 \rangle}{\langle (B_\tau^{\leq})^2 \rangle^2}. \tag{2.40}$$

We show the results in Figure 2.6 by dashed lines. One can see that in the inertial range, $K^{<}$ based on wavelets (dashed lines) follows $K$ of increments (solid lines): an increase with frequency is present, as expected. At sub-ion range, $K^{<}$ globally increases. $K^{<}(B_R)$ has significant fluctuations, $K^{<}(B_T)$ increases with smaller fluctuations and $K^{<}(B_N)$ increases smoothly up to $\sim 50$ Hz. At the highest frequencies, the data are affected by instrumental filtering so we do not trust the $K^{<}$ values for the frequencies $f > 50$ Hz. The difference in $K^{<}(B_R)$ at sub-ion scales may come from the fact that the power spectral density of $B_R$ is the lowest in energy at high frequencies, as was already discussed above, see Figure 2.7 (red line).

Clearly, different ways to define turbulent eddies give different results for kurtosis $K(f)$. We have considered: (1) probability distribution functions and their kurtosis for fluctuations covering ranges of scales, then we have considered (2) increments and (3) Morlet wavelet based high-passed filtered signal. These three approaches have comparable results in the inertial range with an increase of $K$ with $f$ for the 3 components of magnetic field. At higher frequencies the results of (1) are in agreement with (3), where we do not see saturation of intermittency at ion scales as present with (2), but rather an increase of the signatures of coherent structures. We will verify this result in the physical space in Chapter 4. Now, let us discuss, in the next chapter, the theoretical models of possible coherent structures we can meet in the solar wind.

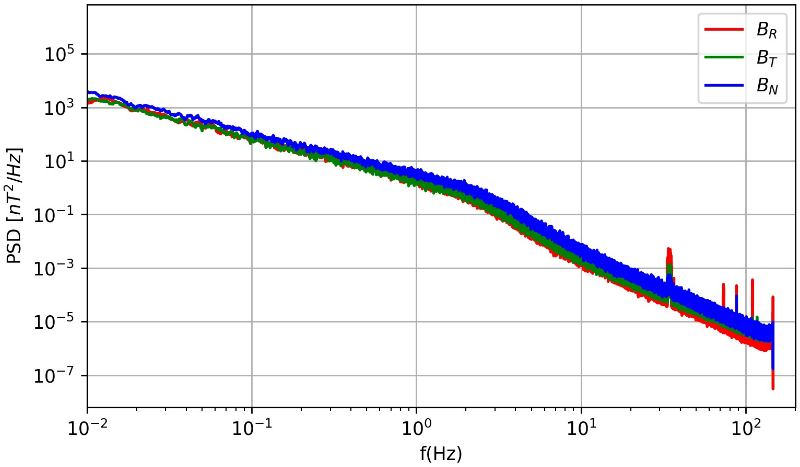

Figure 2.7: Power spectral density of magnetic field components ($B_R$,$B_T$,$B_N$) for the analysed time interval of 5h during the E1 of PSP. At high frequencies (corresponding to sub-ion scales) the power spectral density of $B_R$ (red line) is less energetic than for the other two components.

# Chapter 3

# Models of coherent structures

Previously, turbulence was seen as the chaotic, unpredictable in detail motion of a fluid, so that only statistical properties of fluctuations are reproducible. It was the common view until the discovery of the emergence of quasi-deterministic coherent structures in turbulent flows. Coherent structure can be defined as stable localized in space event with a high-amplitude and phase coherence over its spatial extent (Hussain, 1986; Fiedler, 1988; Veltri, 1999; Bruno et al., 2001; Mangeney, 2001; Farge and Schneider, 2015; Alexandrova, 2020).

In hydrodynamic experiments, coherent structures typically represent vorticity filaments (van Dyke, 1982; Jiménez et al., 1993; Vincent and Meneguzzi, 1991). They can be detected in flow visualization experiments (for example Fiedler, 1988; Zhou et al., 1999; Green et al., 2007). Recently the deep learning methods were applied to predict the number and filling factor of the coherent structures over time in a turbulent channel flow (Schmekel et al., 2022).

In this Chapter we discuss different types of coherent structures observed in the solar wind (properties, occurrence rate, possible generation mechanisms). In Sections 3.1 and 3.2 we briefly describe the coherent structures that are typically studied in the solar wind. In Section 3.3 we concentrate on the model of Alfvén vortices. We provide the derivation of the Alfvén vortex model which were less investigated so far than other coherent structures, so we provide a deeper discussion. We generalize the derivation to describe the case of multipole vortices.

## 3.1 Current sheets

Current sheets are locally planar coherent structures that separate the plasma with different magnetic field directions. Already the first satellite measurements of the magnetic field in the solar wind revealed the presence of current sheets (Burlaga et al., 1977). Figure 3.1 shows an example of the Explorer 43 satellite measuring the magnetic field in a fast solar wind stream at 1 au. The magnetic field component $B_y$ changes sign in the center of the

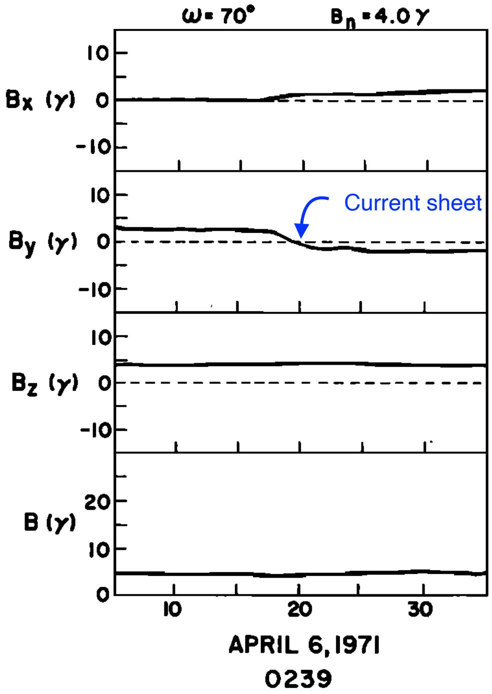

Figure 3.1: An example of a current sheet crossed by Explorer 43 spacecraft. The panels show the three components and the magnitude of the measured magnetic field in function of time (adapted from Burlaga et al., 1977).

interval. This is an example of a current sheet observed in the solar wind.

Current sheets with large rotation angles across the sheet represent the boundaries of magnetic tubes (Bruno et al., 2001; Borovsky, 2008). The population of current sheets with smaller rotation angles is much more numerous than the one with large angles (Borovsky, 2008). These current sheets might be formed spontaneously as a result of the turbulent cascade (e.g. Matthaeus and Montgomery, 1980; Veltri, 1999; Mangeney, 2001; Servidio et al., 2008; Salem et al., 2009; Zhdankin et al., 2012; Greco et al., 2008, 2009, 2012).

MHD classification of current sheets include rotational (RDs) and tangential (TDs) discontinuities (e.g. Baumjohann and Treumann, 1997; Tsurutani et al., 2011). A typical method to distinguish RD from TD is based on the normalised change in magnetic field magnitude $\Delta B/B$ across the discontinuity (which is zero for RD) and the normal magnetic field component normalised to the magnetic field magnitude $B_n/B$ (which is zero for TD). The sketch illustrating both types of discontinuities is shown in Figure 3.2. However,

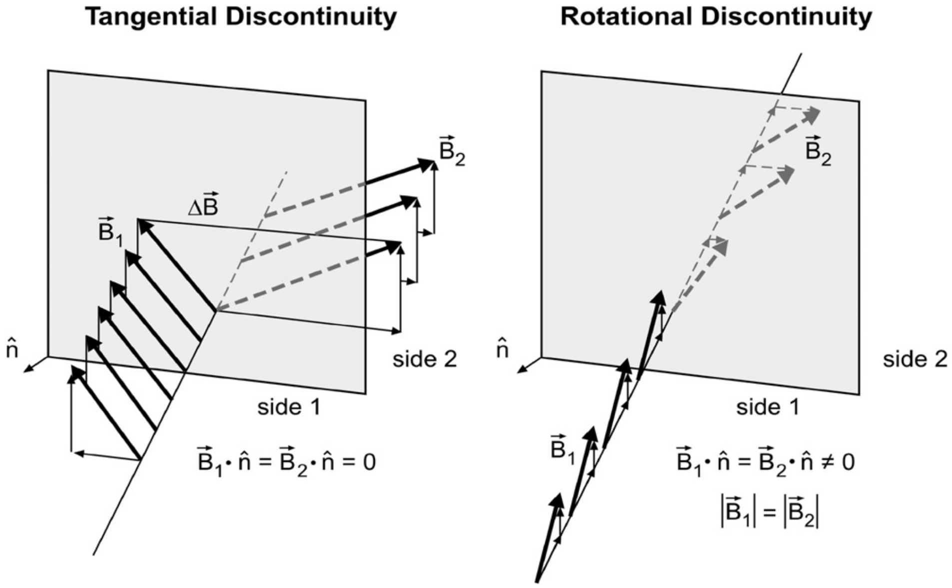

Figure 3.2: A schematics of tangential and rotational discontinuities showing the variation of the magnetic field across the structures. Adapted from Tsurutani et al. (2011).

observations showed that current sheets can combine both properties of RDs and TDs (Neugebauer, 2006; Artemyev et al., 2019).

Typically, the thickness of the current sheets is of the order of ion kinetic scales. But there are also thin current sheets with spatial sizes ranging from proton Larmor radius $\rho_p$ down to electron Larmor radius $\rho_e$ (Perri et al., 2012; Greco et al., 2016).

Ion kinetic scale current sheets become potential sites of magnetic reconnection (Cassak et al., 2006; Donato et al., 2012). Reconnection leads to the conversion of magnetic energy into kinetic and thermal energy. Observations show that high magnetic field increments, associated with current sheets, correlate with regions of increased local heating (Osman et al., 2011; Wu et al., 2013; Chasapis et al., 2015; Sioulas et al., 2022). This might indicate that the reconnection is one of the mechanisms of the turbulent magnetic energy dissipation.

The first *in-situ* observational evidence of magnetic reconnection in the solar wind (in the interior of an interplanetary coronal mass ejection) was found by Gosling et al. (2005), who observed the bifurcation of the current sheet related with the reconnection jet. When the spacecraft is crossing a bifurcated current sheet, the magnetic field is changing twice: first, when the spacecraft enters the reconnection outflow region and the second when it leaves it. Reconnection events have been frequently observed in the regular solar wind (Phan et al., 2006; Davis et al., 2006; Gosling, 2007; Enžl et al., 2014, 2017; Mistry et al., 2015, 2017). Automatic detection of reconnection events allowed to analyze large statistics of events (Tilquin et al., 2020; Eriksson et al., 2022; Fargette et al., 2023).

The occurrence rate of current sheets is ranging from a few hundred per day at 1 au (Vasquez et al., 2007a; Podesta, 2017; Vasko et al., 2022) to $\simeq 10^3$ day$^{-1}$ at 0.17 au (Lotekar et al., 2022). This is a plausible indication that current sheets are mostly formed close to the Sun and then are dissipated as the distance to the Sun increases. Restricting only to reconnecting current sheets, the occurrence rate was found from minimum of 0.4 day$^{-1}$ (WIND data at 1 au, Phan et al., 2010) up to 7 day$^{-1}$ (Solar Orbiter data at 0.7 au, Fargette et al., 2023).

Interestingly, during the first PSP encounter, most of the reconnection events (21 in total) were detected far from the perihelion (Phan et al., 2020). They speculate that the reconnection might be less frequent due to the specific highly-Alfvénic solar wind observed for this encounter, where the finite normal magnetic field prevents reconnection, and the dominance of rotational discontinuities.

## 3.2 Magnetic holes

A magnetic hole is a coherent structure that represents a strong localised magnetic field modulus decrease. Magnetic holes are observed in the solar wind, e.g. (Turner et al., 1977; Winterhalter et al., 1994; Stevens and Kasper, 2007; Volwerk et al., 2020; Wang et al., 2020).

Figure 3.3 shows a typical example of magnetic hole detected by the WIND spacecraft (Stevens and Kasper, 2007). The magnetic field magnitude dip is shown in the top panel. The proton density and temperature are enhanced inside the magnetic hole (see 3rd and 4th panels of Figure 3.3). The decrease of magnetic pressure is balanced by the increase of proton kinetic pressure. The temperature anisotropy $T_{p,\perp}/T_{p,\parallel}$ (bottom panel) is higher inside the magnetic hole than in the surrounding plasma. The crossection width of this magnetic hole is about 100 $\rho_p$, where $\rho_p$ is the proton Larmor radius.

Statistically, the crossing widths of MHD-scale magnetic holes cover a broad range of scales: from $\sim 10\,\rho_p$ to $\sim 10^3\rho_p$ (Stevens and Kasper, 2007; Karlsson et al., 2021). The occurrence rate of magnetic holes is higher closer to the Sun: from 2.4 per day at 0.7 au to 3.4 per day at 0.3 au (Volwerk et al., 2020).

The origin of magnetic holes is still under debate. The plausible mechanism of the large (MHD-scale) magnetic holes formation is the mirror mode instability. Under the condition:

$$1 + \beta_{p,\parallel}\left(1 - \frac{T_{p,\perp}}{T_{p,\parallel}}\right) < 0, \quad \text{where } \beta_{p,\parallel} = \frac{n_p k_B T_{p,\parallel}}{B^2/2\mu_0} \tag{3.1}$$

an enhanced plasma density develops in the magnetic field depression regions (Chandrasekhar et al., 1958; Vedenov and Sagdeev, 1961; Hasegawa, 1969; Southwood and Kivelson, 1993). Magnetic holes were mainly detected in the anisotropic, high-$\beta$ solar wind, in

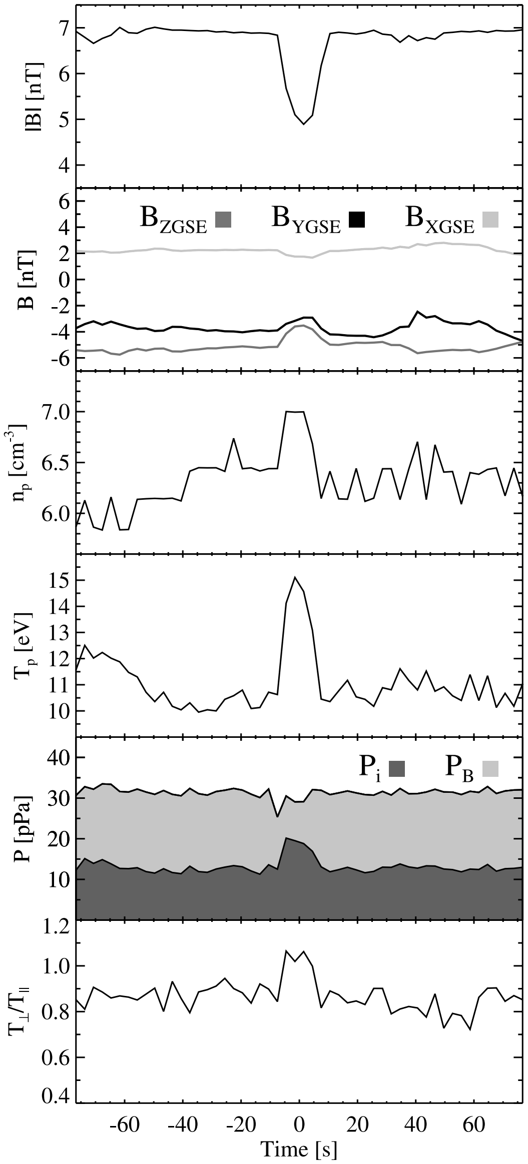

Figure 3.3: A magnetic hole detected by WIND satellite. From top to bottom the panels show the magnetic field strength and its components, the proton density and temperature, the plasma and magnetic pressures, and the ratio of orthogonal to parallel temperatures with respect to the local mean magnetic field orientation (adapted from Stevens and Kasper, 2007).

proximity of the instability threshold of Equation (3.1) (Tsurutani et al., 1992; Winterhalter et al., 1994; Stevens and Kasper, 2007). This observation supports the association of magnetic holes with mirror modes, however many magnetic holes are also found in the mirror mode stable environment.

Other mechanisms for the formation of magnetic holes have been proposed, such as non-linear evolution of Alfvén waves (Tsurutani et al., 2002; Dasgupta et al., 2003); local inhomogeneities introduced by large-amplitude Alfvén wave packets that evolve into magnetic holes (Buti et al., 2001) or soliton solutions in magnetized fluid models (Baumgärtel, 1999).

Sub-ion scale magnetic holes have been found in the solar wind (Wang et al., 2020). Sub-ion scale magnetic holes display properties that are inconsistent with their formation by the mirror instability (Sundberg et al., 2015). In particular, their size is much smaller than the typical wavelengths associated with mirror modes. Moreover, they are typically observed in an environment which is stable to the mirror instability (Balikhin et al., 2012). Furthermore, these sub-ion scale structures are typically associated with an enhanced electron temperature anisotropy, while the ions do not show any response to the presence of such small-scale magnetic holes. This is in contrast with the properties of large-scale magnetic holes, where the magnetic field depression is balanced by an increase in ion density and pressure.

## 3.3 Alfvén vortices

### 3.3.1 Summary of previous works

Alfvén vortices are typically described as cylindrically symmetric coherent structures nearly aligned with the background magnetic field. The first multi-satellite observation of Alfvén vortices have been done in the Earth's magnetosheath with the Cluster mission (Alexandrova et al., 2004, 2006; Alexandrova, 2008). Cassini measurements indicate the presence of such structures in the Kronian magnetosheath as well (Alexandrova and Saur, 2008). Signatures of Alfvén vortices were found in single spacecraft data (Verkhoglyadova et al., 2003; Lion et al., 2016). Later the existence of Alfvén vortices in the solar wind was confirmed with the 4 spacecrafts of Cluster (Roberts et al., 2016; Perrone et al., 2016, 2017). Wang et al. (2019) investigated the kinetic effects within an Alfvén vortex thanks to MMS measurements in the Earth's magnetosheath.

A recent simulation paper indicates that Alfvén vortices might emerge at the late stage of the solar wind turbulence (Meyrand et al., 2023). Closer to the Sun the outward Alfvén waves dominate. The solar wind expantion effects are taken into account in the simulation. The reflection of Alfvénic fluctuations from background gradients, enable nonlinear interactions between counter-propagating wave packets. This process is called the reflection-driven turbulent cascade (Velli et al., 1989; Chandran and Perez, 2019). At the larger distances the fluctuations gradually become balanced $z^+ \sim z^-$, structured into an ensemble of nonlinear Alfvén vortices.

The Alfvén vortex theoretical solution for monopoles and dipoles has been described for the first time by Petviashvili and Pokhotelov (1992), however the discussion of the assumptions is not complete. Another derivation of Alfvén vortices with different assumptions is given in Verkhoglyadova et al. (2003). In the following section we provide a detailed derivation of the Alfvén vortex model with the complete description of the underlying assumptions.

### 3.3.2 Reduced magnetohydrodynamics (RMHD) equations

**Hypothesis**

Magnetic fluctuations in the solar wind are anisotropic with a much larger energy power in the fluctuations transverse to the mean local magnetic field compared to the parallel one so $B_\perp \gg B_\|$ (see Section 2.3). Accordingly, it is reasonable to use the reduced magnetohydrodynamics equations (RMHD, Kadomtsev and Pogutse, 1974; Strauss, 1976). Assuming that the solution is transverse-dominant, slow-evolving, and for small-amplitudes, we have the ordering:

$$\partial_z/\nabla_\perp \sim \partial_t/V_A\nabla_\perp \sim B_\perp/B_0 \sim V_\perp/V_A \ll 1 \tag{3.2}$$

**General implications**

The mass conservation equation reduces to $\nabla \cdot \mathbf{V} = 0$, so the plasma is incompressible. MHD momentum and induction equations can be simplified to a pair of scalar equations describing RMHD (Kadomtsev and Pogutse, 1974; Strauss, 1976). The independent variables of RMHD equations are flux function $\psi$ and axial vector potential $A_z$. The flux function $\psi$ is defined in the following way:

$$\mathbf{V}_\perp = (\mathbf{e}_z \times \nabla\psi) = (-\frac{\partial\psi}{\partial y}, \frac{\partial\psi}{\partial x}, 0) \tag{3.3}$$

The vorticity is $\mathbf{\Omega} = \nabla \times \mathbf{V}$. RMHD involves only the axial vorticity $\omega$ (vorticity along the local mean magnetic field):

$$\omega = \mathbf{\Omega}_z = \nabla_\perp^2\psi \tag{3.4}$$

The axial vector potential $A_z$ ($\mathbf{B} = \nabla \times \mathbf{A}$) is defined as:

$$\mathbf{B}_\perp = \nabla A_z \times \mathbf{e}_z \tag{3.5}$$

The axial current density $J$ ($\mathbf{J} = \frac{1}{\mu_0}\nabla \times \mathbf{B}$) writes:

$$J = \mathbf{J}_z = \nabla_\perp^2 A_z \tag{3.6}$$

**Conversion to dimensionless equations**

As was done in Petviashvili and Pokhotelov (1992), we introduce the following normalized

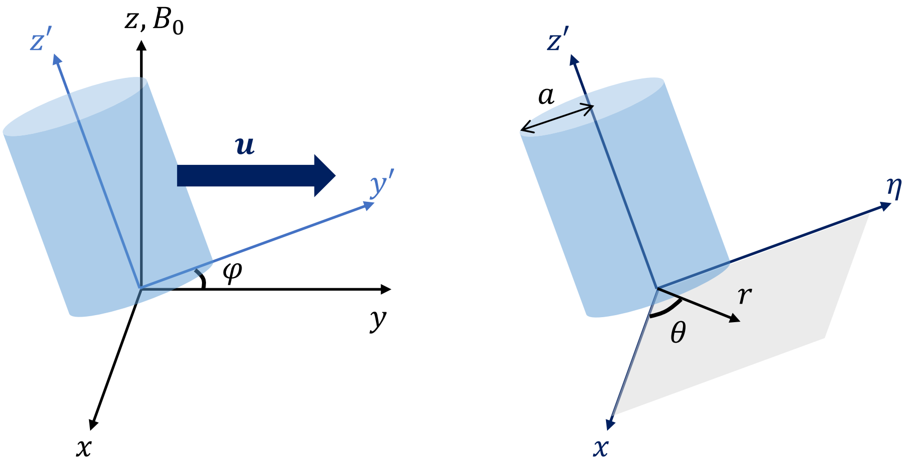

Figure 3.4: The left panel shows the propagation of the vortex at the speed $\mathbf{u}$. The vortex axis is inclined with respect to the local mean magnetic field $\mathbf{B}_0$ by the angle $\varphi$. $z$ is set in the direction of $\mathbf{B}_0$ and $y$ is set in the plane $(\mathbf{u}, \mathbf{B}_0)$. The right panel introduces the cylindrical coordinates $(r, \theta)$ associated with the moving vortex of radius $a$.

quantities:

$$\Omega_{ci}t, \quad \mathbf{r}_\perp/\rho_i, \quad \frac{z}{c/\omega_{pi}}, \quad \rho/\rho_0, \quad \frac{\psi}{\rho_i^2\Omega_{ci}}, \quad \frac{A_z V_A}{B_0\rho_i^2\Omega_{ci}} \tag{3.7}$$

where $\Omega_{ci} = eB_0/m_i$, $\rho_i = w_{\perp,i}/\Omega_{ci} = \sqrt{2k_BT_\perp/m_i}/\Omega_{ci}$, $\omega_{pi} = \sqrt{e^2n_i/\epsilon_0 m_i}$, $V_A = B_0/\sqrt{\mu_0\rho_0}$. This allows to write dimensionless equations. In order to simplified the notations, we still keep the same notation, $t$, $x$, $y$, $z$, $\psi$ and $A_z$ for all the following dimensionless equations.

**RMHD equations in dimentionless units**

Using the above assumptions, the momentum and induction MHD equations are simplified to a couple of dimentionless RMHD equations:

$$\partial_t\omega + \{\psi, \omega\} = -\{A_z, J\} + \partial_z J \tag{3.8}$$

$$\partial_t A_z + \{\psi, A_z\} = -\partial_z\psi \tag{3.9}$$

where the Poisson brackets are defined as:

$$\{f, g\} = \frac{\partial f}{\partial x}\frac{\partial g}{\partial y} - \frac{\partial f}{\partial y}\frac{\partial g}{\partial x}$$

### 3.3.3 RMHD equations for 2D coherent structures

**Introducting coherent structures**

Equations (3.8) and (3.9) are coupled equations for $A_z(x,y,z,t)$ and $\psi(x,y,z,t)$. Here, following Petviashvili and Pokhotelov (1992), we look for coherent structures which are propagating in the plasma at a constant velocity $u$ while keeping their shapes, so without an explicit function of time. For example a function such as $A_z(x, y - u\,t)$ is a two-dimensionnal solution which is propagating without deformation in the $y$ direction with the velocity $u$. This function is independent of $z$, so it is invariant along the direction of the background magnetic field $\mathbf{B}_0$. In order to be more general, we let the coherent structure to be inclined on the $z$ axis by an angle $\varphi$. In this case, the flux function $\psi$ and the vector potential $A_z$ are functions of the new coordinates $(x,\eta)$, where

$$\eta = y + \tan(\varphi)\, z - u\, t \tag{3.10}$$

The inclination angle $\varphi$ should be small in accordance with RMHD assumption $\partial_z/\nabla_\perp \ll 1$. We introduce the corresponding inclined coordinate system:

$$\begin{cases} x' = x \\ y' = \cos\varphi\, y + \sin\varphi\, z \\ z' = -\sin\varphi\, y + \cos\varphi\, z \end{cases} \tag{3.11}$$

The case of a cylindrical structure, defined in the $x, y'$ plane, and invariant in the $z'$ direction is represented in Figure 3.4. The propagation speed in the $y$ direction is at the constant speed $u$, while the propagation speed orthogonally to the structure, in $y'$ direction, is $u\cos\varphi$.

**RMHD equations for coherent structures**

With $A_z(x,\eta)$, the derivatives in Equation (3.8) transform as:

$$\begin{cases} \partial_t A_z = \frac{\partial A_z}{\partial \eta}\frac{\partial \eta}{\partial t} = -u\,\partial_\eta A_z \\ \partial_x A_z = \partial_x A_z \\ \partial_y A_z = \frac{\partial A_z}{\partial \eta}\frac{\partial \eta}{\partial y} = \partial_\eta A_z \\ \partial_z A_z = \frac{\partial A_z}{\partial \eta}\frac{\partial \eta}{\partial z} = \alpha\,\partial_\eta A_z \end{cases} \tag{3.12}$$

where $\alpha = \tan(\varphi)$. Similar expressions are obtained for $\psi(x,\eta)$.

Then, the induction Equation (3.9) is transformed successively to:

$$-u\,\partial_\eta A_z + \partial_\eta A_z\,\partial_x\psi - \partial_\eta\psi\,\partial_x A_z + \alpha\,\partial_\eta\psi = 0$$

$$\partial_\eta A_z(\partial_x\psi - u) - \partial_\eta\psi(\partial_x A_z - \alpha) = 0$$

$$\partial_x(\psi - ux)\partial_\eta(A_z - \alpha x) - \partial_x(A_z - \alpha x)\partial_\eta(\psi - ux) = 0$$

This introduces the new Poisson brackets:

$$\{\tilde{\psi}, \tilde{A}_z\}_{x,\eta} = \frac{\partial\tilde{\psi}}{\partial x}\frac{\partial\tilde{A}_z}{\partial\eta} - \frac{\partial\tilde{A}_z}{\partial x}\frac{\partial\tilde{\psi}}{\partial\eta} \tag{3.13}$$

where we introduce the modified magnetic vector potential and flux function:

$$\begin{cases} \tilde{A}_z = A_z - \alpha\, x \\ \tilde{\psi} = \psi - u\, x \end{cases} \tag{3.14}$$

Finally, the induction RMHD Equation (3.9) is written in the following compact form:

$$\{\tilde{\psi}, \tilde{A}_z\}_{x,\eta} = 0 \tag{3.15}$$

A similar procedure is next applied to the momentum RMHD equation, and we skip the derivation steps below. Substituting Equation (3.12), and equivalent forms with $\psi$, to the momentum RMHD Equation (3.8) and using Equations (3.13) and (3.14), it is rewritten as:

$$\{\tilde{\psi}, \tilde{\nabla}_\perp^2\tilde{\psi}\}_{x,\eta} = \{\tilde{A}_z, \tilde{\nabla}_\perp^2\tilde{A}_z\}_{x,\eta} \tag{3.16}$$

where we define the new Laplace operator:

$$\tilde{\nabla}_\perp^2 = \frac{\partial^2}{\partial x^2} + \frac{\partial^2}{\partial\eta^2} \tag{3.17}$$

**In summary**, Equations (3.15) and (3.16) are the compact form taken by the RMHD equations for two-dimentionnal coherent structures where the flux function $\psi$ and the vector potential $A_z$ are functions of $(x, \eta)$ with $\eta$ defined by Equation (3.10). This transformation set the two equations in a more compact format suitable to derive their properties and analytical solutions, thanks to the properties of Poisson brackets.

### 3.3.4 General solutions for 2D coherent structures

**Solutions for the flux function and vector potential**

Equation (3.15) means that $\tilde{\psi}$ and $\tilde{A}_z$ are dependent on each other. The general solution of the Equation (3.15) is:

$$\tilde{\psi} = g(\tilde{A}_z) \tag{3.18}$$

where $g(\tilde{A}_z)$ is an arbitrary function (Petviashvili and Pokhotelov, 1992). Next, we use the above expression in order to obtain the solution of Equation (3.16). The left side of the Equation (3.16) is rewritten as:

$$\begin{aligned} \{\tilde{\psi}, \tilde{\nabla}_\perp^2\tilde{\psi}\}_{x,\eta} &= \{g(\tilde{A}_z), \tilde{\nabla}_\perp^2 g(\tilde{A}_z)\}_{x,\eta} \\ &= \{g'\,\tilde{A}_z, \tilde{\nabla}_\perp^2 g(\tilde{A}_z)\}_{x,\eta} \\ &= \{\tilde{A}_z, g'\,\tilde{\nabla}_\perp^2 g(\tilde{A}_z)\}_{x,\eta} \end{aligned}$$

with $g' = dg/d\tilde{A}_z$. Then, Equation (3.16) is rewritten as:

$$\{\tilde{A}_z, \tilde{\nabla}_\perp^2 \tilde{A}_z - g' \, \tilde{\nabla}_\perp^2 g(\tilde{A}_z)\}_{x,\eta} = 0$$

which implies:

$$\tilde{\nabla}_\perp^2 \tilde{A}_z - g'(\tilde{A}_z) \, \tilde{\nabla}_\perp^2 g(\tilde{A}_z) = h(\tilde{A}_z) \tag{3.19}$$

where $h(\tilde{A}_z)$ is another arbitrary function of $\tilde{A}_z$. This provides a second order differential equation for $\tilde{A}_z$. Equation (3.19) is generally non linear due to the presence of the general functions $g(\tilde{A}_z)$ and $h(\tilde{A}_z)$. If a set of solutions for $\tilde{A}_z$ is found, then $\tilde{\psi}$ is obtained with Equation (3.18). With the definitions of Equation (3.14), this provides solutions to the RMHD Equations (3.8) and (3.9).

**Implications for the velocity and magnetic field**
The velocity is given by Equation (3.3) which can be written in function of $\tilde{A}_z$ as follows:

$$\begin{aligned}
\mathbf{V}_\perp &= \mathbf{e}_z \times \nabla\psi \\
&= \mathbf{e}_z \times \nabla(\tilde{\psi} + u\,x) \\
&= g' \mathbf{e}_z \times \nabla(\tilde{A}_z) + u\,\mathbf{e}_y \\
&= -g'(\mathbf{B}_\perp + \alpha\,\mathbf{e}_y) + u\,\mathbf{e}_y
\end{aligned}$$

where we use

$$\mathbf{B}_\perp = (\nabla A_z \times \mathbf{e}_z) = (\nabla \tilde{A}_z) \times \mathbf{e}_z) - \alpha\,\mathbf{e}_y$$

**In summary**, $\mathbf{V}_\perp$ and $\mathbf{B}_\perp$ are related as:

$$\mathbf{V}_\perp = -g' \mathbf{B}_\perp + (u - \alpha\, g')\,\mathbf{e}_y \tag{3.20}$$

This implies a finite $\mathbf{V}_\perp$ in all the $(x, \eta)$ plane except where $g' = u/\alpha$. Then, for a coherent structure with a finite spatial extension, the departure of $g'(\tilde{A}_z)$ from $u/\alpha$ should be limited to a finite region.

### 3.3.5 Linearized RMHD equations for 2D coherent structures

Equations (3.15) and (3.16) are the compact form of the RMHD equations for solutions of the form $A_z(x, \eta)$ and $\psi(x, \eta)$. Both are generally non linear equations as shown above. The implied link between $\mathbf{V}_\perp$ and $\mathbf{B}_\perp$, Equation (3.20), implies $g' = u/\alpha$ outside the coherent structure. Then, using Equation (3.18) this implies a linear relationship between $\tilde{\psi}$ and $\tilde{A}_z$ ($\tilde{\psi} = u/\alpha\,\tilde{A}_z$). Below, we extend this linear relation ship inside the structure. This is a linearisation of Equation (3.15). We first explore the implications of this linearisation below, before exploring the implications of linearising also Equation (3.16).

**Linearisation of the induction equation**

Among the infinite set of solutions (see Equation (3.18), we consider the linear one with $g' = \xi =$ constant:

$$\tilde{\psi} = \xi \tilde{A}_z \tag{3.21}$$

Then, Equation (3.20) is rewritten as:

$$\mathbf{V}_\perp = -\xi\, \mathbf{B}_\perp + (u - \xi\alpha)\, \mathbf{e}_y \tag{3.22}$$

Then, we need to set

$$\xi = u/\alpha \tag{3.23}$$

to eliminate the additional constant speed along $\mathbf{e}_y$ (second term on the right hand side). This constant speed is a global motion of the plasma, and it can be removed by a change of frame. This first linearisation means that

$$\mathbf{V}_\perp = -\xi\, \mathbf{B}_\perp \tag{3.24}$$

so they are proportional everywhere. By taking the curl of this equation, one finds the proportionality everywhere between the vorticity and the current density.

**Implication for the momentum equation**

Substituting Equation (3.21) into the Equation (3.16), we get:

$$(\xi^2 - 1)\{\tilde{A}_z, \tilde{\nabla}^2_\perp \tilde{A}_z\}_{x,\eta} = 0 \tag{3.25}$$

There are two independent set of solutions:

- If $\xi = \pm 1$ we obtain arbitrary Alfvénic solution with $d\mathbf{V}_\perp = \mp d\mathbf{B}_\perp$. In this case any nonlinearities of the RMHD momentum equation can be included. Indeed, with $\xi = \pm 1$, the convective term and Lorenz force term in the RMHD momentum Equation (3.8) are balanced.
- If $\xi \neq \pm 1$, the Poisson bracket must be equal zero which implies

  $$\tilde{\nabla}^2_\perp \tilde{A}_z = h(\tilde{A}_z) \tag{3.26}$$

  with $h(\tilde{A}_z)$ an arbitrary function. Physically it means that current density, $J = -\nabla^2_\perp A_z = -\tilde{\nabla}^2_\perp \tilde{A}_z$, is an arbitrary function of the modified vector potential: $J = J(\tilde{A}_z)$.

**Linearisation of the momentum equation**

Below we further explore the case $\xi \neq \pm 1$ by linearising $h(\tilde{A}_z)$. We also look for solutions for vortices having a cylinder shape. Then, we introduce the cylindrical coordinate system associated with the vortex:

$$\begin{cases} r = \sqrt{x^2 + \eta^2} \\ \theta = \arctan(\eta/x) \end{cases} \tag{3.27}$$

The moving boundary of the vortex is defined in the following way:

$$r = \sqrt{x^2 + \eta^2} = \sqrt{x^2 + (y + \alpha z - ut)^2} = a, \quad \text{where } a \text{ is the vortex radius} \tag{3.28}$$

We seek the solution with the current density localized in the cylinder so $h(\tilde{A}_z) = 0$ for $r > a$. Equation (3.26) is similar to the force free equation $\nabla_\perp^2 A_z = h(A_z)$ obtained by imposing $\mathbf{j}$ parallel to $\mathbf{B}$ (no Lorentz force). For a linear force free field $\mathbf{j} = k\,\mathbf{B}$ with $k$ a constant. This implies $\mathbf{B} = k\,\mathbf{A}$ (selecting a specific gauge, $\nabla \cdot \mathbf{A} = 0$ as allowed). Then $\mathbf{j} = k^2\,\mathbf{A}$, so that the linear force free equation writes $\nabla_\perp^2 A_z = -k^2 A_z$. Since $\alpha$ is supposed to be small (to be in the RMHD conditions), $\tilde{A}_z \approx A_z$, then we use the same equation for $\tilde{A}_z$ in the region $r < a$. The linear version of Equation (3.26) is an Helmholtz equation inside the cylinder and a Laplace equation outside the cylinder, as follows:

$$\begin{cases} \nabla_\perp^2 \tilde{A}_z = -k^2 \tilde{A}_z & r \le a \\ \nabla_\perp^2 \tilde{A}_z = 0 & r > a \end{cases} \tag{3.29}$$

where $k$ is an arbitrary constant, and we suppose that there is no perturbation of the current density outside the vortex.

**General solution of the linearized equations**

The general solution of the Equation (3.29) is

$$\begin{cases} \tilde{A}_z = \sum_{n=0}^{\infty} (a_n J_n(kr) + b_n Y_n(kr)) \cos(n\theta + \theta_n) & r \le a \\ \tilde{A}_z = -c_0 \ln(r) + d_0 + \sum_{n=1}^{\infty} (c_n r^{-n} + d_n r^n) \cos(n\theta + \theta_n) & r > a \end{cases} \tag{3.30}$$

In terms of $A_z = \tilde{A}_z + \alpha x$, the above equation rewrites

$$\begin{cases} A_z = \sum_{n=0}^{\infty} (a_n J_n(kr) + b_n Y_n(kr)) \cos(n\theta + \theta_n) + \alpha r \cos(\theta) & r \le a \\ A_z = -c_0 \ln(r) + d_0 + \sum_{n=1}^{\infty} (c_n r^{-n} + d_n r^n) \cos(n\theta + \theta_n) + \alpha r \cos(\theta) & r > a \end{cases} \tag{3.31}$$

The radial and azimuthal components of the magnetic field are deduced from

$$\begin{cases} \mathbf{B}_r = \frac{1}{r} \frac{\partial A_z}{\partial \theta} \\ \mathbf{B}_\theta = -\frac{\partial A_z}{\partial r} \end{cases} \tag{3.32}$$

**Physical constraints for $r = 0$ and $r \to \infty$**

Bessel functions of the second kind $Y_n$ are singular at $r = 0$, it is non-physical, so $b_n = 0$.

Next, in case of localised vortex solution:

$$\begin{cases} B_\theta \underset{r\to\infty}{\rightarrow} 0 \\ B_r \underset{r\to\infty}{\rightarrow} 0 \end{cases} \tag{3.33}$$

So, the boundary conditions at $r \to \infty$ are:

$$\begin{cases} \partial_r A_z \underset{r\to\infty}{\rightarrow} 0 \\ \frac{1}{r}\frac{\partial A_z}{\partial \theta} \underset{r\to\infty}{\rightarrow} 0 \end{cases} \tag{3.34}$$

In order to satisfy these boundary conditions at $r \to \infty$, we need to set $d_1 = -\alpha$, $d_{n>1} = 0$ in solution (3.31).

**Physical solutions**

With non singular magnetic field at $r = 0$ and a vanishing perturbation at infinite distance ($r \to \infty$) the general solution of Equation (3.31) is reduced to:

$$\begin{cases} A_z = \sum_{n=0}^{\infty} a_n J_n(kr)\cos(n\theta + \theta_n) + \alpha r\cos(\theta) & r \le a \\ A_z = -c_0 \ln(r) + d_0 + \sum_{n=1}^{\infty} c_n r^{-n} \cos(n\theta + \tilde{\theta}_n) & r > a \end{cases} \tag{3.35}$$

The constant $c_0$ is related to the current $J_{tot}$ integrated over the circle $S$ of the radius $R > a$:

$$J_{tot} = \iint_S J \cdot ds = \oint_L B_\theta dl = -\int_0^{2\pi} \partial_r A_z|_{r=R} \cdot R d\theta = 2\pi c_0 \tag{3.36}$$

If we impose the condition that the total current of the vortex $J_{tot} = 2\pi c_0 = 0$, then $c_0 = 0$. Otherwise with a finite total current the magnetic field in the exterior decreases as $\sim 1/r$, so the perturbation is slowly decreasing with distance.

**Boundary conditions at the vortex border**

Now, we set the boundary conditions at $r = a$ to determine $a_n, c_n, \theta_n, \tilde{\theta}_n$. Divergence-free condition at the boundary $r = a$, requires the continuity of $B_r$. If there is no current layer at the boundary of the vortex, $B_\theta$ is also continuous at $r = a$. Both conditions with respect to $A_z$ give:

$$\begin{cases} [\partial_\theta A_z]\,|_{r=a} = 0 \\ [\partial_r A_z]\,|_{r=a} = 0 \end{cases} \tag{3.37}$$

The inner solution implies:

$$\begin{cases} \partial_\theta A_z|_{r=a-0} = -\sum_{n=0}^{\infty} a_n n J_n(ka)\sin(n\theta + \theta_n) - \alpha\, a \sin(\theta) \\ \partial_r A_z|_{r=a-0} = \sum_{n=0}^{\infty} a_n k J_n'(ka)\cos(n\theta + \theta_n) + \alpha \cos(\theta) \end{cases} \tag{3.38}$$

The outer solution implies:

$$\begin{cases} \partial_\theta A_z|_{r=a+0} = -\sum_{n=1}^{\infty} c_n a^{-n}\, n \sin(n\theta + \tilde{\theta}_n) \\ \partial_r A_z|_{r=a+0} = -\sum_{n=1}^{\infty} c_n a^{-n-1}\, n \cos(n\theta + \tilde{\theta}_n) \end{cases} \tag{3.39}$$

The application of the continuity of derivatives at $r = a$, Equation (3.37), must be satisfied for any $\theta$ value, then these conditions apply separately for different $n$ values (associated to different $\theta$ harmonics). A specific derivation is required for the $n = 0$, $n = 1$ and $n \geq 2$ as follows. For $n = 0$ (monopole) there is no radial magnetic field component (so no continuity condition at $r = a$). However the constraint of a vanishing total electric current is specific to this case. The case $n = 1$ (dipole) is particular because it incorporates the term $\alpha\, r \cos\theta = \alpha\, x$ coming from solving the RMHD equations for a moving vortex. It implies a specific behavior of the parallel dipole (with $A_z \propto \cos\theta$, then a dipole moment almost aligned with $\mathbf{B}_0$). In contrast the transverse dipole (with $A_z \propto \sin\theta$, then a dipole moment almost orthogonal with $\mathbf{B}_0$) behaves as the higher $n$ modes. Finally, all the $n \geq 2$ modes behave in the same way so they are described below before the $n = 1$ case as the transverse dipole has the same behavior.

### 3.3.6 Alfvén vortex modes

**Case n=0 (monopole)**

If $J_{tot} \neq 0$, there is a related nonzero coefficient $c_0 = J_{tot}/2\pi$, see Equation (3.36). The continuity conditions for $B_r$ and $B_\theta$ at the boundary of the cylinder, Equation (3.37), writes:

$$\begin{cases} 0 = 0 \\ a_0 k J_0'(ka) = -c_0/a \end{cases} \tag{3.40}$$

In this case, for a given vortex radius $a$, there is a constraint on $k$ which depends on the amplitude of the monopole vortex, controlled by $a_0$, and the total current, defined by the parameter $c_0$.

If we impose $J_{tot} = 0$, the continuity condition of Equation (3.37) writes:

$$\begin{cases} 0 = 0 \\ a_0 k J_0'(ka) = 0 \end{cases} \tag{3.41}$$

Since $J_0'(ka) = J_1(ka)$, the condition of no global currentfor the monopole implies the condition :

$$J_1(ka) = 0 \tag{3.42}$$

For a given vortex radius $a$, this implies that possible $k\,a$ values are limited to the series of $J_1$ zeros.

**Case n $\geq$ 2 (multipole)**
Applying the continuity condition of Equation (3.37) to each $n$ mode separately implies:

$$\begin{cases} -a_n\, n\, J_n(ka)\sin(n\theta+\theta_n) = -c_n\, n\, a^{-n}\sin(n\theta+\tilde{\theta}_n) \\ a_n k J_n'(ka)\cos(n\theta+\theta_n) = -c_n\, n\, a^{-n-1}\cos(n\theta+\tilde{\theta}_n) \end{cases}$$

Since this should be valid for any $\theta$ value, the external solution should have the same angular dependance than the internal one. This implies $\tilde{\theta}_n = \theta_n$ and the equations are simplified to:

$$\begin{cases} -a_n\, n\, J_n(ka) = -c_n\, n\, a^{-n} \\ a_n k\, a\, J_n'(ka) = -c_n\, n\, a^{-n} \end{cases} \tag{3.43}$$

We next use the expression for the derivative of the Bessel function and the recurrence relation:

$$J_n'(ka) = (J_{n-1}(ka) - J_{n+1}(ka))/2$$
$$J_{n+1}(ka) = \frac{2n}{ka} J_n(ka) - J_{n-1}(ka)$$

to write $kaJ_n'(ka) = kaJ_{n-1}(ka) - n\, J_n(ka)$. Then, Equations (3.43) are rewritten as the couple of equations:

$$\begin{cases} a_n\, n\, J_n(ka) = c_n\, n\, a^{-n} \\ a_n\, (n\, J_n(ka) - ka\, J_{n-1}(ka)) = c_n\, n\, a^{-n} \end{cases} \tag{3.44}$$

Both equations can only be satisfied if

$$J_{n-1}(ka) = 0 \tag{3.45}$$

For a given vortex radius $a$, this implies that possible $k\, a$ values are limited to the series of $J_{n-1}$ zeros. Since these zeros are different for different $n$ values, two modes cannot be superposed. However, each $n$ mode has an arbitrary amplitude $a_n$.

**Case n=1 (dipole)**
The dipole case is specific because of the extra term $\alpha r\cos\theta$ present in $A_z$ in Equation (3.35). The terms in $\cos(\theta+\theta_1)$ and $\cos(\theta+\tilde{\theta}_1)$ can always be split in a sum of a $\cos(\theta)$ and a $\sin(\theta)$ terms. The same applies for the $\sin(\theta+\theta_1)$ and $\sin(\theta+\tilde{\theta}_1)$ terms. The boundary conditions at $r = a$ apply separately to each of these terms (different $\theta$ behavior). Only the parallel dipole, with $A_z \propto \cos\theta$, is to be grouped with the $\alpha\, r\cos\theta$ term. It implies that the transverse dipole (with $A_z \propto \sin\theta$) behaves as the higher $n$ modes. In particular we can apply exactly the same derivation as above, just setting $n = 1$ in the above equations which implies that Equation (3.45) is also true for the transverse dipole.

For the parallel dipole, the term $\alpha\, r \cos\theta$ present in $A_z$ implies other contributions, then Equation (3.44) taken for $n = 1$ (valid for the transverse dipole) is completed for the parallel dipole with extra terms proportional to $\alpha$ as follows:

$$\begin{aligned} a_1\, J_1(ka) + \alpha a &= c_1\, a^{-1} \\ a_1\, \left(J_1(ka) - ka\, J_0(ka)\right) - \alpha a &= c_1\, a^{-1} \end{aligned} \tag{3.46}$$

The subtraction of these equations implies the amplitude of the internal solution:

$$a_1 = -2\alpha/(k\, J_0(ka)) \tag{3.47}$$

The amplitude of the solution for $r > a$ is

$$c_1 = \alpha a^2 \left(1 - \frac{2}{k\, a} \frac{J_1(ka)}{J_0(ka)}\right) \tag{3.48}$$

Then, the parallel dipole has a finite amplitude depending on $\alpha = \tan\varphi$ so on the inclination of the vortex axis on the mean field $\mathbf{B}_0$. In contrast with all other modes, there is no constraint on $k$ value (apart that $J_0(ka) \neq 0$). This contrast with the transverse dipole which has the constraint $J_0(ka) = 0$ (Equation (3.45)). Then the transverse dipole is incompatible with the presence of the parallel dipole as it would imply an infinite $a_1$ value. This incompatibility can also be seen directly in Equation (3.46) which needs a finite determinant of the associated matrix of coefficients to have a solution for the parallel dipole, while the same equation applies, without the terms in $\alpha$, for the transverse dipole. In this last case, the equations are compatible only if the determinant vanishes.

### 3.3.7 Summary and conclusion for Alfvén vortices

#### Setting the equations

We have searched for theoretical models of coherent structures in the framework of RMHD. We suppose that a coherent structure could move globally at a velocity $u$ in the plasma and that it is inclined by an angle $\varphi$ on the mean magnetic field $\mathbf{B}_0$ (Figure 3.4). With these hypotheses the RMHD equations could be rewritten in a compact form with Poisson brackets (Equations (3.15) and (3.16)) and the modified magnetic vector potential and flux function (defined by Equation (3.14)). This allows to derive the general non linear equation involving only the modified magnetic vector potential, Equation (3.19), and the relationship between the transverse velocity $\mathbf{V}_\perp$ and the transverse magnetic field $\mathbf{B}_\perp$, Equation (3.20). The linearisation of this equation implies $\mathbf{V}_\perp = -\xi \mathbf{B}_\perp$ with $\xi$ a constant defined by $u/\tan\varphi$. The momentum equation is then rewritten in a compact form, Equation (3.25), which have two set of solutions. The first set is Alfvénic, with $\mathbf{V}_\perp = \mp \mathbf{B}_\perp$ and with arbitrary spatial dependance. The second set has $\xi \neq \pm 1$ and a non linear equation, similar to the non linear force-free equation, needs to be satisfied. We further investigate this second set of solutions.

**Solving the linear solution**
We have search solutions for the linearised RMHD equations with a current density proportional to the magnetic field with a coefficient $k$ (Equations 3.29). The coherent structure is supposed to be located inside a cylinder of radius $a$. The equations are solved with a multipole expansion in cylindrical coordinates $(r, \theta)$, see Equation (3.31). The origin of $\theta$ is set by the direction of the velocity $u$. The solutions involve a variety of Alfvén vortices.

As a first approach, we can impose only that the magnetic field is finite at $r = 0$ and vanishes at $r \to \infty$ as well as a divergent free magnetic field. Such generic conditions, select the $r$ dependence of each mode, in particular by linking the amplitude of the solution in $r > a$ to the one in $r < a$ (through the continuity of $B_r$ components at $r = a$). However, this does not impose any condition on the mode amplitude or the $k$ value. More precisely, the condition of Equation (3.42) for the monopole is not present if the total electric current does not vanish. For the dipole and multipoles only the first equation in Equations (3.44) and (3.46) is present (due to a divergence free magnetic field). Then we can select the amplitude of the vortex and $k$ freely and the continuity of $B_R$ determines the external solution. In such case, the different modes can be superposed as in Equation (3.35), and a current layer is generically present at $r = a$.

**Properties of the modes**
However, if no net total current is present in $r \geq a$, this implies for $n = 0$ mode (monopole) the condition:

$$J_1(ka) = 0 \tag{3.49}$$

Next, if $B_\theta$ is continuous at $r = a$, this implies for one of the $n = 1$ mode (with the dipolar momentum about transverse to $\mathbf{B}_0$) and for the $n \geq 2$ modes (multipoles) the condition:

$$J_{n-1}(ka) = 0 \tag{3.50}$$

For a given vortex of radius $a$, these conditions, Equations (3.49, 3.50) imply that possible $k\,a$ values are limited to the series of $J_{n-1}$ zeros. Since these zeros are different for different $n$ values, two modes with $n \geq 2$ cannot be superposed in general. The exception is the monopole and the quadrupole ($n = 2$) which have the same condition. Finally, each $n$ mode has an arbitrary amplitude.

The parallel dipole ($n = 1$, the dipolar momentum is about parallel to $\mathbf{B}_0$) is specific since its amplitude is determined by its inclination $\varphi$ on the mean field direction. Since its amplitude is proportional to $1/J_0(ka)$, it becomes infinite for the condition required for the transverse dipole ($J_0(ka) = 0$). Then, both dipole solutions are incompatible. However, the transverse dipole is compatible with any other single mode.

**In summary**, with the constraint of no net total current and no current sheet at the vortex boundary, only the parallel dipole solution can be superposed with only one other mode solution with $n \geq 2$. This superposition writes

$$\begin{cases} A_z = \alpha\, x \left(1 - \frac{2}{k\,r}\frac{J_1(kr)}{J_0(ka)}\right) + a_n J_n(kr)\cos(n\theta + \theta_n) & r < a \\ A_z = \alpha\, x \left(1 - \frac{2}{k\,a}\frac{J_1(ka)}{J_0(ka)}\right)\frac{a^2}{r^2} + a_n J_n(ka)\left(\frac{a}{r}\right)^n \cos(n\theta + \theta_n) & r > a \end{cases} \tag{3.51}$$

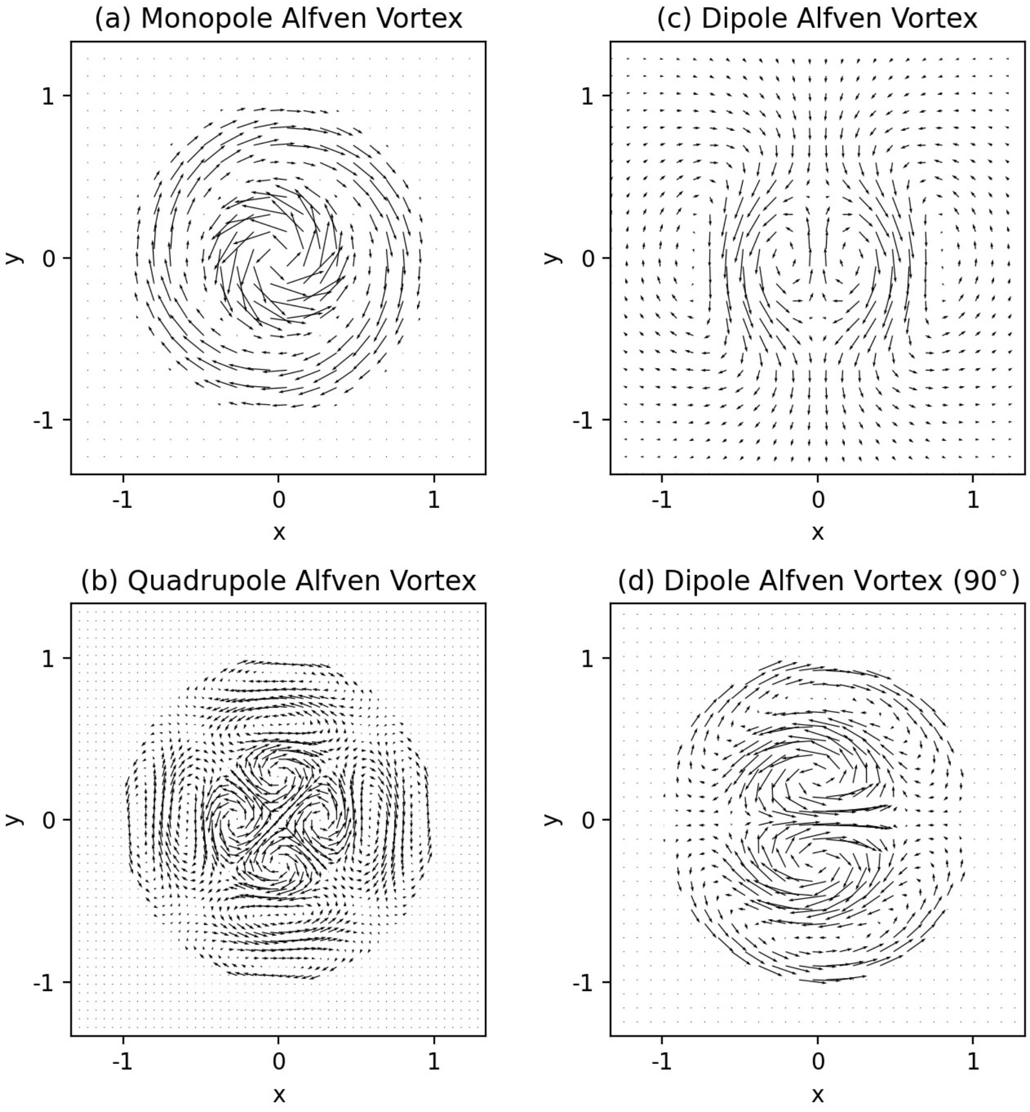
(a) Monopole Alfven Vortex

(c) Dipole Alfven Vortex

(b) Quadrupole Alfven Vortex

(d) Dipole Alfven Vortex (90°)

Figure 3.5: The magnetic field of the monopole (a), quadrupole (b), parallel (c) and transverse (d) dipole Alfvén vortices.

The superposition of the monopole, parallel dipole and quadrupole solutions writes:

$$\begin{cases} A_z = a_0 J_0(kr) + \alpha\, x \left(1 - \frac{2\alpha}{J_0(ka)}\, \frac{J_1(kr)}{k\,r}\right) + a_2 J_2(kr)\cos(2\theta+\theta_2) & r < a \\ A_z = a_0 J_0(ka) + \alpha\, x \frac{a^2}{r^2} \qquad\qquad\qquad\qquad + a_2 J_2(ka)\left(\frac{a}{r}\right)^2 \cos(2\theta+\theta_2) & r > a \end{cases} \tag{3.52}$$

where Equation (3.49) is used to simplify the expression for $r > a$.

In the above equations $a$ (vortex radius) and $a_n$ (mode amplitude) are free coefficients, while $k$ is limited to the corresponding zeros of the Bessel function ($J_{n-1}(ka) = 0$ and $J_1(ka) = 0$, respectively). The inclusion of the parallel dipole implies the motion of the Alfvén vortex at the velocity $u$, with an inclination $\varphi$ of its axis (with $\alpha = \tan\varphi$) on the local mean field $\mathbf{B}_0$. This parallel dipole, of finite amplitude, can transport with it either a mutipole ($n \geq 2$), either a monopole and a quadrupole, with arbitrary amplitude (within the RMHD limits). Finally, the magnetic field components are obtained with Equation (3.32). The magnetic field of the monopole, parallel and transverse dipole, and quadrupole are shown in Figure 3.5. Like for hydrodynamic vortices (Larichev and Reznik, 1976), it is worth to analyze the stability of these vortex solutions in the future.

# Chapter 4

# Investigation of coherent structures in the solar wind

Coherent structures are important elements of the solar wind turbulence (see Chapter 2). The nonlinearities of MHD equations cause the formation of current sheets (Frisch et al., 1983; Greco et al., 2008; Mininni et al., 2006; Greco et al., 2008; Wan et al., 2009). However, current sheets are not the only type of observed coherent structures (see Chapter 3). So the aim of this Chapter is to identify coherent structures in the turbulent solar wind at different scales and to study their physical nature. We use the time interval during the first encounter of PSP at 0.17 au as described in Sectionı 2.3. These data are unique because we can study turbulent fluctuations at large MHD scales as well as at ion scales ($\sim 100$ km) and sub-ion scales ($\sim 10$ km).

In this chapter we first discuss the method how to detect coherent structures. Then we show four examples of detected intermittent events. The first pair represent a current sheet and an Alfvén vortex. The second pair of events are, respectively, at the boundary of a switchback, and corresponds to a couple of neighboring switchbacks at the scale $\sim 10^4$ km similar to one observed by Froment et al. (2021, Figure 4). We show embedded ion and sub-ion scale structures. Finally in order to determine the dominant type of coherent structures at each range of scales, we compare observations with models and determine the probability of each type of coherent structure.

## 4.1 Local Intermittency Measure

Turbulence is a multiscale phenomenon. So we need a method that allows us to decompose the signal at different frequencies. A classical method is Fourier transform (see Chapter 2, Figure 2.1). However the signal is not homogeneous, not stationary and not periodic. So we need a more sophisticated method to detect these inhomogeneities, which are coherent structures.

A general method to detect coherent structures, based on the wavelet transform, was proposed by Farge (1992). It is summarized in Appendix B. In solar wind turbulence studies, the wavelet transform is applied to time series of the magnetic field. In order to cover the timescales up to $\tau_{max} = 10^3$ s and to avoid the boundary effects (where wavelets are ill-defined) we use a shorter time interval $T' = $ [00:22:49, 04:37:11] UT, which is determined by the intercept of $\tau = \tau_{max}$ with the cone of influence (COI) curve (see Figure B.1 in Appendix B).

The local intermittency measure (LIM) is defined as follows:

$$L(t,\tau) = \frac{\sum_{i=R,T,N} |W[B_i](t,\tau)|^2}{\langle \sum_{i=R,T,N} |W[B_i](t,\tau)|^2 \rangle_{t\in T'}} \tag{4.1}$$

where $W[B_i]$ is the wavelet transform of the component $B_i$, defined in the RTN system of coordinates so $i = R, T, N$. The value $L(t,\tau)$ measures the total magnetic energy of fluctuations at a time $t$ and at a scale $\tau$, relative to the average energy at that scale (as included in the denominator).

As an example, in Figure 4.1 we show a 30 minutes zoom within $T'$. Panel (a) gives RTN components of the measured $\mathbf{B}$ at PSP. Panel (b) shows the computed $L(t,\tau)$. The vertical elongations of enhanced $L(t,\tau)$ values are due to coupled (or coherent) phases of the fluctuations between a range of scales (Lion et al., 2016; Perrone et al., 2016; Alexandrova, 2020).

In order to illustrate the coherent events in the data, we construct an artificial signal that has the same Fourier spectrum as the original magnetic field measurements, but with random phases independently for each component (Hada et al., 2003; Koga and Hada, 2003). This synthetic signal $\mathbf{B}_{rand}$ is shown in Figure 4.1(c), while the corresponding LIM $L_{rand}(t,\tau)$ is shown in the panel (d). The energy distribution of the synthetic signal is incoherent (randomly distributed in the $(t,\tau)$–plane), i.e., peaks of $L_{rand}(t,\tau)$ at different $\tau$ are not observed at the same time. In contrast, the vertical elongations in the observed $L(t,\tau)$ correspond to magnetic fluctuations with coupled phases across scales where the elongation is observed. The high energy of these events with respect to the mean is a sign of intense coherent structures formed in the turbulent medium (e.g. Farge, 1992; Bruno, 2019). So, we observe coherent structures which extend from inertial to sub-ion timescales. Using the Taylor hypothesis (see Appendix A), the timescale range $\tau \in \tau_{all} = [10^{-2}, 10^3]$ s can be converted into the spatial range $\ell = V \cdot \tau \in [3, 3 \cdot 10^5]$ km, where $V$ is the solar wind speed.

The difference between random-phased signal and original magnetic field data suggests a methodology for detecting the central times of coherent structures. Specifically, we integrate LIM over the timescale range $\tau_{all}$:

$$I(t) = \sum_{\tau\in\tau_{all}} L(t,\tau) \tag{4.2}$$

Figure 4.2(a) shows $I(t)$ (blue-azure line), random phased integrated LIM $I_{rand}(t)$ (black line) and the threshold $I_{threshold} = \max(I_{rand}(t))$ (red horizontal line). The local maxima of $I(t) > I_{threshold}$ give the central times of the coherent structures present in the original signal. We refer below to this method as the integrated LIM selection.

The comparison of original $I(t)$ and random phased $I_{rand}(t)$ distributions is shown on Figure 4.2(b). The $I_{rand}$ distribution (in black) is close to Gaussian with a mean of 1 (because of the normalization and random phases). On the contrary, $I(t)$ (in blue-azure) has a long tail of extreme values due to the presence of coherent structures integrated over all time scales.

The integrated LIM selection does not have a predetermined scale at which the structure is searched for but it is preferentially focused on scales where the vertical enhancements in the LIM $L(t, \tau)$ are observed. Imposing $I > I_{threshold}$ we found $\sim 10^4$ isolated intermittent events.

## 4.2 Examples of embedded coherent structures

In this Section we show four examples of intermittent events among the statistics of 374 visually analyzed events with $I/I_{threshold} \geq 6$. The first three of them are presented in the article Vinogradov et al. (2023). Here we put another focus in our discussion to relate the coherent structures with the surrounding environment.

Close to the Sun the average magnetic field is directed nearly radially (Parker, 1958). However numerous changes of polarity of $B_R$ were detected in the first encounter of the PSP (Bale et al., 2019; Kasper et al., 2019). Moreover, the pitch angle of the suprathermal electrons is always anti-aligned with the magnetic field. This implies that the magnetic field lines are locally bent backward to the Sun then producing twice the observed $B_R$ change of sign. These specific reversals are called switchbacks (see Figure 1.2 and related text). They are formed of strongly folded magnetic field line connected to one solar region with a given polarity, rather than a transition region between the solar wind coming from regions with different magnetic polarities.

The physical origin of switchbacks is not yet understood, so they are actively investigated (for example, Krasnoselskikh et al., 2020; Fedorov et al., 2021). Zank et al. (2020) and Drake et al. (2021) argued that switchbacks might originate from the Sun as a consequence of interchange reconnection in the corona between open and close magnetic field lines. In contrast, Schwadron and McComas (2021) proposed that switchbacks might form further away when streams of fast and slow solar wind are interacting, so that the faster solar wind is bending the field lines of the slow solar wind located in front. Another possible mechanisms of their formation is due to the turbulence, as shown in the simulations of Squire et al. (2020) and Ruffolo et al. (2020). Finally, switchbacks can also be due to large amplitude Alfvénic fluctuations, more precisely to highly kinked Alfvénic wave packet with a nearly constant magnetic field strength (Tenerani et al., 2020).

During the first encounter, PSP was magnetically connected to a coronal hole with negative polarity $B_R < 0$. Suprathermal electrons (of energy about 314 eV) have a pitch angle $\approx 180°$ during all the 5 hours studied (and even during a longer time interval, see Kasper et al., 2019). Then, the analyzed time interval is switchback abundant. It includes the 1 h 15 time interval characterized by Perrone et al. (2020) as the interval of strong switchback activity. Below we describe in details four of the detected coherent structures, two of them being linked to switchbacks.

The event in the left column of the Figure 4.3 was observed on November 6, 2018, at $t_0$ = 00:36:27 UT. Panel (a) shows the low-pass filtered magnetic field in RTN reference frame during $\pm 1000$ seconds around the central time with $t_0$ subtracted to the observed time. It is intended to show the global environment around the event. Using the mean observed velocity, it corresponds to a scale $\sim 3 \times 10^5$ km, so of the order of injection scales (Chen et al., 2020). In this case the coherent structure, around t = 0 is associated to a discontinuity but it is not associated to a switchback (see the original data in Figure 7 of Vinogradov et al., 2023, see Appendix E).

In Figure 4.3(b-d) we show the filtered magnetic field data $\delta B_j$ at time scales defined by Equation (2.34), with $j =$*'MHD', 'ion'* and *'subion'*. We use local MVA reference frame adapted to each scale range shown (see the MVA method description in Appendix C). The segments between the panels show the zoom location on the panel located just above. The basis vectors $(\mathbf{e}_1, \mathbf{e}_2, \mathbf{e}_3)$ are directed along the maximum, intermediate and minimum variance of the magnetic field. Magnetic field components $(\delta B_1, \delta B_2, \delta B_3)$ are shown in red, green and blue in panels (b-d).

In Figure 4.3(b), a high amplitude current sheet is observed at MHD scales. In (Vinogradov et al., 2023, see Appendix E) we use the plasma data to provide a physical analysis as summarized below. We show that the Walen relation for rotational discontinuities $(\Delta\mathbf{V} = \pm\Delta\mathbf{B}/\sqrt{4\pi\rho})$ is violated in this example. In presence of pressure anisotropy, the density can change across the discontinuity, and the Walen relation is modified, as follows (Hudson, 1970; Neugebauer, 2006):

$$\begin{aligned} \Delta(A\rho) &= 0 \\ \Delta\mathbf{V} &= (\rho/\mu_0)^{1/2} A^{1/2} \Delta(\mathbf{B}/\rho) \end{aligned} \tag{4.3}$$

where $A = 1 - \mu_0(p_\parallel - p_\perp)/B^2$ is the anisotropy parameter. For this example, the pressure anisotropy correction (Hudson, 1970) is insufficient to explain the observations (Vinogradov et al., 2023). In addition, the jump of the magnetic field magnitude across the sheet $\Delta B/B_0 = 0.1$ is $\approx 2$ times greater than the standard deviation of $\Delta B/B_0$ in the 5 h interval. These properties are inconsistent with a rotational discontinuity. So we conclude that the discontinuity is tangential (Vinogradov et al., 2023). At ion and sub-ion scales (shown in panels (c) and (d) respectively) we show substructures embedded in this discontinuity. The ion scale structure resembles crossing the dipole Alfvén vortex model along the center, see Appendix D. Sub-ion scale structure might represent a compressible vortex (Jovanović et al., 2015). Indeed kinetic-scale turbulence may be described with fluid-like equations, which are structurally similar to reduced MHD equations. Therefore, it is reasonable to expect that similar types of structures can be distinguished among coherent structures on ion and subion scales.

The second event is shown in Figure 4.3 (right column) in the same format. The central time is 01:19:20 UT. It is not associated to a switchback (see the original data in Figure 8 of Vinogradov et al., 2023, see Appendix E). Low-pass filtered magnetic field component $B_R$ is negative during the interval ±100 s, as shown in the panel (f). We interpret this MHD scale structure as a monopole Alfvén vortex crossed close to its center (Vinogradov et al., 2023). Within this monopole Alfvén vortex, we observe smaller scale vortices at ion and sub-ion scales.

Figure 4.4(left column) shows a third event observed at 2:19:38 UT. $B_R$ changes sign across the sheet, meaning that the sheet forms the boundary of a switchback (see the original data in Figure 11 of Vinogradov et al., 2023, see Appendix E), similarly to observations in Krasnoselskikh et al. (2020). In panel (a) the current sheet is located at $t - t_0 = 20$ s. The velocity magnetic field jumps satisfy the Walen relation and the magnetic field magnitude is constant within the short interval $t - t_0 \in (0, 40)$ s near the center of the sheet (Vinogradov et al., 2023). So we conclude that this current sheet follows the characteristic features of rotational discontinuities. At ion scales (panel (c)) maximum ($\delta B_1$) and intermediate ($\delta B_2$) components have similar amplitudes, while $\delta B_3 \approx 0$. Both $\delta B_1$ and $\delta B_2$ are transverse to the mean magnetic field; $\delta B_1$ changes sign, and $\delta B_2$ has a peak at $t - t_0 = 0$. This is consistent with the off-center crossing of an Alfvén vortex monopole (Vinogradov et al., 2023). Sub-ion scale structure (Figure 4.4(d)) has typical properties for structures at sub-ion scales in our statistics: $\delta B_1$ has a Mexican hat-like shape, and this event has a significant compressibility $\delta|B| \sim 0.5\,\delta B_1$. It is very similar to the sub-ion scale structure shown in Figure 4.3(d). Such localized compressible magnetic fluctuations at sub-ion scales can be interpreted as the electron Alfvén vortex of Jovanović et al. (2015).

Figure 4.4(right column) shows the fourth example. In the panel (e) the lowpass filtered $B_R$ is positive in the center, indicating a possible switchback. In fact two switchbacks are present with the original data, see Figure 4.5(top panel). At ion scales we observe an embedded coherent structure that might represent a monopole Alfvén vortex crossed through the center (panel (g)). We observe a strong peak-like fluctuation of $\delta B_1$ at sub-ion scales (see panel (h)). The intermediate MVA fluctuation $\delta B_2$ is localised in the center of the event. The curve $\delta B_1$ is closely similar to the one of $\delta|B|$. So this structure is compressible $\delta|B| \sim 0.2\,\delta B_1$. It belongs to the same typical class of sub-ion scale coherent structures (compressible vortices) as the structures shown in Figures 4.3(d) and 4.4(d).

Figure 4.5 shows the ±1000 s interval around the central time of the fourth example. The top panel shows $B_R$ which attains positive values around the center while reversing to negative values shortly in the central part. The middle panel shows the pitch angle distribution of ($\sim 36$ eV) electrons, while the thermal temperature of electrons is $\sim 30$ eV (see Figure 1(e) in Vinogradov et al., 2023, see Appendix E). So this selected energy band is marginally in the suprathermal range. We still select it as the data becomes noisier at higher energies while still showing the same pattern. The maximum of the flux of electrons is observed for electrons with 180° pitch angles during the whole interval, including times when $B_R > 0$. Then $B_R$ and the pitch angle evolution show the presence of a couple of switchbacks: while the pitch angle stays 180°, $B_R$ changes its sign few times.

The bottom panel of Figure 4.5 shows the pitch angle distribution for electrons in the $\sim 2$ eV energy channel, so well in the thermal core. Still, it shows electrons moving anti parallel to the magnetic field, as for the higher energy channel shown above. It also shows electrons moving nearly along the magnetic field. However, the color bar of the bottom panel is covering a relatively small range of electron fluxes. Then, the $\sim 2$ eV electrons have an isotropic component with a flux variation of about $\pm 50\%$ for directions parallel and orthogonal to the magnetic field. In contrast, the $\sim 36$ eV electrons are highly anisotropic (with a contrast of about 100). Note, that bottom panel shows an increase of diffused electrons in pitch angles around the central time, within $\pm 300$ s. We may face trapped electrons within the switchbacks. This will be investigated in a future study.

### Summary of Examples

We collected a large statistics of coherent structures (Figure 4.2). At MHD scales some of these events represent isolated current sheets such as tangential and rotational current sheets with two examples shown in Figures 4.3(a-b) and 4.4(a-b), respectively. However, we found that current sheets are not the dominant type of coherent structures. The example in Figure 4.3(f) is interpreted as the crossing of a monopole vortex along its center (embedded in a weak and large-scale rotationnal discontinuity). Finally, the example in Figure 4.4(f) is complex.

The first pair of MHD-scale coherent structures (Figure 4.3), a tangential current sheet and an Alfvén vortex, are far from the nearest switchback. In contrast, the second pair of events represent a boundary of a switchback Figure 4.4(a,b) and even a pair of tied switchbacks as shown in Figure 4.4(e,f). Other events have typically one of these characteristics. Therefore it can be concluded that a part of the detected coherent structures on MHD scales is related to switchbacks. This is further investigated in Section 4.4.

More generally we show (Vinogradov et al., 2023), that the embedded structures at ion and sub-ion scales are mostly Alfvén vortices, independently on the existence of a current sheet at large scales. In the case of a current sheet at large scales, the sub-ion vortices are compressible and in the case of the large-scale Alfvén vortex, the small-scale vortices are incompressible. The generality of this conclusion will be studied in a future work.

## 4.3 Statistics of coherent structures at MHD, ion and subion scales

### 4.3.1 Detection and filling factor of coherent structures

We use the integrated LIM over the reduced time-scale ranges, to understand in more details the physical nature of the structures at MHD, ion and subion scales, where physics is different. So, we define integrated LIM as $I_i = (I_{MHD}, I_{ion}, I_{subion})$ over the corresponding range of timescales $\tau_j = (\tau_{MHD}, \tau_{ion}, \tau_{subion})$, defined in Equation (2.33):

$$I_j(t) = \sum_{\tau \in \tau_j} L(t, \tau) \tag{4.4}$$

Similarly, integrating $L_{rand}(t, \tau)$ over $\tau_j$ we define random phased integrated LIM $I_{rand,j}(t)$. Then, we define the central times of the structures within these scale-bands as the times of the local maxima for $I_j(t) > I_{threshold,j} = \max(I_{rand,j}(t))$.

This band-integrated LIM selection allows us to see how the number, $N$, of the structures and the filling factor $F$ change with scale band. We find a relatively small number of MHD scale structures ($N_{MHD}$ =196) with a high filling factor ($F$ = 12%), compared to $F$ = 7% and $F$ = 6% for much more numerous ion scale structures ($N_{ion}$ = 2028) and sub-ion scale structures ($N_{sub-ion}$ = 11167). We remark that our estimations of $P$ are conservative, because only the time intervals where LIM is over the threshold is counted, while coherent structures have a magnetic field which extends outside of the time where the energy of the structure is concentrated. So, the filling factor can be more than twice larger than given here. Finally, numerous small-scale events populate larger ones and may exist outside them as well.

### 4.3.2 Multiscale minimum variance analysis

We further analyse the whole set of structures detected by integrated LIM at different time-scale ranges, see equation (4.4). For all the detected events, we study the amplitude anisotropy of the measured fluctuations via minimum variance analysis (MVA). Then, we compare the observed anisotropy with the one of the model structures crossed by a spacecraft (see Chapter 3). Such synthetic crossings of different models are described in Appendix D and shown in Figure D.1.

For each coherent structure detected within the j-th range of scales we consider filtered magnetic field fluctuations $\delta\mathbf{B}_j$ at the time interval $t - t_0 \in T_{struct} = (-\tau_{max,j}, \tau_{max,j})$ in the vicinity of the structure center $t_0$, where $\tau_{max,j}$ is the maximum timescale of each scale range defined by Equation (2.34). We define the amplitude of the structure $\delta B_{struct,j}$ in the MV frame as:

$$\delta B_{struct} = \max(|\delta\mathbf{B}_j|)_{t \in T_{struct}} \tag{4.5}$$

The amplitude anisotropy of the magnetic fluctuations $\delta\mathbf{B}_j$ of the structure along the crossing trajectory is characterised by MVA eigenvalue ratios $\lambda_2/\lambda_1$ and $\lambda_3/\lambda_2$, where $\lambda_1$, $\lambda_2$ and $\lambda_3$ are the maximum, intermediate and minimum eigenvalues. The relative amplitude $\delta B_{struct,j}/B_0$ is shown in color in the Figure 4.6. For each range of scales, the number of structures $N$ and the filling factor $P$ are written in the legend of the panels.

Figure 4.6(a) gives the results of the MVA for the raw magnetic field data during 200 s time intervals around the central times $t_0$ of the MHD-scale coherent structures. The MVA results for examples shown in Figures 4.3 and 4.4 are marked on the $(\lambda_2/\lambda_1, \lambda_3/\lambda_2)$ plane with special symbols: Example-1, a tangential discontinuity at large scales, is shown with a black dot; Example-2, an Alfvén vortex at large scales, is shown with a cross; Example-3, a rotational discontinuity at large scales, is shown with a plus; and Example-4, a group of coherent structures, is shown with an odot.

Analysing all the data point in Figure 4.6, we see that the structures are regrouped, in large bands, along the two main axis. If $\lambda_3/\lambda_2) < 0.2$, the intermediate over maximum variance, $\lambda_2/\lambda_1$, can be anything, as is the case for the monopole and dipole Alfvén vortex, see Figure D.1 of Appendix D. Minimum over intermediate variance, $\lambda_3/\lambda_2$, sometime takes high values ($> 0.5$), as is the case for the monopole vortex, a tangential discontinuity or a magnetic hole. Values of $\lambda_3/\lambda_2$ around 0.3 and for small $\lambda_2/\lambda_1$ can be interpreted as rotational discontinuities, see Figure D.1. So, the observed distribution of $\lambda_3/\lambda_2$ as a function of $\lambda_2/\lambda_1$ can be due to a superposition of different types of coherent structures. From this distribution, we conclude that vortices are dominant, but other types of structures may also exist.

Figure 4.6(b) corresponds to the same set of coherent structures as in panel (a) but for filtered MHD-scale fluctuations $\delta\mathbf{B}_{MHD}$ instead of the raw magnetic field data. Here, the data are spread nearly uniformly in the bottom-left part of the panel. This is an indication that this distribution can be also interpreted as a superposition of the 5 models discussed above, with a dominance of vortices. This idea is quantified below in Section 4.3.3.

Figure 4.6(c,d) represent the MVA results for ion and sub-ion scale structures respectively. At ion scales, the distribution is similar to what is observed in raw data (we are using the merged magnetic field data without filtering), but with more cases (2028 vs 196). Sub-ion scale structures have different distribution of the MVA eigenvalue ratios. Most of the points, and especially high amplitude events, are grouped closer the left side of the eigenvalue ratios plane, where $\lambda_2/\lambda_1 < 0.25$. But this does not exclude any of the 5 models.

An additional distinguishing parameter is the compressibility of magnetic fluctuations within a coherent structure. A coherent structure is compressible, if the magnetic field magnitude $|B|$ is not constant due to the parallel magnetic fluctuations of the structure. Considering the compressibility at j-th range of scales, we filter $|B|$ as we do for fluctuations $\delta\mathbf{B}_j$. This defines $\delta|B|$ at the scale-range $j$. The amplitude of compression associated with a coherent structure is defined as $\max(|\delta|B||)_{t\in T_{struct}}$. We normalize it by $\delta B_{struct}$ to define

|  | Alfvén vortex |  | Current sheet |  | Magnetic hole | None |
|---|---|---|---|---|---|---|
|  | Monopole | Dipole | Rotational | Tangential |  |  |
| RAW MHD | 0.04 | 0.86 | 0.1 | 0 | 0 | 0 |
| MHD | 0.1 | 0.84 | 0.0 | 0 | 0 | 0.06 |
| Ion scales | 0.15 | 0.85 | 0.0 | 0 | 0 | 0 |
| Sub-ion | 0.07 | 0.49 | 0.05 | 0 | 0.004 | 0.34 |

Table 4.1: Result of the problem formulated in Equation (4.9). The numbers are the coefficients $p(\text{model})$ which correspond to the fraction of the observed coherent structures that have MVA eigenvalue ratios consistent with the crossing of a given model (Figure D.1).

the compressibility of the structure:

$$C_{struct} = \max(|\delta|B||)/\delta B_{struct} \tag{4.6}$$

We underline that our measure of compressibility differs from the definitions used in Turner et al. (1977) and Volwerk et al. (2020). It is more similar to those used in Stevens and Kasper (2007) and Perrone et al. (2016).

The compressibility of magnetic fluctuations in the full time interval is small since we found earlier on that $E_{\|}/E_{total} \sim 5{\cdot}10^{-3}$ at MHD scales and it attains the value $E_{\|}/E_{total} \sim 0.3$ at sub-ion scales (see Figure 2.4(b)). Is it also true for coherent structures? Consistent with expectations (arising from the four examples we considered in Section 4.2), we find that only subion scale coherent structures possess a significant level of compressibility. Among them, the structures with the lowest compressibility are mainly located close to the $\lambda_3/\lambda_2$-axis (which is characteristic of current sheets or vortices, see Appendix D). The most compressible structures (with $C_{struc} \geq 0.8$) account for 2.7% of the total statistics and fill the plane uniformly. Finally, there is no characteristic amplitude anisotropy for the most compressible structures.

In the following Section we compare the amplitude anisotropy and the compressibility for MHD, ion and sub-ion scale structures, with the crossings of different coherent structures models (see Appendix D).

### 4.3.3 Types of observed coherent structures

Below we compare the observational statistics of coherent structures with models. For convenience we use below the notation $(r_{32}, r_{21}) = (\lambda_3/\lambda_2, \lambda_2/\lambda_1)$ for MVA eigenvalue ratios. First, we systematically investigate the compressible coherent structures with nearly linear polarisation, such as magnetic holes (see Section 3.2). We use two criteria to select magnetic holes. First, $C_{struct} > 0.8$ ($C_{struct}$ is defined in Equation (4.6)) to select strongly compressible structures and second, we delimit the zone $(r_{32} > 0.6, r_{21} < 0.4)$ in the MVA eigenvalue ratios plane, that is characteristic for the magnetic hole crossings, see the bottom panel of Figure D.1 column (e). Their percentage at MHD, ion and subion scales is shown in the column *Magnetic hole* of Table 4.1. We found that they are observed only at sub-ion scales. Among sub-ion scale structures, they account for 0.4% of the cases. We will study these events in more details in a future work.

We define the proportions of vortices and current sheets among the remaining observed structures by comparing the amplitude anisotropy from observation (as shown in Figure 4.6) to the one of models, without imposing any criterion for compressibility.

Figure 4.7(a) show 2D histograms (6 × 6 bins) of distributions of the data in the $(r_{32}, r_{21})$–plane for raw data (top raw), observations at MHD (second raw), ion (third raw) and sub-ion (bottom raw) scales. In other words, we show the probability density $P_{obs,j}$ of observations

$$P_{obs,j}(r_{32}, r_{21}) = N_{obs,j}(r_{32}, r_{21})/N_{obs,j}, \tag{4.7}$$

where $N_{obs,j}(r_{32}, r_{21})$ is the number of the observed structures in a bin, and $N_{obs,j}$ is the total number of observed structures. The index $j$ denotes the scale range. The histograms are limited to few bins (6 × 6) to keep enough cases in bins having the largest counts in order to limit the statistical fluctuations.

We assume that crossings of coherent structures along trajectories with different impact parameters are equally probable (because crossings are random) and we take into account the noise from the observations, with Equation (D.2), in Appendix D. Since the dipole Alfvén vortex has an angular structure, we average the results over a uniform distribution of trajectory orientations. Then, we obtain the probability density $P(r_{32}, r_{21}|\text{model})$ of MVA eigenvalue ratios for each model structure:

$$P_j(r_{32}, r_{21}|\text{model}) = N_{model,j}(r_{32}, r_{21})/N_{model,j} \tag{4.8}$$

where the index $j$ denotes the scale range. The probability distributions for 4 different models $P_j(r_{32}, r_{21}|\text{model})$ are shown in columns (b-e) of Figure 4.7. To simulate different scales, we change the level of the noise according to what is observed at each scale, see Equation (D.2).

The observed distribution of MVA eigenvalue ratios $P_{obs,j}$ can be expressed as the linear combination of the conditional probabilities $P_j(r_{32}, r_{21}|\text{model})$, determined from the models. The positive coefficients $p(\text{model})$ reflect the probability to encounter each model structure. Coefficients $p(\text{model})$ are found from the constrained minimisation problem:

$$\begin{cases} ||P_{obs}(r_{32}, r_{21}) - \sum\limits_{model} p(\text{model})P(r_{32}, r_{21}|\text{model})|| \to 0 \\ \sum\limits_{model} p(\text{model}) \leq 1 \\ p(\text{model}) \geq 0 \end{cases} \tag{4.9}$$

We use the least squares minimisation. Note that no compressibility criteria is imposed, since vortices and current sheets are mostly incompressible structures. The resulting probabilities $p(\text{model})$ at different scales and for different models are shown in Table 4.1: The

MVA eigenvalues of the observed coherent structures at any scale range are most consistent with the crossings of the dipole Alfvén vortices. The monopole vortices account for $7-15\%$ of coherent structures among different scales. The rotational discontinuities are observed in raw (non-filtered) data at MHD scales only. Tangential discontinuities do not appear to be statistically significant. There is 6% of events which were not possible to model at MHD scales. Finally, the results presented in Table 4.1 doesn't change qualitatively if instead of least squares, the sum of the absolute values of probability differences (between observations and models) in each bin is minimized.

At the MHD scales applying MVA to the raw data we found 86% dipole Alfvén vortices, 4% monopole vortices and 10% rotational discontinuities. Analyzing the same structures with filtered magnetic field data at MHD scales, $(1, 100)$ s, we found 84% dipole vortices, 10% monopole vortices, and 6% unspecified structures. In fact, the discontinuities found in raw data are rarely isolated (an isolated current sheet is Example 1, Figure 4.3). Thus, while considering only time scales below 100 s, the amplitude of the jump decreases and the MVA results give properties of MHD structures around the discontinuity, as is clearly seen in Example 3, Figure 4.4(b).

On ion scales we found 85% dipole vortices and 15% of monopoles. Planar discontinuities are not found by this method.

On subion scales coherent structures represent dipole vortices (49%), monopole vortices (7%), rotational current sheets (5%) and magnetic holes (0.4%). Around 34% of sub-ion scale structures do not fit any of the considered models. It is plausible that this is a consequence of using incompressible models of vortices in comparison to observations. To improve this study at sub-ion scales in the future, the electron-scale Alfvén vortex model of Jovanović et al. (2015) should be used.

The visual classification of ion-scale coherent structures at 0.17 au, during the first PSP perihelion, has been done recently in Perrone et al. (2020). Three different time intervals were considered: quiet, weekly-disturbed and highly-disturbed solar wind. The highly-disturbed interval (of 1.5 h), with $B_R$ reversals, is a subset of the 5 h-interval considered here. The authors concluded that in the highly-disturbed interval current sheets were dominant (46%), while during the weekly-disturbed interval Alfvén vortices (45%) and wave packets (50%) were observed. This is in contrast with the quantitative classification presented above (showing that Alfvén vortices are dominant).

In the previous studies of ion scales coherent structures at 1 au in slow (Perrone et al., 2016) and fast (Perrone et al., 2017) solar wind with Cluster satellites, the dominance of Alfvén vortices with respect to current sheets has been found. These results are more consistent with our results at 0.17 au in the slow wind.

## 4.4 Filling factor from MHD to sub-ion scales

In Section 4.1 we showed that the magnetic field measured by PSP differs from the signal with random phases. Coherent structures appear on the scalogram as time-localized regions (vertically elongated) with high LIM values (Figure 4.1). However, the time interval of the scalogram is much longer than the time scales of the corresponding ion and subion scale structures. Therefore, Figure 4.1 poorly illustrates how many structures exist on ion and subion scales and how they are clustered/grouped.

Figure 4.8 shows a closer zoom (±100 s around the central time 02:54:08 UT) to the pair of switchbacks structure shown in Figures 4.4 (right column) and 4.5. The top panel shows the magnetic field data in the RTN reference frame. The radial component $B_R$ is positive during two intervals $t - t_0 \in (-25, 10)$ s and $t - t_0 \in (25, 84)$ s, indicating two neighboring switchbacks. The boundaries of both switchbacks are current sheets of ion scale thickness. Figure 4.8(bottom panel) shows the LIM scalogram. A few enhancements of $L(t, \tau)$ cover the periods corresponding to MHD range of scales $\tau > 1$ s (marked with the pink area on the left side of the bottom panel). The main structures are located around the switchback boundaries. At ion scales, marked with the green area, a transition in the enhancement organization is observed with more structures distributed on a larger fraction of the time range. Much more finer structures are present in the subion region (blue area), with a large density of structures present in an extended time interval around the switchbacks boundaries and the structures present in the MHD range. Interestingly, there are also many LIM enhancements covering $\tau < 1$ s (ion and sub-ion scales) quite far away from the switchback centers and from their boundaries, for example ones that we observe at $t - t_0 \in (-100, -75)$ s.

Next, we analyze intermittent events at each timescale $\tau$, in contrast to the above description and the approach in Section 4.3.1, where we considered timescale ranges (defined in Equation 2.34). Specifically we find time intervals when local intermittency measure is above the threshold:

$$L(t, \tau) > L_{threshold}(\tau),$$

where $L_{threshold}(\tau) = \max(L_{rand}(t, \tau))$ and $L_{rand}(t, \tau)$ is the LIM of the signal with random phases. By definition, Equation (4.1), $L(t, \tau)$ is the normalized energy of magnetic fluctuations so, the selection of events by $L(t, \tau)$ is a selection by the energy. Below we refer to them as energetic events.

We define the filling factor $F$ as the fraction of time above the threshold

$$F = \mathrm{Time}(L(t, \tau) > L_{threshold}(\tau)) \, / \, T'.$$

Then, we identify isolated events, i.e., we find continuous time intervals when $L(t, \tau) > L_{threshold}(\tau)$. $N$ denotes the number of isolated events at the scale $\tau$.

Apart from the most energetic events we are also interested in the most compressible events. To detect them we need another measure. Similarly to the approach of Perrone et al. (2016), we define intermittency of the parallel fluctuations $L_{\parallel}(t,\tau)$ as follows:

$$L_{\parallel}(t,\tau) = \frac{|W[|B|](t,\tau)|^2}{\langle |W[|B|](t,\tau)|^2 \rangle_{t\in T'}} \tag{4.10}$$

The threshold value is defined as $L_{\parallel,threshold}(\tau) = \max(L_{\parallel,rand}(t,\tau))$. In the same way as it was done above for energetic events, we determine the filling factor and the number of isolated compressible events. We note that the two families of events are not mutually exclusive: the identified compressible events probably all belong to the family of the energetic events (this could be done by comparing the central times of compressible and energetic structures). However, all energetic events are not necessarily compressible.

Figure 4.9(a) shows the number of isolated events $N$ as function of the frequency $f = 1/\tau$. The number of energetic and compressible events are shown in blue and orange lines, respectively. Both are increasing monotonously with $f$ and there is about a factor 2 to 3 less compressible events than energetic ones at all scales. There is no significant change in the relation $N(f)$ at the crossing of the ion scales. We can relate these results to our previous results on kurtosis, see sub-Section 2.3.2, with all three methods for the MHD scales, and the ones with wavelet transform for ion and subion scales, as follows. Let us consider the simple picture of turbulence having random fluctuations plus energetic events. Then, at each scale, kurtosis will increase with the number of coherent structures if they are intense enough. This may explain our observations and relate the results of Figure 4.9(a) to those of Figure 2.6.

The filling factor is shown in Figure 4.9(b). In inertial range the filling factor is decreasing according to a power law as $f^{-0.26}$ and $f^{-0.13}$ for energetic and compressible events, respectively. For both energetic and compressible events, the filling factor becomes constant at subion scales (Figure 4.9(b)) while the number $N$ of structures still grows up with the same power law than at MHD scales (Figure 4.9(a)).

Next, we investigate the duration of the coherent structures normalized by $\tau$. This normalized duration, $\Delta t$, is expected to be larger than 1 (due to the wavelet fitering at scale $\tau$). The results shown in Figure 4.9(c) indicates $\Delta t \sim 1.5$ at low frequencies, with a slight increase towards $\Delta t \sim 2$ at high frequencies. This implies that coherent structures are dominantly with a duration slightly above $\tau$, so with few oscillations, as the examples shown in Figures 4.3 and 4.4. In particular, long wave packets, with many oscilations, are not frequent.

In summary, from the energy spectrum we know that in the inertial range fluctuations are weekly compressible. The most intense magnetic field compressions are inhomogeneous since they are localized in coherent structures. The number, $N$, and filling factor, $F$ of compressible structures is smaller than energetic structures by a factor 2 to 3, and the dependence of $N$ and $F$ on timescale $\tau$ is similar for both (Figure 4.9). This is probably because all compressible events are included in the family of the energetic events. The filling factor of coherent structures is decreasing with frequency and saturates at the ion and sub-ion scales. Coherent structures have mainly few oscillations, with a duration proportional to the scale $\tau$.

In conclusion, the increase of the number of isolated events from large to small scales is observed both in the inertial range and down to subion scales. Only a part of the subion coherent structures are linked to MHD coherent structures. This finding is in agreement with observational results of Greco et al. (2016) who observed that about half of intermittent sub-ion scale structures are not isolated, but belong to a cluster of substructures formed near the ion-scale current sheet that undergoes a process of fragmentation. Similar picture with an hierarchy of sub-ion scale structures arise in fully kinetic simulations of Karimabadi et al. (2013). These results have an implication on the plasma heating since the energetic events are expected to be tightly associated to the dissipation at even smaller scales (electron scales). With PSP we have the relevant range of higher frequency to test this conjecture, but these data are not in the Merged data set used above. We leave this analysis for a future work. Still our results point to a highly fragmented dissipation in small-scale structures occupying only about 2% of the space along a 1D cut, so only about 0.04% of the 3D volume if we assumed that the coherent structures are mostly bi-dimensional (Chapter 3).

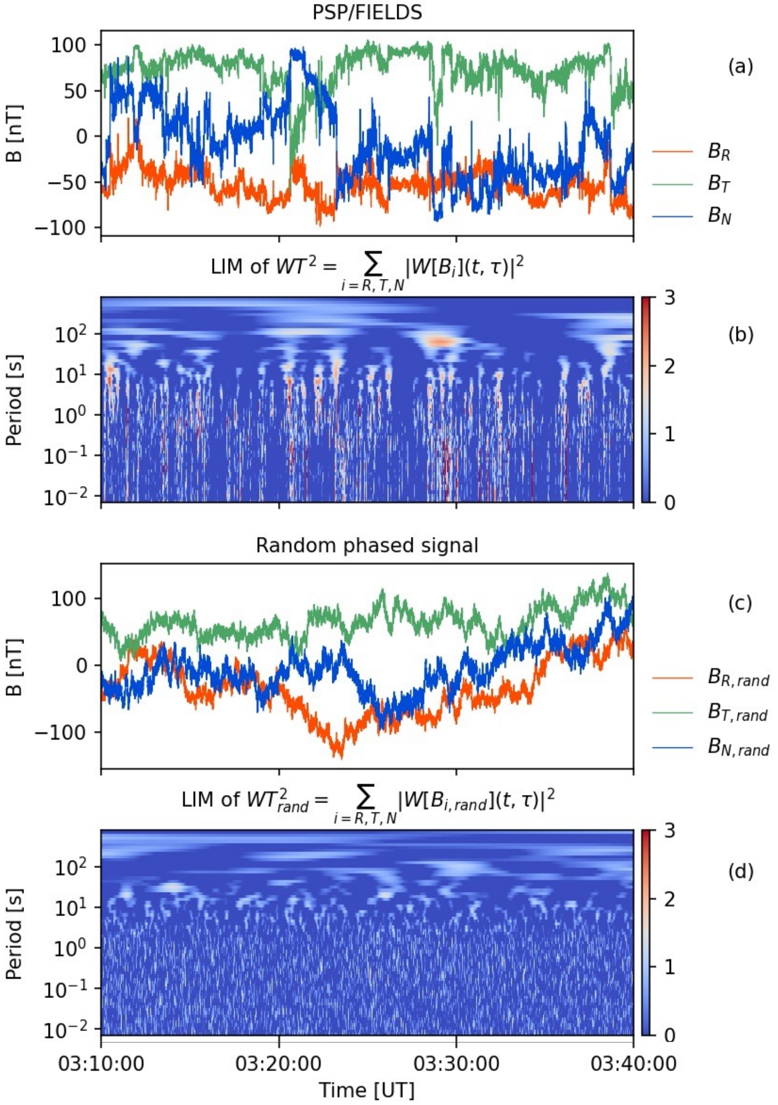

Figure 4.1: A 30 minutes zoom, $[03:10, 03:40]$ UT, within the analyzed time interval of 5 hours on November 6, 2018 of PSP data. From top to bottom: (a) magnetic field in Radial Tangential Normal (RTN) reference frame, (b) Local Intermittency Measure (LIM) of the magnetic fluctuations of the total energy $L(t,\tau)$ defined by Equation (4.1), (c) artificial magnetic field $\mathbf{B}_{rand}$ with random phases and the same Fourier amplitudes as original magnetic field measurements, (d) LIM of the artificial signal $L_{rand}(t,\tau)$. The color bar indicates the LIM level.

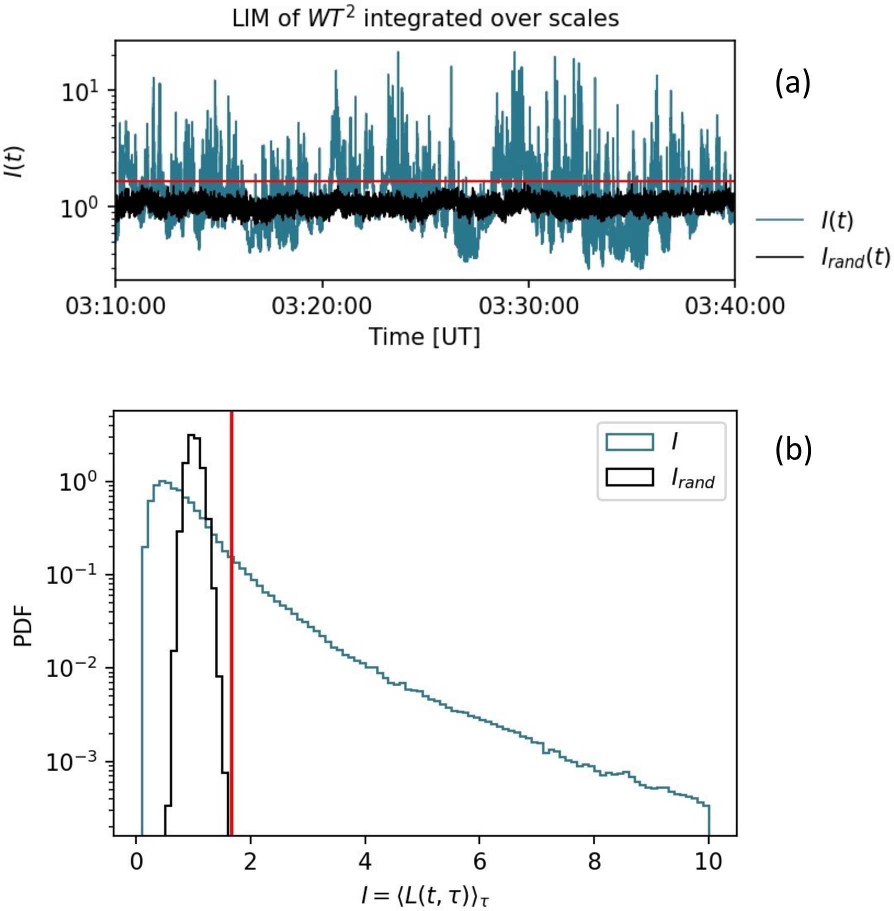

Figure 4.2: (a) the comparison of the integrated LIMs $I(t) = \langle L(t,\tau)\rangle_{\tau\in[10^{-2},10^3]\ s}$ (blue), and the $I_{rand}(t) = \langle L_{rand}(t,\tau)\rangle_{\tau\in[10^{-2},10^3]\ s}$ (black). The horizontal red line shows $I_{threshold} = \max(I_{rand}(t))$ as defined in panel (b) with a red vertical line. (b) Histograms of the integrated LIM $I(t)$ and the random phased integrated LIM $I_{rand}(t)$.

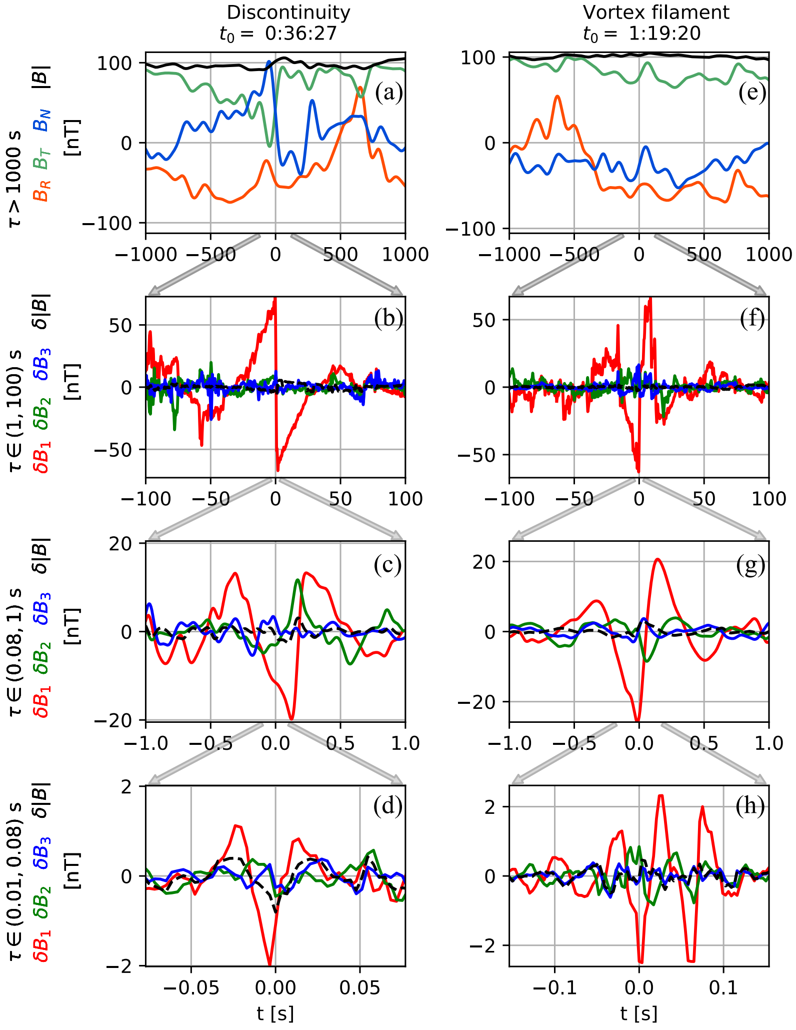

Figure 4.3: Columns show the first pair of events: a discontinuity (example 1, left) and a vortex (example 2, right). The central time of each structure $t_0$ is indicated in the title. Top row: Low-pass filtered magnetic field in RTN reference frame. Rows 2 through 4: the bandpass filtered magnetic fluctuations at MHD, ion and sub-ion frequency ranges in local MVA reference frame (see Appendix C). We note that MHD scale coherent structures contain more energy that ion-scale and sub-ion scale structures.

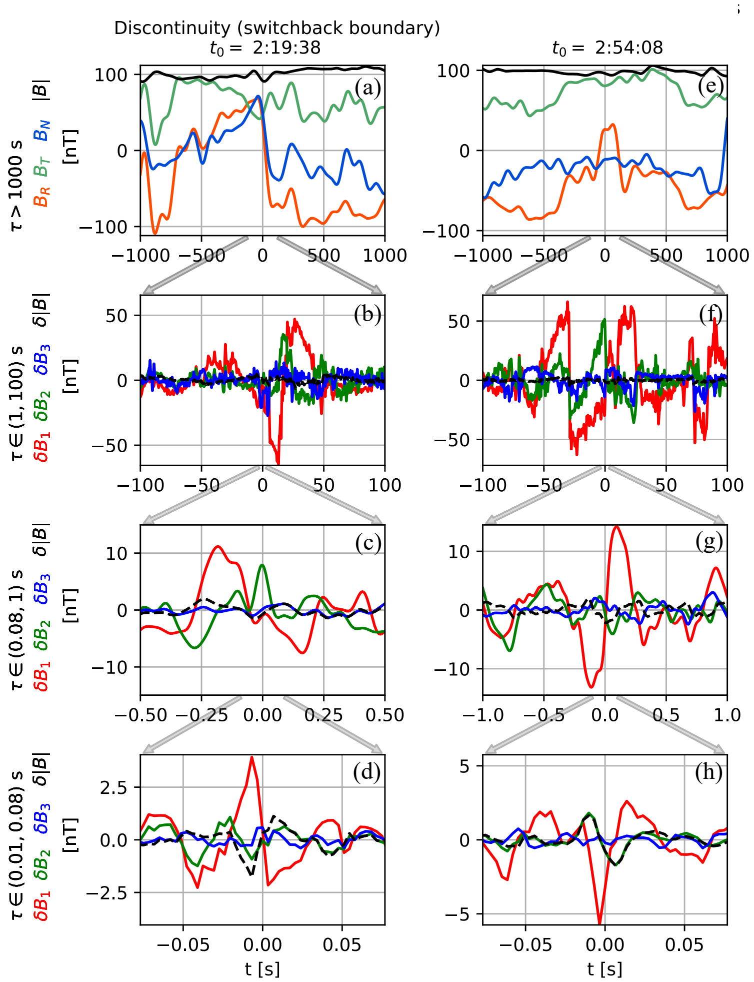

Figure 4.4: A pair of events associated to switchbacks. On the left side (example 3), a coherent structure is present around one boundary of a switchback. On the right side (example 4), two switchbacks are nearby and three coherent structures are indeed forming these switchbacks. The format is the same as in Figure 4.3.

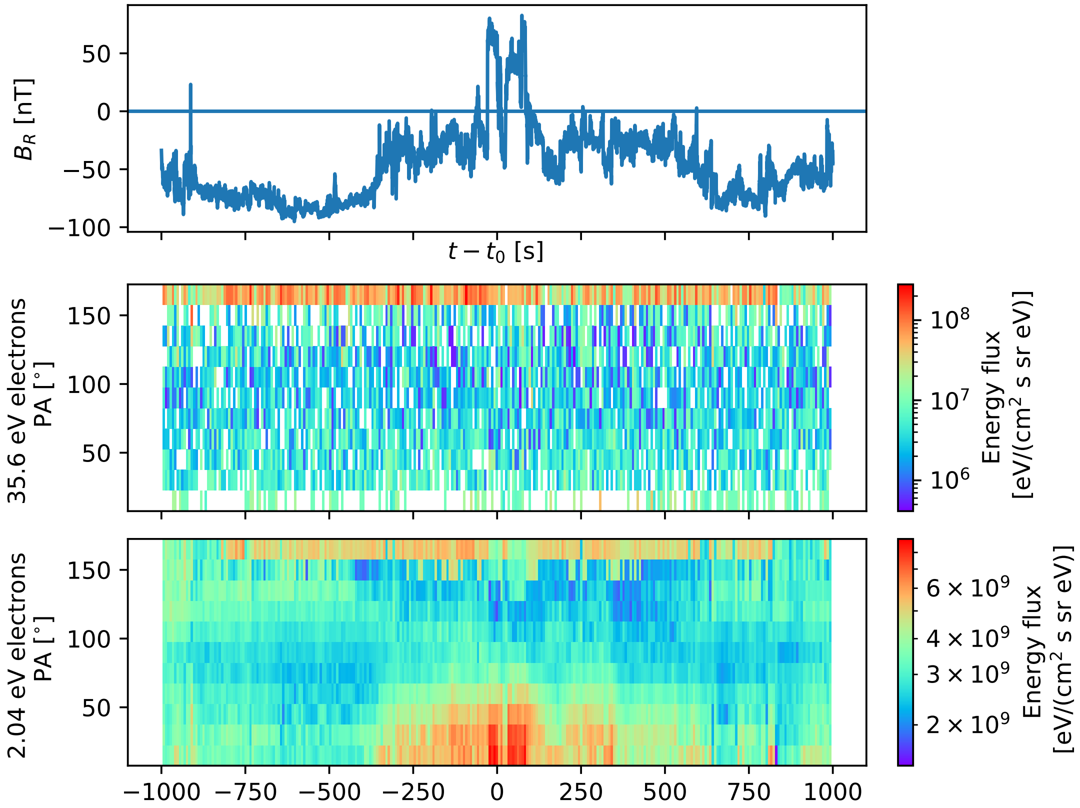

Figure 4.5: Time interval of ±1000 s around the central time 02:54:08UT when the complex structure of example 4 was observed. Top panel: Raw data of the radial magnetic field component $B_R$ showing two nearby switchbacks. Bottom panels: Electron pitch angle distributions for 36.6 eV and 2.04 eV energy channels.

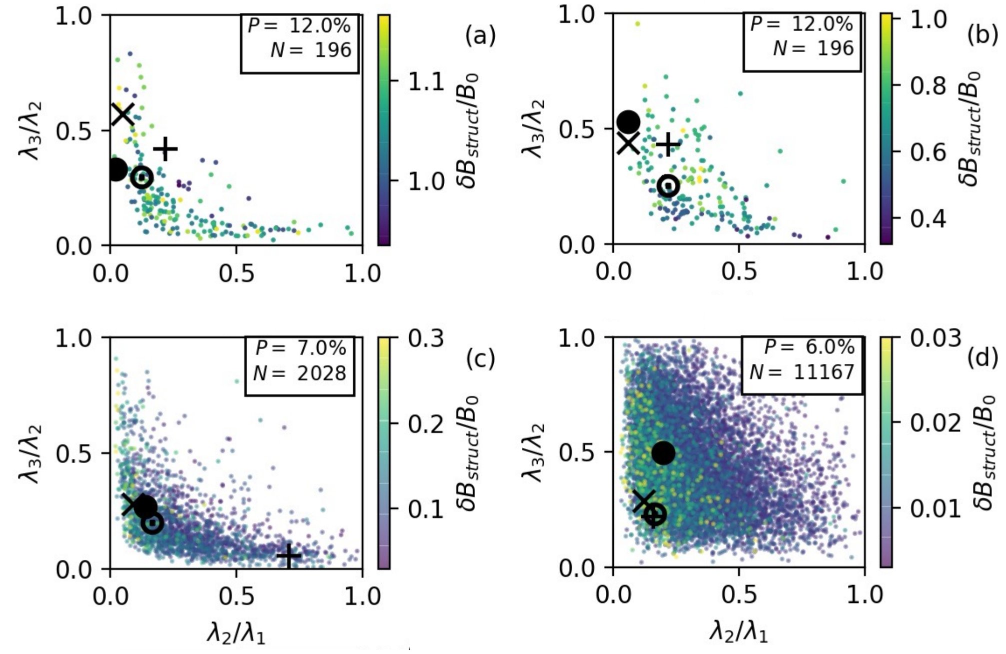

Figure 4.6: Minimum variance analysis eigenvalues ratios plane $(\lambda_2/\lambda_1, \lambda_3/\lambda_2)$: each dot corresponds to an observed coherent structure, the color gives its amplitude $\delta B_{struct}/B_0$. Panels (a,b) correspond to the raw data and MHD scales, respectively. They include 196 structures found at MHD scales. Panel (c) provides the eigenvalues ratios for 2028 structures at ion scales and panel (d) for 11167 events at sub-ion scales. The filling factor $P$ and the number of detected coherent structures $N$ at different frequency ranges are shown in the panel legends. The eigenvalue ratios of the example structures from Figures 4.3 and 4.4 are shown by the black marks: "circle", "cross", "plus" and "odot", respectively. They correspond to the example structures 1-4, respectively.

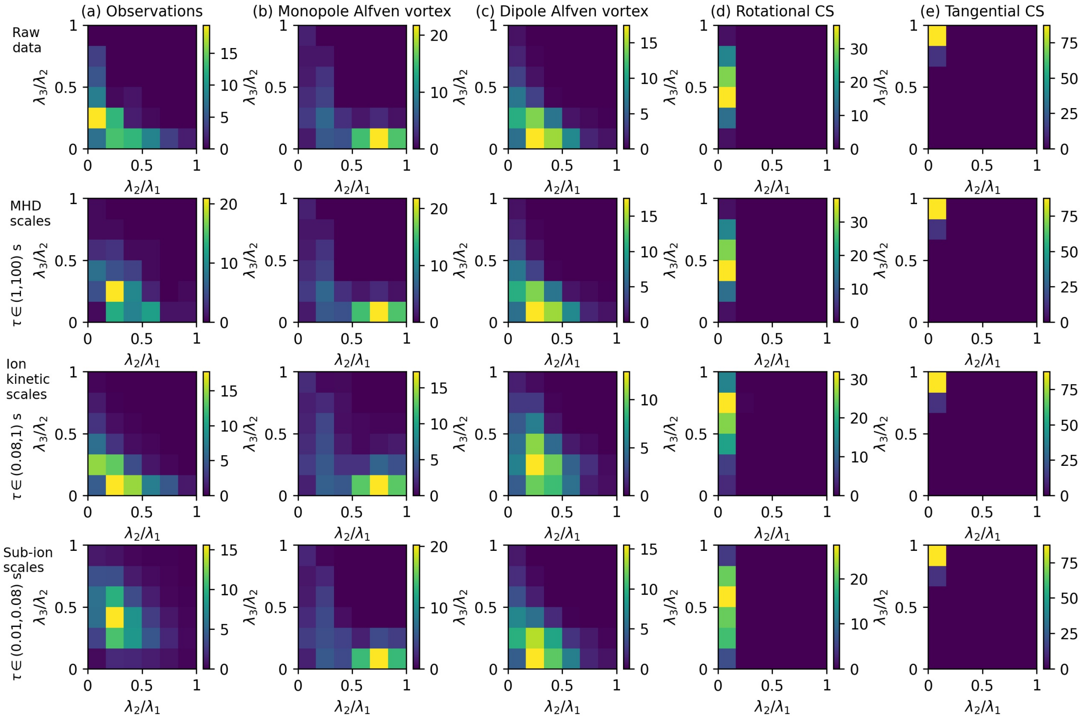

Figure 4.7: Probability distributions on the MVA eigenvalue ratios plane $(r_{32}, r_{21}) = (\lambda_3/\lambda_2, \lambda_2/\lambda_1)$. The column (a) shows the probability [%] per bin to observe a coherent structure with the corresponding MVA eigenvalue ratios (so $P_{obs,j}(r_{32}, r_{21})$ defined by Equation (4.7)). First and second panels of the column (a) show the distributions for the MHD-scale coherent structures using the raw (non-filtered) data and the MHD-range filtered data respectively. Third and fourth rows of the column (a) correspond to coherent structures detected at ion and sub-ion scale ranges respectively. Columns (b-e) show the probability densities obtained from simulating model crossings ($P_j(r_{32}, r_{21}|\text{model})$ defined by Equation (4.8)). The difference between panels in columns (b-e) is due to the different imposed noise level $\epsilon_{sim}$ as estimated from the data (see Appendix D for details).

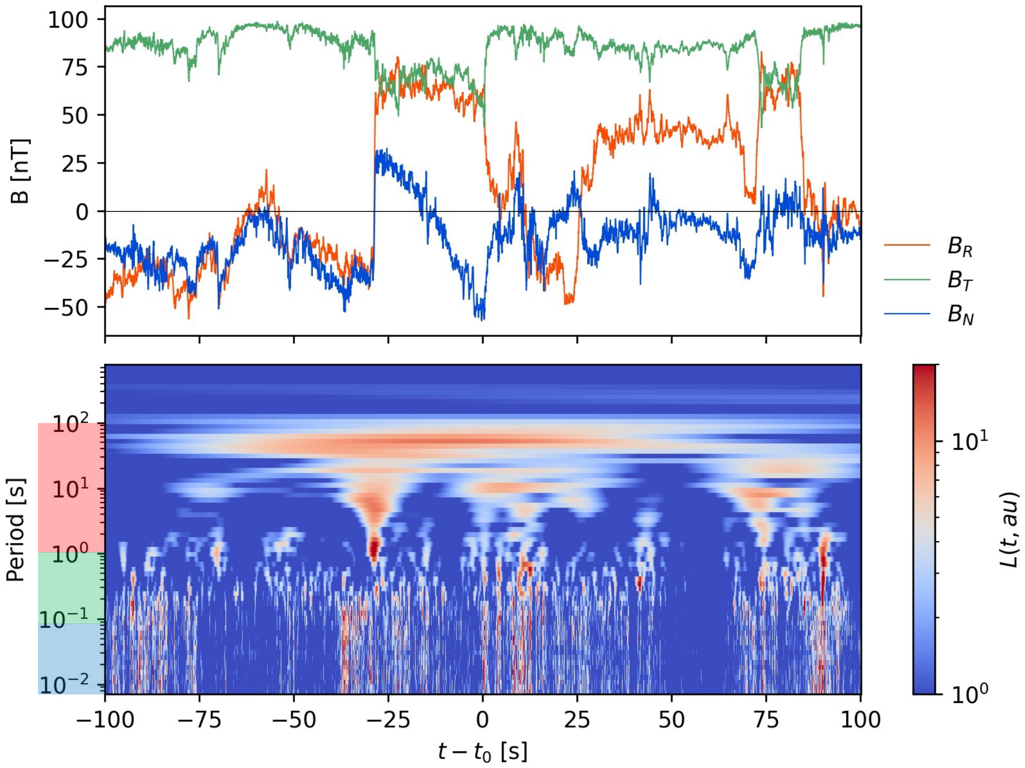

Figure 4.8: The top panel shows the raw magnetic field in RTN reference frame of example 4 during the time interval of ±100 s around 02:54:08 UT, corresponding to the center of the switchback structure shown in Figure 4.4(e-f). The bottom panel shows the local intermittency measure $L(t, \tau)$. Transparent colour bands in period-axis show the frequency ranges: MHD (red), ion (green) and subion (blue), see definition in Equation (2.34).

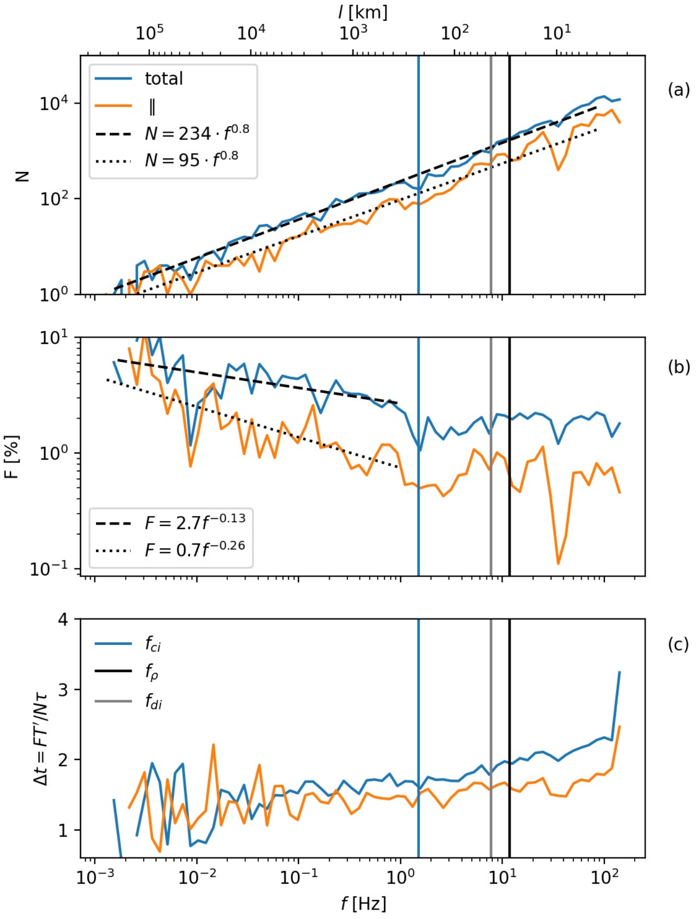

Figure 4.9: (a): Number of isolated intermittent events, as a function of frequency $f = 1/\tau$. The number of energetic events ($L(t,\tau) > L_{threshold}(\tau)$) is shown in blue line. The orange line shows the compressible events ($L_{\|}(t,\tau) > L_{\|,threshold}(\tau)$). The axis labels above the panel are showing the corresponding spatial scales $x$ (using the Taylor hypothesis, see Appendix A). (b): Percentage $F$ of time filled with intermittent events. (c): The average duration of the events detected at the given timescale $\tau = 1/f$ and normalized by $\tau$.

# Chapter 5

# Conclusion and discussion

The intermittency in the solar wind is typically investigated from the statistical point of view. As we have described in Chapter 2, in the inertial range the behavior of the structure function exponents, in function of the structure function order, deviates from linear scaling. This is usually interpreted with multifractal models of turbulence. Indeed this is a possible explanation. Another interpretation was proposed by Salem et al. (2007). They show clearly that, after removing the most energetic coherent structures, the dependence is linear (see Figure 2.3). So the physical reason of nonlinear scaling is the presence of coherent structures.

In this thesis we brought a piece of a new knowledge to the subject. We show, with Parker Solar Probe (PSP) data, that coherent structures are present not only at MHD and ion scales, but also at sub-ion scales. For the first time, we apply a multi-scale approach in physical space to investigate coherent structures and their embedding, from the MHD scales, to the smallest resolved sub-ion scales, see Section 4.2. Using plasma and magnetic field time profiles, we characterize several events in more details. The most frequently observed events are large amplitude Alfvénic (i.e., with $\delta B_\perp \simeq \delta V_\perp$ and $\delta B_\perp / B_0 \sim 1$) time-localised events at MHD scales, that can be interpreted as incompressible Alfvén vortices. These large scales vortices include inside a number of embedded incompressible ion-scale Alfvén vortices and sub-ion scale compressible vortices. Less frequently, we observe planar tangential and rotational discontinuities at MHD scales containing embedded incompressible ion-scale Alfvén vortices and sub-ion scale compressible vortices. This embedding is shown in Figures 4.3 and 4.4.

The filling factor of the structures weakly decreases with frequency (or at smaller scales). However, the number of the structures increases toward smaller scales by four orders of magnitude from MHD to sub-ion scales. No specific change in this scaling is observed at ion scales, the increase is the same across all available scales. This result indicates that the active cascade continues up to sub-ion scales. That is at odds with typically observed saturation of kurtosis of magnetic field increments at scales smaller than ion scales. This disagreement can be understood thanks to our observations at small scales: indeed, we observe only vortex like structures at sub-ion scales. Magnetic field increments are more sensitive to planar discontinuities than to vortices. Thus kurtosis of increments saturates. When the wavelet coefficients are used to calculate the kurtosis of high-pass filtered magnetic field, we rather find that the kurtosis is still increasing with frequency. We interpret this as the better detection by the Morlet wavelet transform of the increasing number of Alfvén vortices with frequency.

The analyzed time interval is switchback abundant. Some of the high amplitude MHD structures are related to switchbacks. In our example we show a rotational discontinuity present at the boundary of a switchback. This is in favor of the idea that coherent structures and switchbacks are interrelated.

Another important point of this thesis is a contribution to our understanding of Alfvén vortices. In Section 3.3 we refined the derivation of an Alfvén vortex model by providing detailed discussion of the underlying assumptions. We also generalize the model to describe the solution of the linearized reduced MHD equations with a series expansion in multipoles. If a current layer is allowed at the vortex boundary, all the terms of the series could be superposed with arbitrary amplitudes. However, imposing the continuity of the magnetic field components at the vortex boundary implies resonant[1] conditions to be achieved by most of the multipoles. One of the dipole mode is particular since it has no resonant condition but its amplitude is fixed by the inclination of the vortex axis on the mean magnetic field. Finally, we explicit how the modes could be combined, or not, in order to provide more general Alfvén vortex solutions than derived before.

Analyzing PSP data, we found that Alfvén vortices is the dominant type of structures at all scales. In Chapter 4 we derive a new method of classification of coherent structures. This method involves the comparison of the statistical properties of the observed structures with the model expectations for the amplitude anisotropy of magnetic fluctuations. The results are dominantly consistent with the crossings of the Alfvén vortex model. Only a small fraction of the structures corresponds to current sheets and magnetic holes. This result is in contrast with the conclusion of Perrone et al. (2020) at 0.17 au since they found that current sheets are more frequently observed (the 'highly perturbed' time interval analyzed in (Perrone et al., 2020) is a subset of our's). However this is in the line of Perrone et al. (2016, 2017) results at 1 au since they found that, among ion scale coherent structures, the vortices prevail both in the slow and fast solar wind.

The efficiency of the proposed classification method, in particular the percentage of each type of structures, can be tested in more controlled conditions. For example, by using 3D turbulence simulations to estimate the fraction of different types of coherent structures

---

[1] By 'resonant condition' we mean the requirement, that there is no current sheet at the cylindrical boundary of the Alfven vortex, selects a series of specific and discret modes for the internal solution (like for a resonant cavity). In contrast, if the current sheet at the boundary is allowed, it provides an additional degree of freedom and a continuum of modes is allowed.

(current sheets, vortices and magnetic holes). Alternatively, the method can be tested using the data from 4-satellite missions, such as Cluster and MMS or the future 9-satellite mission Helioswarm, since multispacecraft measurements allow to distinguish between cylindrical and flat geometries of the structures (Alexandrova et al., 2006; Roberts et al., 2016).

The results presented in this thesis are limited to a specific slow highly-perturbed (with switchbacks) solar wind region at 0.17 au from the Sun. The analysis can be expanded to different solar wind conditions in order to obtain more general results, in particular to different types of solar wind and solar source regions.

Are coherent structures formed in the solar wind turbulence or convected from the Sun? More generally, how do these structures evolve as the solar wind expands outwards? The statistics of the waiting times between the neighbouring currents sheets suggests that they are formed due to the turbulence (Vasquez et al., 2007a). But this is not a very clear evidence. Also the occurrence rate of current sheets is higher closer to the Sun (Tsurutani and Smith, 1979; Söding et al., 2001). In order to make progress in our understanding, we need to extend present study to plasma radial alignment with two spacecraft, such as PSP and Solar Orbiter, in order to follow the evolution of the same, or at least similar, plasma with solar distance.

# Appendix A

# Taylor hypothesis

Single spacecraft measurements are limited to local measurements, then it is difficult to differentiate between the temporal and spacial variations. For example, let us consider a wave mode with a wave-vector $\mathbf{k}$ and frequency $\omega$ advected with velocity $\mathbf{V}_{sw}$ by the solar wind across the spacecraft. Then, the frequency $\omega_{sc}$ of the signal measured on the spacecraft is:

$$\omega_{sc} = \omega + \mathbf{k} \cdot \mathbf{V}_{sw} \tag{A.1}$$

If the wind velocity is larger than the phase velocity of the wave, $|\omega| \ll |\mathbf{k} \cdot \mathbf{V}_{sw}|$, then the frequency of the signal measured on the spacecraft is mainly associated with the component of the wave-vector parallel to the solar wind velocity.

$$\omega_{sc} \simeq \mathbf{k} \cdot \mathbf{V}_{sw} \tag{A.2}$$

In other words, the temporal variation of the plasma and magnetic field within the spacecraft measurements is mainly associated with the spatial variation of the solar wind properties. This defines the so-called Taylor hypothesis (Taylor, 1938).

From the Equation (A.2) the direction of the wave vector is undetermined. In fact, the signal measured at the frequency $\omega_{sc}$ is a superposition of fluctuations with different wavevectors. But using additional assumptions one can associate the frequency $\omega_{sc}$ with the range of wavevectors that mainly contribute to the signal. Given that the solar wind turbulence is anisotropic with most of the energy in the fluctuations with $k$ perpendicular to $\mathbf{B}_0$ (as shown in observations Horbury et al. (2008); Podesta (2009), see discussion in Section 2.1.1), the additional condition $\mathbf{k} = k\mathbf{e}_\perp$ was imposed by Bourouaine et al. (2012) leading to the equation:

$$\omega_{sc} = kV \sin\Theta_{BV} \cos\phi \tag{A.3}$$

where $V$ is the solar wind speed, $\Theta_{BV}$ is the angle between the $\mathbf{B}$ and $\mathbf{V}$ (can be determined from the measurements); $\phi$ is the angle between the wavevector $\mathbf{k}$ and the plane containing $\mathbf{B}$ and $\mathbf{V}$ (unknown). Within the inertial range the energy follows a power law decreasing with $k_\perp$. Therefore among different possible $\mathbf{k}_\perp$, the major contribution comes from the waves with the smallest $k = |\mathbf{k}_\perp|$ since more energy is present there. This corresponds to $\phi \leq 40°$ (see Bourouaine et al., 2012). Then, as an approximation one can take $\cos\phi = 1$ in Equation (A.3).

Taylor hypothesis may not be valid when waves are highly dispersive or if the solar wind speed is low ($V < V_A$, Howes et al., 2014). In the solar wind the bulk speed $V \approx 300$ - 700 km/s exceeds the Alfvén speed $V_A = B/\sqrt{\mu_0\rho} \approx 50$ - 200 km/s in the distance range $[0.1, 1]$ au. Assuming that turbulent fluctuations can be characterized by the dispersion relation for linear waves, Howes et al. (2014) showed that the Taylor hypothesis is satisfied for Alfvén waves at MHD scales as well as for the kinetic Alfvén waves at subion scales. Only the quasi-parallel whistler waves might violate it.

In observations the Taylor hypothesis was widely used for the entire range of frequencies including the sub-ion scales. For example it is used in Kiyani et al. (2015) to convert frequency spectra to spacial spectra from MHD down to sub-ion scales (see Figure 2.1). Perri et al. (2012) used Taylor hypothesis to give an interpretation of high frequency magnetic fluctuations in terms of spatial structures - current sheets - from proton to electron kinetic scales.

# Appendix B

# Wavelet transform

Wavelet transform is a powerful tool to investigate non-stationary signals covering wide range of frequencies. Wavelets allow to analyze the signal in time as well as in frequency domain, therefore they are widely used, specifically to detect spatially localized coherent structures and measure their contribution to the energy spectrum (e.g. Farge, 1992; Bruno et al., 2001; Alexandrova et al., 2004; Lion et al., 2016).

We consider a time series $X_n$ which represents a data series. It is defined on the equally spaced time mesh $t_n = n\,\delta t$, where $n \in (0, 1, ..., N-1)$ and $\delta t$ is the time step. The wavelet transform $W_n(s)$ of the signal $X_n$ is defined as the convolution of $X_n$ with the stretched and time-shifted mother function $\psi$:

$$W_n(\tau) = \sum_{n'=0}^{N-1} X_{n'}(t_n)\,\psi^* \left[ \frac{(n'-n)\,\delta t}{\tau} \right] \tag{B.1}$$

where $*$ means the complex conjugate, $\tau$ is the scale parameter and $n$ is the time index. The summation over $n'$ provides the variable time shift in the convolution. The calculation is repeated with different $\tau$ in order to cover the desired range of timescales (or, equivalently, frequencies).

Since the signal has finite length, wavelet coefficients are influenced by edge effects. Indeed, low frequencies cannot be constrained by data which duration are shorter than $\approx \tau$. The cone of influence (COI) curve separates the region of scales where edge effects become important. The COI is a curve in the frequency-time space which allows to avoid not enough well constrained low frequency signal (large scales).

To define a wavelet transform it is essential to choose the mother function $\psi$. The general requirement for $\psi$ is that it must have zero mean and be localised in both time and frequency space (Farge, 1992; Kumar, 1994). It is clear, however, that the frequency resolution $\Delta f$ and the temporal resolution $\Delta t$ can not be small simultaneously but are linked by the uncertainty principle:

$$\Delta f \Delta t \sim \text{const.}$$

Therefore, there is a compromise to find between frequency and time resolution. There are a large variety of mother functions which can be orthogonal or non-orthogonal, complex or real. The selection of the mother function $\psi$ depend on the application and which aspect is to be optimized. In particular, the shape of the wavelet is important, since the wavelet function has to reflect approximately the features of the signal we are searching for.

The Morlet wavelet transform is based on the following mother function:

$$\psi_{Morlet}(t) = \pi^{-1/4}\, e^{-(t-t_0)^2/(2\tau^2)}\, e^{i\,\omega_0\,(t-t_0)}, \tag{B.2}$$

where $t_0$ is the central time, $\tau$ is the temporal extension, and $\omega_0$ is the parameter that defines the angular frequency of oscillations with respect of the duration of the envelope. Then, $\omega_0$ defines the number of oscillations with significant amplitude modulated behind the envelop $e^{-t^2/(2\tau^2)}$.

The Fourier transform of Equation (B.2) is still a Morlet function, but written in the Fourier space:

$$F\psi_{Morlet}(\omega) = \pi^{-1/4}\, e^{-(\omega-\omega_0)^2\,2\tau^2}\, e^{i\,t_0\,(\omega-\omega_0)}, \tag{B.3}$$

This shows that the Morlet mother function is a wave packet with an ensemble of monochromatic waves of frequencies well centered around $\omega_0$ due to the Gaussian function $\exp\left(-(\omega-\omega_0)^2\,2\tau^2\right)$ with a limited bandwith $\approx 1/\tau$. Higher values of $\tau$ provide higher frequency resolution but lower temporal resolution.

In the following we use Morlet wavelet with $\omega_0 = 6$. It implies about 3 oscillation periods with significant amplitudes (Figure B.1(a)) providing a good compromise between time and scale resolution. Compared to other wavelet transforms, Morlet wavelet has the advantage to minimize the product of the standard deviations in time and frequency, then it is broadly used. A drawback is that the set of Morlet mother functions (at various scales) are not orthogonal, then it does not provide a decomposition of the signal in an orthogonal base (like Fourier transform). Still the total energy is preserved. The comparison of power spectral density computed with Fourier and Morlet wavelet transform shows a close correspondence (Dudok de Wit et al., 2013; Lion et al., 2016). Even more, the spectra built with wavelets is much less noisy than the ones build with Fourier transform, which allows to determine more precisely the spectral slopes.

For comparison, we also present the results of wavelet transform with two other mother functions: Paul and DOG (Torrence and Compo, 1998). We show the shape of the mother functions $\psi$ for the three different wavelets: Morlet, Paul and Dog in the panels (a-c) on the left hand side of the Figure B.1.

In order to illustrate the differences between the wavelet transforms we apply them to the test signal shown with a blue curve at the top of the right panels. The test signal is built to represent the typical features present in the data. It is the superposition of a small-amplitude uniform Gaussian noise and 3 high-amplitude events including: a wave packet with the central wave period $\tau_0 = 0.8$ s bounded by the Gaussian envelope, a step function with thickness $dt = \tau_0 = 0.8$ s and a peak function with the same duration.

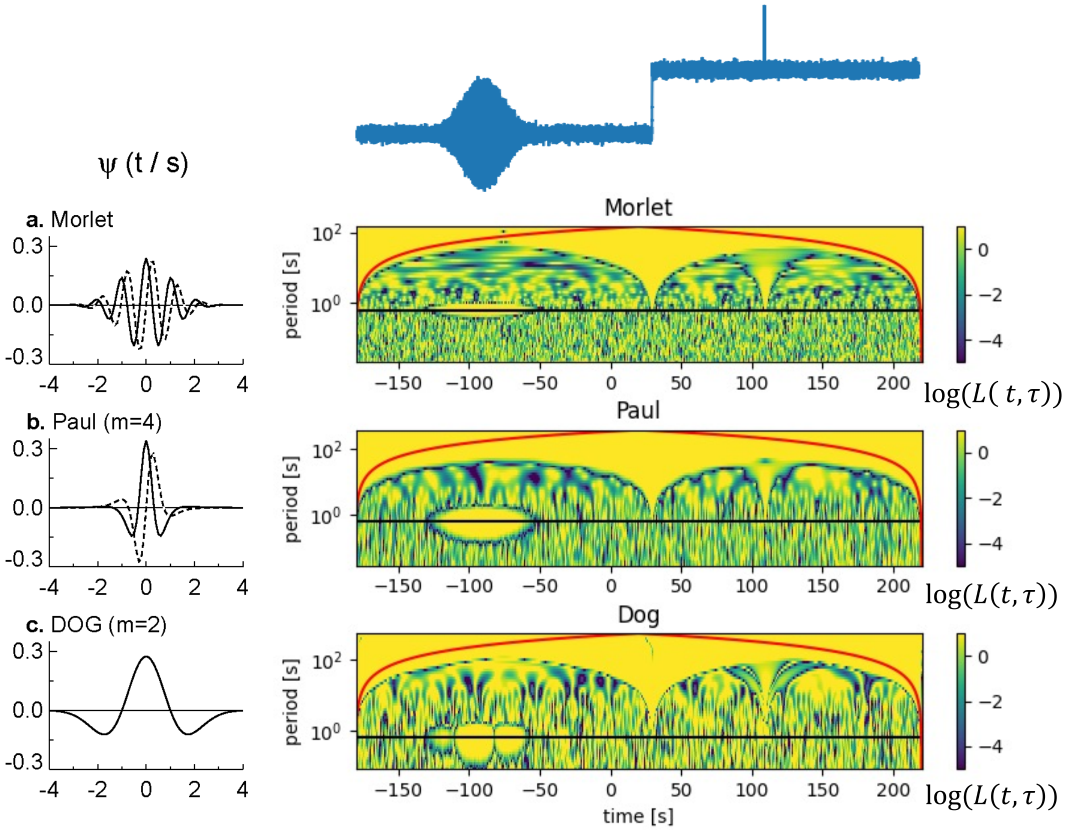

Figure B.1: Tests of wavelet transforms with different mother functions applied to a synthetic signal. Left: Panels (a-c) show the mother functions $\psi$ of different wavelets: Morlet (or Gabor), Paul, and Dog respectively. Right top: synthetic signal with various contributions: Gaussian noise, a wave packet, a sharp variation (discontinuity-like) and a peak. Right three panels below: Comparison of the LIM scalograms of the test signal (top right panel) calculated with different wavelets. The horizontal black line shows the timescale, equal to the central wavelength of the wave packet, the thickness of the sharp variation and of the peak. The red curve shows the cone of influence, delimiting the wavelet coefficients, above that line, that are poorly defined due to the boundary effects (due to finite duration of the signal).

The right panels in Figure B.1 are showing the scalograms of LIM $L(t, \tau)$ (as defined by Equation (4.1)). The noise is filling the scalogram with uncorrelated uniformly distributed minima and maxima. This is similar to the results obtained by imposing random phases to the PSP signal (see Figure 4.1(d)). The black horizontal line shows the timescale $\tau_0$. The wave packet can be identified in the scalogram at the timescale $\tau_0$ during the long time interval $t \in (-130, -50)$. In contrast, the 'smooth discontinuity' (at $t = 30$ s) and the peak (at $t = 105$ s) are causing the increased values of LIM $L(t, \tau)$ localized in time and delocalized in periods with periods larger than the timescale of the structure (so with $\tau > \tau_0$).

The wave packet in the test signal is formed by monochromatic waves having nearby frequencies. This implies an intrinsic extension of periods in the scalogram. For different mother functions, smaller width in periods in the scalogram means higher frequency resolution of the wavelet. The Morlet wavelet has a good frequency resolution unlike DOG and Paul wavelets. The Morlet wavelet transform also identifies well the temporal extension of the wave packet. Finally, the step and peak functions of the signal are well identified both in time and periods by the three mother functions.

The frequency resolution of the Morlet wavelet can be increased if we use larger value of $\omega_0$. However, a better frequency resolution means a poorer temporal resolution, while a good temporal resolution is required for determination of the central times of the coherent structures. Since we are mainly interested in coherent structures, Morlet wavelet with $\omega_0 = 6$ is appropriate, and we do not need higher frequency resolution.

# Appendix C

# MVA analysis

The Minimum Variance Analysis (MVA) method (Sonnerup and Scheible, 1998) was initially used to determine the basis $(\mathbf{e}_1, \mathbf{e}_2, \mathbf{e}_3)$ associated with a current layer. The directions of the largest $(\mathbf{e}_1)$, intermediate $(\mathbf{e}_2)$ and smallest $(\mathbf{e}_3)$ magnetic field variances are determined by minimizing the functional of the direction $\mathbf{e}$:

$$\sigma^2(\mathbf{e}) = \frac{1}{N} \sum_{i=1}^{N} \|(\vec{B}^i - < \vec{B} >) \cdot \mathbf{e}\| \tag{C.1}$$

with the condition $\|\mathbf{e}\|^2 = 1$ is fulfilled and where $N$ is the number of data points. This conditional extremum problem is solved by introducing the Lagrange multiplier $\lambda$:

$$\frac{\partial}{\partial \mathbf{e}_x}(\sigma^2 - \lambda\,(\|\mathbf{e}\|^2 - 1)) = 0 \tag{C.2}$$

$$\frac{\partial}{\partial \mathbf{e}_y}(\sigma^2 - \lambda\,(\|\mathbf{e}\|^2 - 1)) = 0 \tag{C.3}$$

$$\frac{\partial}{\partial \mathbf{e}_z}(\sigma^2 - \lambda\,(\|\mathbf{e}\|^2 - 1)) = 0 \tag{C.4}$$

Thus the problem reduces to find the eigenvalues and eigenvectors for the matrix

$$M_{\eta\nu} =< B_\eta B_\nu > - < B_\eta >< B_\nu > \tag{C.5}$$

so to solve the linear system of equations:

$$\sum_{\nu=1}^{3} M_{\eta\nu}\, \mathbf{e}_\nu = \lambda\, \mathbf{e}_\eta \tag{C.6}$$

The eigenvectors form an orthogonal basis $(\mathbf{e}_1, \mathbf{e}_2, \mathbf{e}_3)$ corresponding to the direction of the largest, intermediate, and minimum variance of the magnetic field. The eigenvalues $\lambda_1$, $\lambda_2$ and $\lambda_3$ are real and positive ($M_{\eta\nu}$ is real and symmetric).

When the MVA method is applied to a current layer the direction of $\mathbf{e}_1$ corresponds to the tangential magnetic field component which changes sign and has the largest jump across the current layer. $\mathbf{e}_1$ is typically accurately determined. However, the other two basis vectors have typically close and low eigenvalues (corresponding to small variation of the magnetic field components across the current layer). Then, these two eigen vectors are determined up to a rotation around $\mathbf{e}_1$ direction.

When the MVA method is applied to an Alfvén vortex, $\mathbf{e}_1$ is also typically well determined if the impact parameter is small (closest distance of the trajectory to the vortex axis normalized by the vortex radius). It corresponds to the azimuthal magnetic field component (see Appendix D). The quality of the MVA frame, to approximate the local Alfvén vortex frame, is degrading as the impact parameter increases.

# Appendix D

# Model structures crossings

We describe the analysis of five type of coherent structures described by simple models as shown in the first row of Figure D.1 (see Chapter 3 for a description of the models). We simulate a series of structure crossings with a range of impact parameters. The simulated magnetic field components, for trajectory crossing the structure center, are shown in the second row of Figure D.1. Plotting hodographs of the simulated data is a way to visually differentiate the models. The results of both off-center (blue) and central (black) crossing trajectories are shown in the third line of Figure D.1.

In order to compare with the observational results of PSP we need to add a level of noise similar to the one present in observations. The incoherent noise affects both the frame and the eigenvalues deduced from the MVA (Chapter C). The eigenvalue ratios are shown in the bottom row of the Figure D.1 for five types of coherent structures. The greater is the ratio $\epsilon = \delta B_{noise}/\delta B_{struct}$, the closer are $\lambda_2/\lambda_1$ and $\lambda_3/\lambda_2$) to 1 (since there is no privileged direction for a fully noisy signal). Therefore, we need to estimate $\epsilon$ from observations to take into account the noise in the model crossings.

For each band of scales we characterize the amplitude of incoherent fluctuations as follows:

$$\sigma_{noise,j} = \mathrm{std}(\delta B_j(t \in T_{\text{no struct}})) \tag{D.1}$$

where $T_{\text{no struct}} = \mathrm{Time}(I_j(t) < I_{threshold,j})$, so the time intervals without coherent struc-

| | $\langle \epsilon_{obs} \rangle$ | $\sigma(\epsilon_{obs,j})$ |
|---|---|---|
| RAWDATA MHD | 0.11 | 0.03 |
| MHD | 0.11 | 0.03 |
| Ion scales | 0.15 | 0.05 |
| Sub-ion | 0.12 | 0.03 |

Table D.1: The mean and the standard deviation of the relative noise level $\epsilon_{obs}$ at different ranges of scales (defined in Equation (D.2)).

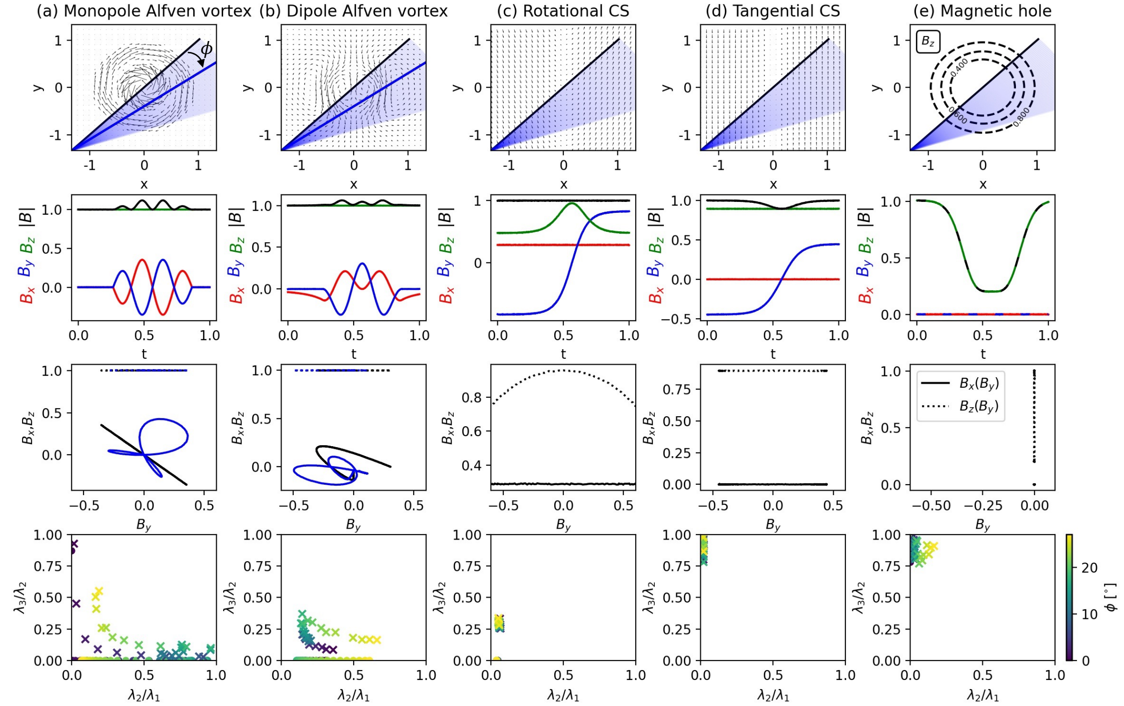

Figure D.1: Simulation of the spacecraft crossing (a) a monopole Alfvén vortex, (b) a dipole vortex, (c) a rotational and (d) a tangential discontinuity, and (e) a magnetic hole. The first row shows the magnetic field vector in the plane perpendicular to the background magnetic field. The sector, shown in blue, is a set of trajectories crossing the structure at different angles in order to collect statistics of MVA eigenvalues. The panels in the second line show the magnetic field in the MVA frame of reference, as it would be measured by the spacecraft if it crosses the structure along the black trajectory. Panels in the third line show the hodograph - indicating polarisation for off-center (blue) and central (black) trajectories. The bottom row shows the eigenvalue ratios for the set of trajectories shown within the blue cone in the first row in the presence of noise, with $\epsilon = 0.001$ (circles) and $\epsilon = 0.1$ (crosses). The trajectory angle $\phi$, defined in the top left panel, is coded with colors (see the color scale at the right bottom). Each dashed line shows the boundary of the regions on the eigenvalue ratios plane that is consistent with crossing the given model of structures in the presence of the noise level $\epsilon \in (0, 0.1)$.

tures.

For each structure at the j-th scale range we calculate the ratio of the noise $\sigma_{noise,j}$ (defined in Equation (D.1)) to the amplitude of the structure $\delta B_{struct,j}$:

$$\epsilon_{obs,j} = \sigma_{noise,j}/\delta B_{struct,j} \tag{D.2}$$

At each range of scales the distribution of $\epsilon_{obs,j}$ is nearly Gaussian, but with different values of their parameters. The mean values $\langle\epsilon_{obs,j}\rangle$ and the standard deviations $\sigma(\epsilon_{obs,j})$ are shown in Table D.1.

We repeated the crossings simulation with 10 different relative amplitudes of the imposed noise $\epsilon_{sim}$ following the Gaussian distribution deduced from observations, so with the same parameters, $\langle\epsilon_{obs,j}\rangle$ and $\sigma(\epsilon_{obs,j})$, as in observations. The obtained results of the model crossings with different $\epsilon_{sim}$ are used in Section 4.3.2.

# Appendix E

# Article submitted to ApJ: Vinogradov et al. (2023)

The article ”Embedded coherent structures from MHD to sub-ion scales in turbulent solar wind at 0.17 AU”, Vinogradov et al. (2023), is submitted to ApJ. It is accessible in arXiv at https://arxiv.org/abs/2307.10478.

# Bibliography

Alexandrova, O. (2008). Solar wind vs magnetosheath turbulence and Alfvén vortices. *Nonlinear Processes in Geophysics*, 15(1):95–108.

Alexandrova, O. (2020). *Solar Wind Turbulence: in-situ observations from magneto-fluid to kinetic plasma scales.* Habilitation à diriger des recherches, Observatoire de Paris, Université Paris Sciences et Lettres (PSL).

Alexandrova, O., Carbone, V., Veltri, P., and Sorriso-Valvo, L. (2008). Small-Scale Energy Cascade of the Solar Wind Turbulence. *Astrophys. J.*, 674(2):1153–1157.

Alexandrova, O., Chen, C. H. K., Sorriso-Valvo, L., Horbury, T. S., and Bale, S. D. (2013). Solar Wind Turbulence and the Role of Ion Instabilities. *Space Sci. Rev.*, 178(2-4):101–139.

Alexandrova, O., Jagarlamudi, V. K., Hellinger, P., Maksimovic, M., Shprits, Y., and Mangeney, A. (2021). Spectrum of kinetic plasma turbulence at 0.3-0.9 astronomical units from the Sun. *Phys. Rev. E*, 103(6):063202.

Alexandrova, O., Lacombe, C., Mangeney, A., Grappin, R., and Maksimovic, M. (2012). Solar Wind Turbulent Spectrum at Plasma Kinetic Scales. *Astrophys. J.*, 760:121.

Alexandrova, O., Mangeney, A., Maksimovic, M., Cornilleau-Wehrlin, N., Bosqued, J. M., and André, M. (2006). Alfvén vortex filaments observed in magnetosheath downstream of a quasi-perpendicular bow shock. *Journal of Geophysical Research (Space Physics)*, 111(A12):A12208.

Alexandrova, O., Mangeney, A., Maksimovic, M., Lacombe, C., Cornilleau-Wehrlin, N., Lucek, E. A., DéCréAu, P. M. E., Bosqued, J. M., Travnicek, P., and Fazakerley, A. N. (2004). Cluster observations of finite amplitude Alfvén waves and small-scale magnetic filaments downstream of a quasi-perpendicular shock. *Journal of Geophysical Research (Space Physics)*, 109(A5):A05207.

Alexandrova, O. and Saur, J. (2008). Alfvén vortices in Saturn's magnetosheath: Cassini observations. *Geophys. Res. Lett.*, 35(15):L15102.

Alexandrova, O., Saur, J., Lacombe, C., Mangeney, A., Mitchell, J., Schwartz, S. J., and Robert, P. (2009). Universality of Solar-Wind Turbulent Spectrum from MHD to Electron Scales. *Phys. Rev. Lett.*, 103(16):165003–+.

Alfvén, H. (1942). Existence of Electromagnetic-Hydrodynamic Waves. *Nature*, 150(3805):405–406.

Artemyev, A. V., Angelopoulos, V., and Vasko, I. Y. (2019). Kinetic Properties of Solar Wind Discontinuities at 1 AU Observed by ARTEMIS. *Journal of Geophysical Research (Space Physics)*, 124(6):3858–3870.

Bale, S. D., Badman, S. T., Bonnell, J. W., Bowen, T. A., Burgess, D., Case, A. W., Cattell, C. A., Chandran, B. D. G., Chaston, C. C., Chen, C. H. K., Drake, J. F., de Wit, T. D., Eastwood, J. P., Ergun, R. E., Farrell, W. M., Fong, C., Goetz, K., Goldstein, M., Goodrich, K. A., Harvey, P. R., Horbury, T. S., Howes, G. G., Kasper, J. C., Kellogg, P. J., Klimchuk, J. A., Korreck, K. E., Krasnoselskikh, V. V., Krucker, S., Laker, R., Larson, D. E., MacDowall, R. J., Maksimovic, M., Malaspina, D. M., Martinez-Oliveros, J., McComas, D. J., Meyer-Vernet, N., Moncuquet, M., Mozer, F. S., Phan, T. D., Pulupa, M., Raouafi, N. E., Salem, C., Stansby, D., Stevens, M., Szabo, A., Velli, M., Woolley, T., and Wygant, J. R. (2019). Highly structured slow solar wind emerging from an equatorial coronal hole. *Nature*, 576(7786):237–242.

Balikhin, M. A., Sibeck, D. G., Runov, A., and Walker, S. N. (2012). Magnetic holes in the vicinity of dipolarization fronts: Mirror or tearing structures? *Journal of Geophysical Research (Space Physics)*, 117(A8):A08229.

Balogh, A., Forsyth, R. J., Lucek, E. A., Horbury, T. S., and Smith, E. J. (1999). Heliospheric magnetic field polarity inversions at high heliographic latitudes. *Geophys. Res. Lett.*, 26(6):631–634.

Barnes, A. (1966). Collisionless Damping of Hydromagnetic Waves. *Physics of Fluids*, 9(8):1483–1495.

Barnes, A. (1979). Hydromagnetic waves and turbulence in the solar wind. In Parker, E. N., Kennel, C. F., and Lanzerotti, L. J., editors, *Solar System Plasma Physics*, volume 1, pages 249–319.

Baumgärtel, K. (1999). Soliton approach to magnetic holes. *J. Geophys. Res.*, 104(A12):28295–28308.

Baumjohann, W. and Treumann, R. A. (1997). *Basic Space Plasma Physics.* Imperial College Press.

Bavassano, B., Dobrowolny, M., Mariani, F., and Ness, N. F. (1982). Radial evolution of power spectra of interplanetary Alfvénic turbulence. *J. Geophys. Res.*, 87(A5):3617–3622.

Belcher, J. W. and Davis Jr., L. (1971). Large-amplitude alfvén waves in the interplanetary medium, 2. *Journal of Geophysical Research (1896-1977)*, 76(16):3534–3563.

Benzi, R. and Toschi, F. (2023). Lectures on turbulence. *Physics Reports*, 1021:1–106. Lectures on turbulence.

Biskamp, D. (1993). *Nonlinear magnetohydrodynamics*.

Biskamp, D. (2003). *Transition to turbulence*, page 33–64. Cambridge University Press.

Borovsky, J. E. (2008). Flux tube texture of the solar wind: Strands of the magnetic carpet at 1 AU? *Journal of Geophysical Research (Space Physics)*, 113(A8):A08110.

Bourouaine, S., Alexandrova, O., Marsch, E., and Maksimovic, M. (2012). On Spectral Breaks in the Power Spectra of Magnetic Fluctuations in Fast Solar Wind between 0.3 and 0.9 AU. *Astrophys. J.*, 749(2):102.

Bowen, T. A., Bale, S. D., Bonnell, J. W., Dudok de Wit, T., Goetz, K., Goodrich, K., Gruesbeck, J., Harvey, P. R., Jannet, G., Koval, A., MacDowall, R. J., Malaspina, D. M., Pulupa, M., Revillet, C., Sheppard, D., and Szabo, A. (2020a). A Merged Search-Coil and Fluxgate Magnetometer Data Product for Parker Solar Probe FIELDS. *Journal of Geophysical Research (Space Physics)*, 125(5):e27813.

Bowen, T. A., Mallet, A., Bale, S. D., Bonnell, J. W., Case, A. W., Chandran, B. D. G., Chasapis, A., Chen, C. H. K., Duan, D., Dudok de Wit, T., Goetz, K., Halekas, J. S., Harvey, P. R., Kasper, J. C., Korreck, K. E., Larson, D., Livi, R., MacDowall, R. J., Malaspina, D. M., McManus, M. D., Pulupa, M., Stevens, M., and Whittlesey, P. (2020b). Constraining Ion-Scale Heating and Spectral Energy Transfer in Observations of Plasma Turbulence. *Phys. Rev. Lett.*, 125(2):025102.

Bruno, R. (2019). Intermittency in Solar Wind Turbulence From Fluid to Kinetic Scales. *Earth and Space Science*, 6(5):656–672.

Bruno, R., Bavassano, B., and Villante, U. (1985). Evidence for long period Alfvén waves in the inner solar system. *J. Geophys. Res.*, 90(A5):4373–4377.

Bruno, R. and Carbone, V. (2013). The Solar Wind as a Turbulence Laboratory. *Living Reviews in Solar Physics*, 10(1):2.

Bruno, R., Carbone, V., Veltri, P., Pietropaolo, E., and Bavassano, B. (2001). Identifying intermittency events in the solar wind. *Planetary Spa. Sci.*, 49(12):1201–1210.

Bruno, R., Carbone, V., Vörös, Z., D'Amicis, R., Bavassano, B., Cattaneo, M. B., Mura, A., Milillo, A., Orsini, S., Veltri, P., Sorriso-Valvo, L., Zhang, T., Biernat, H., Rucker, H., Baumjohann, W., Jankovičová, D., and Kovács, P. (2009). Coordinated Study on Solar Wind Turbulence During the Venus-Express, ACE and Ulysses Alignment of August 2007. *Earth Moon and Planets*, 104(1-4):101–104.

Burlaga, L. F., Lemaire, J. F., and Turner, J. M. (1977). Interplanetary current sheets at 1 AU. *J. Geophys. Res.*, 82(22):3191.

Buti, B., Tsurutani, B. T., Neugebauer, M., and Goldstein, B. E. (2001). Generation mechanism for magnetic holes in the solar wind. *Geophys. Res. Lett.*, 28(7):1355–1358.

Carbone, V. (1993). Cascade model for intermittency in fully developed magnetohydrodynamic turbulence. *Phys. Rev. Lett.*, 71(10):1546–1548.

Carbone, V. and Pouquet, A. (2009). An Introduction to Fluid and MHD Turbulence for Astrophysical Flows: Theory, Observational and Numerical Data, and Modeling. In Cargill, P. and Vlahos, L., editors, *Turbulence in Space Plasmas*, volume 778, page 71.

Carbone, V., Veltri, P., and Bruno, R. (1996). Solar wind low-frequency magnetohydrodynamic turbulence: extended self-similarity and scaling laws¡/a¿. *Nonlinear Processes in Geophysics*, 3(4):247–261.

Carbone, V., Veltri, P., and Mangeney, A. (1990). Coherent structure formation and magnetic field line reconnection in magnetohydrodynamic turbulence. *Physics of Fluids A*, 2(8):1487–1496.

Cassak, P. A., Drake, J. F., and Shay, M. A. (2006). A Model for Spontaneous Onset of Fast Magnetic Reconnection. *Astrophys. J. Lett.*, 644(2):L145–L148.

Chandran, B. D. G., Li, B., Rogers, B. N., Quataert, E., and Germaschewski, K. (2010). Perpendicular Ion Heating by Low-frequency Alfvén-wave Turbulence in the Solar Wind. *Astrophys. J.*, 720(1):503–515.

Chandran, B. D. G. and Perez, J. C. (2019). Reflection-driven magnetohydrodynamic turbulence in the solar atmosphere and solar wind. *Journal of Plasma Physics*, 85(4):905850409.

Chandran, B. D. G., Verscharen, D., Quataert, E., Kasper, J. C., Isenberg, P. A., and Bourouaine, S. (2013). Stochastic Heating, Differential Flow, and the Alpha-to-proton Temperature Ratio in the Solar Wind. *Astrophys. J.*, 776(1):45.

Chandrasekhar, S., Kaufman, A. N., and Watson, K. M. (1958). The Stability of the Pinch. *Proceedings of the Royal Society of London Series A*, 245(1243):435–455.

Chasapis, A., Retinò, A., Sahraoui, F., Vaivads, A., Khotyaintsev, Y. V., Sundkvist, D., Greco, A., Sorriso-Valvo, L., and Canu, P. (2015). Thin Current Sheets and Associated Electron Heating in Turbulent Space Plasma. *Astrophys. J. Lett.*, 804(1):L1.

Chaston, C. C., Bonnell, J. W., Carlson, C. W., McFadden, J. P., Ergun, R. E., Strangeway, R. J., and Lund, E. J. (2004). Auroral ion acceleration in dispersive Alfvén waves. *Journal of Geophysical Research (Space Physics)*, 109(A4):A04205.

Chen, C. H. K., Bale, S. D., Bonnell, J. W., Borovikov, D., Bowen, T. A., Burgess, D., Case, A. W., Chandran, B. D. G., de Wit, T. D., Goetz, K., Harvey, P. R., Kasper, J. C., Klein, K. G., Korreck, K. E., Larson, D., Livi, R., MacDowall, R. J., Malaspina, D. M., Mallet, A., McManus, M. D., Moncuquet, M., Pulupa, M., Stevens, M. L., and Whittlesey, P. (2020). The Evolution and Role of Solar Wind Turbulence in the Inner Heliosphere. *Astrophys. J., Suppl. Ser.*, 246(2):53.

Chen, C. H. K., Horbury, T. S., Schekochihin, A. A., Wicks, R. T., Alexandrova, O., and Mitchell, J. (2010). Anisotropy of Solar Wind Turbulence between Ion and Electron Scales. *Phys. Rev. Lett.*, 104:255002–+.

Chen, C. H. K., Leung, L., Boldyrev, S., Maruca, B. A., and Bale, S. D. (2014). Ion-scale spectral break of solar wind turbulence at high and low beta. *Geophys. Res. Lett.*, 41(22):8081–8088.

Chhiber, R., Matthaeus, W. H., Bowen, T. A., and Bale, S. D. (2021). Subproton-scale intermittency in near-sun solar wind turbulence observed by the parker solar probe. *The Astrophysical Journal Letters*, 911(1):L7.

Coleman, Paul J., J. (1968). Turbulence, Viscosity, and Dissipation in the Solar-Wind Plasma. *Astrophys. J.*, 153:371.

Cranmer, S. R. (2000). Ion Cyclotron Wave Dissipation in the Solar Corona: The Summed Effect of More than 2000 Ion Species. *Astrophys. J.*, 532(2):1197–1208.

Cranmer, S. R., van Ballegooijen, A. A., and Edgar, R. J. (2007). Self-consistent Coronal Heating and Solar Wind Acceleration from Anisotropic Magnetohydrodynamic Turbulence. *Astrophys. J., Suppl. Ser.*, 171(2):520–551.

Cuesta, M. E., Chhiber, R., Fu, X., Du, S., Yang, Y., Pecora, F., Matthaeus, W. H., Li, H., Steinberg, J., Guo, F., Gan, Z., Conrad, E., and Swanson, D. (2023). Compressible Turbulence in the Near-Sun Solar Wind: Parker Solar Probe's First Eight Perihelia. *Astrophys. J. Lett.*, 949(2):L19.

Dakeyo, J.-B., Maksimovic, M., Démoulin, P., Halekas, J., and Stevens, M. L. (2022). Statistical Analysis of the Radial Evolution of the Solar Winds between 0.1 and 1 au and Their Semiempirical Isopoly Fluid Modeling. *Astrophys. J.*, 940(2):130.

D'Amicis, R., Matteini, L., and Bruno, R. (2019). On the slow solar wind with high Alfvénicity: from composition and microphysics to spectral properties. *Monthly Notices of the Royal Astronomical Society*, 483(4):4665–4677.

Dasgupta, B., Tsurutani, B. T., and Janaki, M. S. (2003). A kinetic approach to the Ponderomotive Force. *Geophys. Res. Lett.*, 30(21):2128.

Davis, M. S., Phan, T. D., Gosling, J. T., and Skoug, R. M. (2006). Detection of oppositely directed reconnection jets in a solar wind current sheet. *Geophys. Res. Lett.*, 33(19):L19102.

Denskat, K. U. and Neubauer, F. M. (1982). Statistical properties of low-frequency magnetic field fluctuations in the solar wind from 0.29 to 1.0 AU during solar minimum conditions: HELIOS 1 and HELIOS 2. *J. Geophys. Res.*, 87(A4):2215–2223.

Dobrowolny, M., Mangeney, A., and Veltri, P. (1980). Fully Developed Anisotropic Hydromagnetic Turbulence in Interplanetary Space. *Phys. Rev. Lett.*, 45(2):144–147.

Donato, S., Servidio, S., Dmitruk, P., Carbone, V., Shay, M. A., Cassak, P. A., and Matthaeus, W. H. (2012). Reconnection events in two-dimensional Hall magnetohydrodynamic turbulence. *Physics of Plasmas*, 19(9):092307.

Drake, J. F., Agapitov, O., Swisdak, M., Badman, S. T., Bale, S. D., Horbury, T. S., Kasper, J. C., MacDowall, R. J., Mozer, F. S., Phan, T. D., Pulupa, M., Szabo, A., and Velli, M. (2021). Switchbacks as signatures of magnetic flux ropes generated by interchange reconnection in the corona. *Astron. Astrophys.*, 650:A2.

Dudok de Wit, T., Alexandrova, O., Furno, I., Sorriso-Valvo, L., and Zimbardo, G. (2013). Methods for Characterising Microphysical Processes in Plasmas. *Space Sci. Rev.*, 178(2-4):665–693.

Dudok de Wit, T., Krasnoselskikh, V. V., Bale, S. D., Bonnell, J. W., Bowen, T. A., Chen, C. H. K., Froment, C., Goetz, K., Harvey, P. R., Jagarlamudi, V. K., Larosa, A., MacDowall, R. J., Malaspina, D. M., Matthaeus, W. H., Pulupa, M., Velli, M., and Whittlesey, P. L. (2020). Switchbacks in the Near-Sun Magnetic Field: Long Memory and Impact on the Turbulence Cascade. *Astrophys. J., Suppl. Ser.*, 246(2):39.

Elsasser, W. M. (1950). The Hydromagnetic Equations. *Physical Review*, 79(1):183–183.

Enžl, J., Přech, L., Šafránková, J., and Němeček, Z. (2014). Statistical Study of Reconnection Exhausts in the Solar Wind. *Astrophys. J.*, 796(1):21.

Enžl, J., Šafránková, J., Němeček, Z., and Přech, L. (2017). Spiky Structures around Reconnection Exhausts in the Solar Wind. *Astrophys. J.*, 851(2):86.

Eriksson, S., Swisdak, M., Weygand, J. M., Mallet, A., Newman, D. L., Lapenta, G., Wilson, Lynn B., I., Turner, D. L., and Larsen, B. (2022). Characteristics of Multi-scale Current Sheets in the Solar Wind at 1 au Associated with Magnetic Reconnection and the Case for a Heliospheric Current Sheet Avalanche. *Astrophys. J.*, 933(2):181.

Farge, M. (1992). Wavelet transforms and their applications to turbulence. *Annual Review of Fluid Mechanics*, 24:395–457.

Farge, M. and Schneider, K. (2015). Wavelet transforms and their applications to MHD and plasma turbulence: a review. *Journal of Plasma Physics*, 81(6).

Fargette, N., Lavraud, B., Rouillard, A. P., Houdayer, P. S., Phan, T. D., Øieroset, M., Eastwood, J. P., Nicolaou, G., Fedorov, A., Louarn, P., Owen, C. J., and Horbury, T. S. (2023). Clustering of magnetic reconnection exhausts in the solar wind: An automated detection study. *Astron. Astrophys.*, 674:A98.

Fedorov, A., Louarn, P., Owen, C. J., Horbury, T. S., Prech, L., Durovcova, T., Barthe, A., Rouillard, A. P., Kasper, J. C., Bale, S. D., Bruno, R., O'Brien, H., Evans, V., Angelini, V., Larson, D., Livi, R., Lavraud, B., Andre, N., Genot, V., Penou, E., Mele, G., and Fortunato, V. (2021). Switchback-like structures observed by Solar Orbiter. *Astron. Astrophys.*, 656:A40.

Fiedler, H. E. (1988). Coherent structures in turbulent flows. *Progress in Aerospace Sciences*, 25:231–269.

Frisch, U. (1995). *Turbulence. The legacy of A.N. Kolmogorov.*

Frisch, U., Pouquet, A., Sulem, P. L., and Meneguzzi, M. (1983). The dynamics of two-dimensional ideal MHD. *Journal de Mecanique Theorique et Appliquee Supplement*, pages 191–216.

Frisch, U., Sulem, P. L., and Nelkin, M. (1978). A simple dynamical model of intermittent fully developed turbulence. *Journal of Fluid Mechanics*, 87:719–736.

Froment, C., Krasnoselskikh, V., Dudok de Wit, T., Agapitov, O., Fargette, N., Lavraud, B., Larosa, A., Kretzschmar, M., Jagarlamudi, V. K., Velli, M., Malaspina, D., Whittlesey, P. L., Bale, S. D., Case, A. W., Goetz, K., Kasper, J. C., Korreck, K. E., Larson, D. E., MacDowall, R. J., Mozer, F. S., Pulupa, M., Revillet, C., and Stevens, M. L. (2021). Direct evidence for magnetic reconnection at the boundaries of magnetic switchbacks with Parker Solar Probe. *Astron. Astrophys.*, 650:A5.

Gary, S. P. and Borovsky, J. E. (2004). Alfvén-cyclotron fluctuations: Linear Vlasov theory. *Journal of Geophysical Research (Space Physics)*, 109(A6):A06105.

Goldreich, P. and Sridhar, S. (1995). Toward a Theory of Interstellar Turbulence. II. Strong Alfvenic Turbulence. *Astrophys. J.*, 438:763.

Gosling, J. T. (2007). Observations of Magnetic Reconnection in the Turbulent High-Speed Solar Wind. *Astrophys. J. Lett.*, 671(1):L73–L76.

Gosling, J. T., Skoug, R. M., McComas, D. J., and Smith, C. W. (2005). Direct evidence for magnetic reconnection in the solar wind near 1 AU. *Journal of Geophysical Research (Space Physics)*, 110(A1):A01107.

Grauer, R., Krug, J., and Marliani, C. (1994). Scaling of high-order structure functions in magnetohydrodynamic turbulence. *Physics Letters A*, 195(5-6):335–338.

Greco, A., Chuychai, P., Matthaeus, W. H., Servidio, S., and Dmitruk, P. (2008). Intermittent MHD structures and classical discontinuities. *Geophys. Res. Lett.*, 35(19):L19111.

Greco, A., Matthaeus, W. H., D'Amicis, R., Servidio, S., and Dmitruk, P. (2012). Evidence for Nonlinear Development of Magnetohydrodynamic Scale Intermittency in the Inner Heliosphere. *Astrophys. J.*, 749(2):105.

Greco, A., Matthaeus, W. H., Servidio, S., Chuychai, P., and Dmitruk, P. (2009). Statistical Analysis of Discontinuities in Solar Wind ACE Data and Comparison with Intermittent MHD Turbulence. *Astrophys. J. Lett.*, 691(2):L111–L114.

Greco, A., Perri, S., Servidio, S., Yordanova, E., and Veltri, P. (2016). The Complex Structure of Magnetic Field Discontinuities in the Turbulent Solar Wind. *Astrophys. J. Lett.*, 823(2):L39.

Green, M. J., Brown, R. A., and Armstrong, R. C. (2007). Nonhomogeneous shear flow in concentrated liquid-crystalline solutions. *Physics of Fluids*, 19(11):111702–111702–4.

Grošelj, D., Chen, C. H. K., Mallet, A., Samtaney, R., Schneider, K., and Jenko, F. (2019). Kinetic Turbulence in Astrophysical Plasmas: Waves and/or Structures? *Physical Review X*, 9(3):031037.

Hada, T., Koga, D., and Yamamoto, E. (2003). Phase coherence of MHD waves in the solar wind. *Space Sci. Rev.*, 107(1):463–466.

Hasegawa, A. (1969). Drift mirror instability of the magnetosphere. *Physics of Fluids*, 12:2642–2650.

Hasegawa, A. and Chen, L. (1976). Kinetic processes in plasma heating by resonant mode conversion of Alfvén wave. *Physics of Fluids*, 19(12):1924–1934.

Hellinger, P., Matteini, L., Štverák, Š., Trávníček, P. M., and Marsch, E. (2011). Heating and cooling of protons in the fast solar wind between 0.3 and 1 AU: Helios revisited. *Journal of Geophysical Research (Space Physics)*, 116(A9):A09105.

Hollweg, J. V. (1999). Kinetic Alfvén wave revisited. *J. Geophys. Res.*, 104(A7):14811–14820.

Hoppock, I. W., Chandran, B. D. G., Klein, K. G., Mallet, A., and Verscharen, D. (2018). Stochastic proton heating by kinetic-Alfvén-wave turbulence in moderately high-$\beta$ plasmas. *Journal of Plasma Physics*, 84(6):905840615.

Horbury, T. S. and Balogh, A. (1997). Structure function measurements of the intermittent MHD turbulent cascade. *Nonlinear Processes in Geophysics*, 4(3):185–199.

Horbury, T. S., Forman, M., and Oughton, S. (2008). Anisotropic Scaling of Magnetohydrodynamic Turbulence. *Phys. Rev. Lett.*, 101(17):175005.

Howes, G. G., Cowley, S. C., Dorland, W., Hammett, G. W., Quataert, E., and Schekochihin, A. A. (2006). Astrophysical Gyrokinetics: Basic Equations and Linear Theory. *Astrophys. J.*, 651(1):590–614.

Howes, G. G., Klein, K. G., and TenBarge, J. M. (2014). Validity of the Taylor Hypothesis for Linear Kinetic Waves in the Weakly Collisional Solar Wind. *Astrophys. J.*, 789(2):106.

Hudson, P. D. (1970). Discontinuities in an anisotropic plasma and their identification in the solar wind. *Planetary Spa. Sci.*, 18(11):1611–1622.

Hussain, A. K. M. F. (1986). Coherent structures and turbulence. *Journal of Fluid Mechanics*, 173:303–356.

Iroshnikov, P. S. (1963). Turbulence of a Conducting Fluid in a Strong Magnetic Field. *Astronomicheskii Zhurnal*, 40:742.

Jiménez, J., Wray, A. A., Saffman, P. G., and Rogallo, R. S. (1993). The structure of intense vorticity in isotropic turbulence. *Journal of Fluid Mechanics*, 255:65–90.

Johnson, J. R. and Cheng, C. Z. (2001). Stochastic ion heating at the magnetopause due to kinetic Alfvén waves. *Geophys. Res. Lett.*, 28(23):4421–4424.

Jovanović, D., Alexandrova, O., Maksimović, M., and Belić, M. (2020). Fluid Theory of Coherent Magnetic Vortices in High-$\beta$ Space Plasmas. *Astrophys. J.*, 896(1):8.

Jovanović, D., Alexandrova, O., and Maksimović, M. (2015). Theory of coherent electron-scale magnetic structures in space plasma turbulence. *Physica Scripta*, 90(8):088002.

Kadomtsev, B. B. and Pogutse, O. P. (1974). Nonlinear helical perturbations of a plasma in the tokamak. *Soviet Journal of Experimental and Theoretical Physics*, 38:283–290.

Karimabadi, H., Roytershteyn, V., Wan, M., Matthaeus, W. H., Daughton, W., Wu, P., Shay, M., Loring, B., Borovsky, J., Leonardis, E., Chapman, S. C., and Nakamura, T. K. M. (2013). Coherent structures, intermittent turbulence, and dissipation in high-temperature plasmas. *Physics of Plasmas*, 20(1):012303.

Karlsson, T., Heyner, D., Volwerk, M., Morooka, M., Plaschke, F., Goetz, C., and Hadid, L. (2021). Magnetic Holes in the Solar Wind and Magnetosheath Near Mercury. *Journal of Geophysical Research (Space Physics)*, 126(5):e28961.

Kasper, J. C., Bale, S. D., Belcher, J. W., Berthomier, M., Case, A. W., Chandran, B. D. G., Curtis, D. W., Gallagher, D., Gary, S. P., Golub, L., Halekas, J. S., Ho, G. C., Horbury, T. S., Hu, Q., Huang, J., Klein, K. G., Korreck, K. E., Larson, D. E., Livi, R., Maruca, B., Lavraud, B., Louarn, P., Maksimovic, M., Martinovic, M., McGinnis, D., Pogorelov, N. V., Richardson, J. D., Skoug, R. M., Steinberg, J. T., Stevens, M. L., Szabo, A., Velli, M., Whittlesey, P. L., Wright, K. H., Zank, G. P., MacDowall, R. J., McComas, D. J., McNutt, R. L., Pulupa, M., Raouafi, N. E., and Schwadron, N. A. (2019). Alfvénic velocity spikes and rotational flows in the near-Sun solar wind. *Nature*, 576(7786):228–231.

Kiyani, K. H., Chapman, S. C., Khotyaintsev, Y. V., Dunlop, M. W., and Sahraoui, F. (2009). Global Scale-Invariant Dissipation in Collisionless Plasma Turbulence. *Phys. Rev. Lett.*, 103(7):075006.

Kiyani, K. H., Osman, K. T., and Chapman, S. C. (2015). Dissipation and heating in solar wind turbulence: from the macro to the micro and back again. *Philosophical Transactions of the Royal Society of London Series A*, 373(2041):20140155–20140155.

Koga, D. and Hada, T. (2003). Phase coherence of foreshock MHD waves: wavelet analysis. *Space Sci. Rev.*, 107(1):495–498.

Kolmogorov, A. (1941). The Local Structure of Turbulence in Incompressible Viscous Fluid for Very Large Reynolds' Numbers. *Akademiia Nauk SSSR Doklady*, 30:301–305.

Kolmogorov, A. N. (1962). A refinement of previous hypotheses concerning the local structure of turbulence in a viscous incompressible fluid at high Reynolds number. *Journal of Fluid Mechanics*, 13:82–85.

Kraichnan, R. H. (1965). Inertial-Range Spectrum of Hydromagnetic Turbulence. *Physics of Fluids*, 8(7):1385–1387.

Krasnoselskikh, V., Larosa, A., Agapitov, O., de Wit, T. D., Moncuquet, M., Mozer, F. S., Stevens, M., Bale, S. D., Bonnell, J., Froment, C., Goetz, K., Goodrich, K., Harvey, P., Kasper, J., MacDowall, R., Malaspina, D., Pulupa, M., Raouafi, N., Revillet, C., Velli, M., and Wygant, J. (2020). Localized Magnetic-field Structures and Their Boundaries in the Near-Sun Solar Wind from Parker Solar Probe Measurements. *Astrophys. J.*, 893(2):93.

Kumar, P. (1994). *Wavelets in Geophysics.*

Lacombe, C., Alexandrova, O., and Matteini, L. (2017). Anisotropies of the Magnetic Field Fluctuations at Kinetic Scales in the Solar Wind: Cluster Observations. *Astrophys. J.*, 848(1):45.

Landau, L., Lifshitz, E., and Pitaevskii, L. (1995). *Electrodynamics of Continuous Media: Volume 8*. Course of theoretical physics. Elsevier Science.

Landi, S., Hellinger, P., and Velli, M. (2006). Heliospheric magnetic field polarity inversions driven by radial velocity field structures. *Geophys. Res. Lett.*, 33(14):L14101.

Larichev, V. and Reznik, G. (1976). Two-dimensional solitary rossby waves. *Doklady Akademii nauk SSSR*, 231:1077–1079.

Leamon, R. J., Smith, C. W., Ness, N. F., Matthaeus, W. H., and Wong, H. K. (1998). Observational constraints on the dynamics of the interplanetary magnetic field dissipation range. *J. Geophys. Res.*, 103(A3):4775–4788.

Leamon, R. J., Smith, C. W., Ness, N. F., and Wong, H. K. (1999). Dissipation range dynamics: Kinetic Alfvén waves and the importance of $\beta_e$. *J. Geophys. Res.*, 104(A10):22331–22344.

Lion, S., Alexandrova, O., and Zaslavsky, A. (2016). Coherent Events and Spectral Shape at Ion Kinetic Scales in the Fast Solar Wind Turbulence. *Astrophys. J.*, 824(1):47.

Lithwick, Y., Goldreich, P., and Sridhar, S. (2007). Imbalanced Strong MHD Turbulence. *Astrophys. J.*, 655(1):269–274.

Lotekar, A. B., Vasko, I. Y., Phan, T., Bale, S. D., Bowen, T. A., Halekas, J., Artemyev, A. V., Khotyaintsev, Y. V., and Mozer, F. S. (2022). Kinetic-scale Current Sheets in Near-Sun Solar Wind: Properties, Scale-dependent Features and Reconnection Onset. *Astrophys. J.*, 929(1):58.

Mangeney, A. (2001). Intermittency in the Solar Wind Turbulence and the Haar Wavelet Transform. In Warmbein, B., editor, *Sheffield Space Plasma Meeting: Multipoint Measurements versus Theory*, volume 492 of *ESA Special Publication*, page 53.

Mangeney, A., Grappin, R., and Velli, M. (1991). MHD turbulence in the solar wind. In *Geophysical and Astrophysical MHD*, pages 327–356.

Marsch, E. and Tu, C. Y. (1997). Intermittency, non-Gaussian statistics and fractal scaling of MHD fluctuations in the solar wind¡/a¿. *Nonlinear Processes in Geophysics*, 4(2):101–124.

Matteini, L., Franci, L., Alexandrova, O., Lacombe, C., Landi, S., Hellinger, P., Papini, E., and Verdini, A. (2020). Magnetic field turbulence in the solar wind at sub-ion scales: in situ observations and numerical simulations. *Frontiers in Astronomy and Space Sciences*, 7:83.

Matteini, L., Horbury, T. S., Neugebauer, M., and Goldstein, B. E. (2014). Dependence of solar wind speed on the local magnetic field orientation: Role of Alfvénic fluctuations. *Geophys. Res. Lett.*, 41(2):259–265.

Matteini, L., Stansby, D., Horbury, T. S., and Chen, C. H. K. (2019). The rotation angle distribution underlying magnetic field fluctuations in the 1/ f range of solar wind turbulent spectra. *Nuovo Cimento C Geophysics Space Physics C*, 42(1):16.

Matthaeus, W. H., Dasso, S., Weygand, J. M., Milano, L. J., Smith, C. W., and Kivelson, M. G. (2005). Spatial Correlation of Solar-Wind Turbulence from Two-Point Measurements. *Phys. Rev. Lett.*, 95(23):231101.

Matthaeus, W. H. and Goldstein, M. L. (1982). Measurement of the rugged invariants of magnetohydrodynamic turbulence in the solar wind. *J. Geophys. Res.*, 87(A8):6011–6028.

Matthaeus, W. H. and Goldstein, M. L. (1986). Low-frequency 1/f noise in the interplanetary magnetic field. *Phys. Rev. Lett.*, 57(4):495–498.

Matthaeus, W. H. and Montgomery, D. (1980). Selective decay hypothesis at high mechanical and magnetic Reynolds numbers. *Annals of the New York Academy of Sciences*, 357:203–222.

Matthaeus, W. H. and Velli, M. (2011). Who Needs Turbulence?. A Review of Turbulence Effects in the Heliosphere and on the Fundamental Process of Reconnection. *Space Sci. Rev.*, 160(1-4):145–168.

Matthaeus, W. H., Wan, M., Servidio, S., Greco, A., Osman, K. T., Oughton, S., and Dmitruk, P. (2015). Intermittency, nonlinear dynamics and dissipation in the solar wind and astrophysical plasmas. *Philosophical Transactions of the Royal Society of London Series A*, 373(2041):20140154–20140154.

McChesney, J. M., Stern, R. A., and Bellan, P. M. (1987). Observation of fast stochastic ion heating by drift waves. *Phys. Rev. Lett.*, 59(13):1436–1439.

McComas, D. J., Ebert, R. W., Elliott, H. A., Goldstein, B. E., Gosling, J. T., Schwadron, N. A., and Skoug, R. M. (2008). Weaker solar wind from the polar coronal holes and the whole Sun. *Geophys. Res. Lett.*, 35(18):L18103.

Meneveau, C. and Sreenivasan, K. R. (1987). Simple multifractal cascade model for fully developed turbulence. *Phys. Rev. Lett.*, 59(13):1424–1427.

Meyrand, R., Squire, J., Mallet, A., and Chandran, B. D. G. (2023). Reflection-driven turbulence in the super-alfvénic solar wind.

Mininni, P., Lee, E., Norton, A., and Clyne, J. (2008). Flow visualization and field line advection in computational fluid dynamics: application to magnetic fields and turbulent flows. *New Journal of Physics*, 10(12):125007.

Mininni, P. D., Pouquet, A. G., and Montgomery, D. C. (2006). Small-Scale Structures in Three-Dimensional Magnetohydrodynamic Turbulence. *Phys. Rev. Lett.*, 97(24):244503.

Mistry, R., Eastwood, J. P., Phan, T. D., and Hietala, H. (2015). Development of bifurcated current sheets in solar wind reconnection exhausts. *Geophys. Res. Lett.*, 42(24):10,513–10,520.

Mistry, R., Eastwood, J. P., Phan, T. D., and Hietala, H. (2017). Statistical properties of solar wind reconnection exhausts. *Journal of Geophysical Research (Space Physics)*, 122(6):5895–5909.

Neugebauer, M. (2006). Comment on the abundances of rotational and tangential discontinuities in the solar wind. *Journal of Geophysical Research (Space Physics)*, 111(A4):A04103.

Neugebauer, M. and Goldstein, B. E. (2013). Double-proton beams and magnetic switchbacks in the solar wind. In Zank, G. P., Borovsky, J., Bruno, R., Cirtain, J., Cranmer, S., Elliott, H., Giacalone, J., Gonzalez, W., Li, G., Marsch, E., Moebius, E., Pogorelov, N., Spann, J., and Verkhoglyadova, O., editors, *Solar Wind 13*, volume 1539 of *American Institute of Physics Conference Series*, pages 46–49.

Osman, K. T., Matthaeus, W. H., Greco, A., and Servidio, S. (2011). Evidence for Inhomogeneous Heating in the Solar Wind. *Astrophys. J. Lett.*, 727(1):L11.

Oughton, S. and Matthaeus, W. H. (2020). Critical Balance and the Physics of Magnetohydrodynamic Turbulence. *Astrophys. J.*, 897(1):37.

Papini, E., Cicone, A., Franci, L., Piersanti, M., Landi, S., Hellinger, P., and Verdini, A. (2021). Spacetime Hall-MHD Turbulence at Sub-ion Scales: Structures or Waves? *Astrophys. J. Lett.*, 917(1):L12.

Papini, E., Franci, L., Cicone, A., Verdini, A., Montagud-Camps, V., Hellinger, P., Piersanti, M., and Landi, S. (2022). Spacetime structure of plasma turbulence in 3D Hall-MHD and Hybrid-kinetic numerical simulations. In *AGU Fall Meeting Abstracts*, volume 2022, pages SH33A–07.

Parker, E. N. (1958). Dynamics of the Interplanetary Gas and Magnetic Fields. *Astrophys. J.*, 128:664.

Perez, J. C. and Boldyrev, S. (2009). Role of Cross-Helicity in Magnetohydrodynamic Turbulence. *Phys. Rev. Lett.*, 102(2):025003.

Perri, S., Goldstein, M. L., Dorelli, J. C., and Sahraoui, F. (2012). Detection of Small-Scale Structures in the Dissipation Regime of Solar-Wind Turbulence. *Phys. Rev. Lett.*, 109(19):191101.

Perrone, D., Alexandrova, O., Mangeney, A., Maksimovic, M., Lacombe, C., Rakoto, V., Kasper, J. C., and Jovanovic, D. (2016). Compressive Coherent Structures at Ion Scales in the Slow Solar Wind. *Astrophys. J.*, 826(2):196.

Perrone, D., Alexandrova, O., Roberts, O. W., Lion, S., Lacombe, C., Walsh, A., Maksimovic, M., and Zouganelis, I. (2017). Coherent Structures at Ion Scales in Fast Solar Wind: Cluster Observations. *Astrophys. J.*, 849(1):49.

Perrone, D., Bruno, R., D'Amicis, R., Telloni, D., De Marco, R., Stangalini, M., Perri, S., Pezzi, O., Alexandrova, O., and Bale, S. D. (2020). Coherent Events at Ion Scales in the Inner Heliosphere: Parker Solar Probe Observations during the First Encounter. *Astrophys. J.*, 905(2):142.

Petviashvili, V. and Pokhotelov, O. (1992). *Solitary waves in plasmas and in the atmosphere.*

Phan, T. D., Bale, S. D., Eastwood, J. P., Lavraud, B., Drake, J. F., Oieroset, M., Shay, M. A., Pulupa, M., Stevens, M., MacDowall, R. J., Case, A. W., Larson, D., Kasper, J., Whittlesey, P., Szabo, A., Korreck, K. E., Bonnell, J. W., de Wit, T. D., Goetz, K., Harvey, P. R., Horbury, T. S., Livi, R., Malaspina, D., Paulson, K., Raouafi, N. E., and Velli, M. (2020). Parker Solar Probe In Situ Observations of Magnetic Reconnection Exhausts during Encounter 1. *Astrophys. J., Suppl. Ser.*, 246(2):34.

Phan, T. D., Gosling, J. T., Davis, M. S., Skoug, R. M., Øieroset, M., Lin, R. P., Lepping, R. P., McComas, D. J., Smith, C. W., Reme, H., and Balogh, A. (2006). A magnetic reconnection X-line extending more than 390 Earth radii in the solar wind. *Nature*, 439(7073):175–178.

Phan, T. D., Gosling, J. T., Paschmann, G., Pasma, C., Drake, J. F., Øieroset, M., Larson, D., Lin, R. P., and Davis, M. S. (2010). The Dependence of Magnetic Reconnection on Plasma $\beta$ and Magnetic Shear: Evidence from Solar Wind Observations. *Astrophys. J. Lett.*, 719(2):L199–L203.

Podesta, J. J. (2009). Dependence of Solar-Wind Power Spectra on the Direction of the Local Mean Magnetic Field. *Astrophys. J.*, 698(2):986–999.

Podesta, J. J. (2017). The most intense current sheets in the high-speed solar wind near 1 AU. *Journal of Geophysical Research (Space Physics)*, 122(3):2795–2823.

Podesta, J. J., Roberts, D. A., and Goldstein, M. L. (2007). Spectral Exponents of Kinetic and Magnetic Energy Spectra in Solar Wind Turbulence. *Astrophys. J.*, 664(1):543–548.

Pouquet, A., Frisch, U., and Leorat, J. (1976). Strong MHD helical turbulence and the nonlinear dynamo effect. *Journal of Fluid Mechanics*, 77:321–354.

Richardson, L. F. (1922). *Weather prediction by Numerical Process*. Cambridge University Press.

Roberts, D. A. (2010). Evolution of the spectrum of solar wind velocity fluctuations from 0.3 to 5 AU. *Journal of Geophysical Research (Space Physics)*, 115(A12):A12101.

Roberts, D. A., Klein, L. W., Goldstein, M. L., and Matthaeus, W. H. (1987). The nature and evolution of magnetohydrodynamic fluctuations in the solar wind: Voyager observations. *J. Geophys. Res.*, 92(A10):11021–11040.

Roberts, O. W., Li, X., Alexandrova, O., and Li, B. (2016). Observation of an MHD Alfvén vortex in the slow solar wind. *Journal of Geophysical Research (Space Physics)*, 121(5):3870–3881.

Rouillard, A. P., Viall, N., Pierrard, V., Vocks, C., Matteini, L., Alexandrova, O., Higginson, A. K., Lavraud, B., Lavarra, M., Wu, Y., Pinto, R., Bemporad, A., and Sanchez-Diaz, E. (2021). *The Solar Wind*, chapter 1, pages 1–33. American Geophysical Union (AGU).

Ruffolo, D., Matthaeus, W. H., Chhiber, R., Usmanov, A. V., Yang, Y., Bandyopadhyay, R., Parashar, T. N., Goldstein, M. L., DeForest, C. E., Wan, M., Chasapis, A., Maruca, B. A., Velli, M., and Kasper, J. C. (2020). Shear-driven Transition to Isotropically Turbulent Solar Wind Outside the Alfvén Critical Zone. *Astrophys. J.*, 902(2):94.

Ruzmaikin, A. A., Feynman, J., Goldstein, B. E., Smith, E. J., and Balogh, A. (1995). Intermittent turbulence in solar wind from the south polar hole. *J. Geophys. Res.*, 100(A3):3395–3404.

Sahraoui, F., Goldstein, M. L., Robert, P., and Khotyaintsev, Y. V. (2009). Evidence of a cascade and dissipation of solar-wind turbulence at the electron gyroscale. *Phys. Rev. Lett.*, 102:231102.

Sahraoui, F., Huang, S. Y., Belmont, G., Goldstein, M. L., Rétino, A., Robert, P., and De Patoul, J. (2013). Scaling of the Electron Dissipation Range of Solar Wind Turbulence. *Astrophys. J.*, 777(1):15.

Salem, C. (2000). *Ondes, turbulence et phenomenes dissipatifs dans le vent solaire a partir des observations de la sonde Wind*. PhD thesis. Thèse de doctorat dirigée par André Mangeney; Terre, océan, espace. Physique Paris 7 2000.

Salem, C., Mangeney, A., Bale, S. D., and Veltri, P. (2009). Solar Wind Magnetohydrodynamics Turbulence: Anomalous Scaling and Role of Intermittency. *Astrophys. J.*, 702(1):537–553.

Salem, C., Mangeney, A., Bale, S. D., Veltri, P., and Bruno, R. (2007). Anomalous scaling and the role of intermittency in solar wind MHD turbulence: new insights. In Shaikh, D. and Zank, G. P., editors, *Turbulence and Nonlinear Processes in Astrophysical Plasmas*, volume 932 of *American Institute of Physics Conference Series*, pages 75–82.

Salem, C. S., Howes, G. G., Sundkvist, D., Bale, S. D., Chaston, C. C., Chen, C. H. K., and Mozer, F. S. (2012). Identification of Kinetic Alfvén Wave Turbulence in the Solar Wind. *Astrophys. J. Lett.*, 745(1):L9.

Schekochihin, A. A. (2020). MHD Turbulence: A Biased Review. *arXiv e-prints*, page arXiv:2010.00699.

Schekochihin, A. A., Cowley, S. C., Dorland, W., Hammett, G. W., Howes, G. G., Quataert, E., and Tatsuno, T. (2009). Astrophysical Gyrokinetics: Kinetic and Fluid Turbulent Cascades in Magnetized Weakly Collisional Plasmas. *Astrophys. J., Suppl. Ser.*, 182(1):310–377.

Schmekel, D., Alcántara-Ávila, F., Hoyas, S., and Vinuesa, R. (2022). Predicting coherent turbulent structures via deep learning. *Frontiers in Physics*, 10.

Schwadron, N. A. and McComas, D. J. (2021). Switchbacks Explained: Super-Parker Fields—The Other Side of the Sub-Parker Spiral. *Astrophys. J.*, 909(1):95.

Servidio, S., Matthaeus, W. H., and Dmitruk, P. (2008). Depression of Nonlinearity in Decaying Isotropic MHD Turbulence. *Phys. Rev. Lett.*, 100(9):095005.

She, Z.-S. and Leveque, E. (1994). Universal scaling laws in fully developed turbulence. *Phys. Rev. Lett.*, 72(3):336–339.

Sioulas, N., Shi, C., Huang, Z., and Velli, M. (2022). Preferential Heating of Protons over Electrons from Coherent Structures during the First Perihelion of the Parker Solar Probe. *Astrophys. J. Lett.*, 935(2):L29.

Smith, C. W. and Vasquez, B. J. (2021). Driving and Dissipation of Solar-Wind Turbulence: What Is the Evidence? *Frontiers in Astronomy and Space Sciences*, 7:114.

Söding, A., Neubauer, F. M., Tsurutani, B. T., Ness, N. F., and Lepping, R. P. (2001). Radial and latitudinal dependencies of discontinuities in the solar wind between 0.3 and 19 AU and -80° and +10°. *Annales Geophysicae*, 19(7):667–680.

Sonnerup, B. U. Ö. and Scheible, M. (1998). Minimum and Maximum Variance Analysis. *ISSI Scientific Reports Series*, 1:185–220.

Sorriso-Valvo, L., Carbone, V., Veltri, P., Consolini, G., and Bruno, R. (1999). Intermittency in the solar wind turbulence through probability distribution functions of fluctuations. *Geophys. Res. Lett.*, 26(13):1801–1804.

Southwood, D. J. and Kivelson, M. G. (1993). Mirror instability. I - Physical mechanism of linear instability. *J. Geophys. Res.*, 98(A6):9181–9187.

Squire, J., Chandran, B. D. G., and Meyrand, R. (2020). In-situ Switchback Formation in the Expanding Solar Wind. *Astrophys. J. Lett.*, 891(1):L2.

Stevens, M. L. and Kasper, J. C. (2007). A scale-free analysis of magnetic holes at 1 AU. *Journal of Geophysical Research (Space Physics)*, 112(A5):A05109.

Strauss, H. R. (1976). Nonlinear, three-dimensional magnetohydrodynamics of noncircular tokamaks. *Physics of Fluids*, 19(1):134–140.

Sulem, P. L., Frisch, U., Pouquet, A., and Meneguzzi, M. (1985). On the exponential flattening of current sheets near neutral X-points in two-dimensional ideal MHD flow. *Journal of Plasma Physics*, 33(2):191–198.

Sundberg, T., Burgess, D., and Haynes, C. T. (2015). Properties and origin of subproton-scale magnetic holes in the terrestrial plasma sheet. *Journal of Geophysical Research (Space Physics)*, 120(4):2600–2615.

Taylor, G. I. (1938). The Spectrum of Turbulence. *Proceedings of the Royal Society of London Series A*, 164(919):476–490.

Tenerani, A., Velli, M., Matteini, L., Réville, V., Shi, C., Bale, S. D., Kasper, J. C., Bonnell, J. W., Case, A. W., de Wit, T. D., Goetz, K., Harvey, P. R., Klein, K. G., Korreck, K., Larson, D., Livi, R., MacDowall, R. J., Malaspina, D. M., Pulupa, M., Stevens, M., and Whittlesey, P. (2020). Magnetic Field Kinks and Folds in the Solar Wind. *Astrophys. J., Suppl. Ser.*, 246(2):32.

Tilquin, H., Eastwood, J. P., and Phan, T. D. (2020). Solar Wind Reconnection Exhausts in the Inner Heliosphere Observed by Helios and Detected via Machine Learning. *Astrophys. J.*, 895(1):68.

Torrence, C. and Compo, G. P. (1998). A Practical Guide to Wavelet Analysis. *Bulletin of the American Meteorological Society*, 79(1):61–78.

Tsurutani, B. T., Dasgupta, B., Galvan, C., Neugebauer, M., Lakhina, G. S., Arballo, J. K., Winterhalter, D., Goldstein, B. E., and Buti, B. (2002). Phase-steepened alfvén waves, proton perpendicular energization and the creation of magnetic holes and magnetic decreases: The ponderomotive force. *Geophysical Research Letters*, 29(24):86–1–86–4.

Tsurutani, B. T., Lakhina, G. S., Verkhoglyadova, O. P., Gonzalez, W. D., Echer, E., and Guarnieri, F. L. (2011). A review of interplanetary discontinuities and their geomagnetic effects. *Journal of Atmospheric and Solar-Terrestrial Physics*, 73(1):5–19.

Tsurutani, B. T. and Smith, E. J. (1979). Interplanetary discontinuities: Temporal variations and the radial gradient from 1 to 8.5 AU. *J. Geophys. Res.*, 84(A6):2773–2787.

Tsurutani, B. T., Southwood, D. J., Smith, E. J., and Balogh, A. (1992). Nonlinear magnetosonic waves and mirror mode structures in the March 1991 Ulysses interplanetary event. *Geophys. Res. Lett.*, 19(12):1267–1270.

Turner, J. M., Burlaga, L. F., Ness, N. F., and Lemaire, J. F. (1977). Magnetic holes in the solar wind. *J. Geophys. Res.*, 82(13):1921.

van Dyke, M. (1982). *An album of fluid motion.*

Vasko, I. Y., Alimov, K., Phan, T., Bale, S. D., Mozer, F. S., and Artemyev, A. V. (2022). Kinetic-scale Current Sheets in the Solar Wind at 1 au: Scale-dependent Properties and Critical Current Density. *Astrophys. J. Lett.*, 926(2):L19.

Vasquez, B. J., Abramenko, V. I., Haggerty, D. K., and Smith, C. W. (2007a). Numerous small magnetic field discontinuities of Bartels rotation 2286 and the potential role of Alfvénic turbulence. *Journal of Geophysical Research (Space Physics)*, 112(A11):A11102.

Vasquez, B. J., Smith, C. W., Hamilton, K., MacBride, B. T., and Leamon, R. J. (2007b). Evaluation of the turbulent energy cascade rates from the upper inertial range in the solar wind at 1 AU. *Journal of Geophysical Research (Space Physics)*, 112(A7):A07101.

Vech, D., Klein, K. G., and Kasper, J. C. (2017). Nature of Stochastic Ion Heating in the Solar Wind: Testing the Dependence on Plasma Beta and Turbulence Amplitude. *Astrophys. J. Lett.*, 850(1):L11.

Vedenov, A. A. and Sagdeev, R. Z. (1961). Some properties of a plasma with an anisotropic ion velocity distribution in a magnetic field. In Leontovich, M. A., editor, *Plasma Physics and the Problem of Controlled Thermonuclear Reactions, Volume 3*, volume 3, page 332.

Velli, M., Grappin, R., and Mangeney, A. (1989). Turbulent cascade of incompressible unidirectional Alfvén waves in the interplanetary medium. *Phys. Rev. Lett.*, 63(17):1807–1810.

Veltri, P. (1999). MHD turbulence in the solar wind: self-similarity, intermittency and coherent structures. *Plasma Physics and Controlled Fusion*, 41(3A):A787–A795.

Verdini, A., Grappin, R., Pinto, R., and Velli, M. (2012). On the Origin of the 1/f Spectrum in the Solar Wind Magnetic Field. *Astrophys. J. Lett.*, 750(2):L33.

Verkhoglyadova, O. P., Dasgupta, B., and Tsurutani, B. T. (2003). Model for vortex turbulence with discontinuities in the solar wind. *Nonlinear Processes in Geophysics*, 10:335–343.

Vincent, A. and Meneguzzi, M. (1991). The spatial structure and statistical properties of homogeneous turbulence. *Journal of Fluid Mechanics*, 225:1–20.

Vinogradov, A., Alexandrova, O., Démoulin, P., Artemyev, A., Maksimovic, M., Mangeney, A., Vasiliev, A., Petrukovich, A., and Bale, S. (2023). Embedded coherent structures from mhd to sub-ion scales in turbulent solar wind at 0.17 au.

Voitenko, Y. and Goossens, M. (2004). Cross-Field Heating of Coronal Ions by Low-Frequency Kinetic Alfvén Waves. *Astrophys. J. Lett.*, 605(2):L149–L152.

Volwerk, M., Goetz, C., Plaschke, F., Karlsson, T., Heyner, D., and Anderson, B. (2020). On the magnetic characteristics of magnetic holes in the solar wind between Mercury and Venus. *Annales Geophysicae*, 38(1):51–60.

Wan, M., Oughton, S., Servidio, S., and Matthaeus, W. H. (2009). Generation of non-Gaussian statistics and coherent structures in ideal magnetohydrodynamics. *Physics of Plasmas*, 16(8):080703.

Wang, G. Q., Zhang, T. L., Xiao, S. D., Wu, M. Y., Wang, G., Liu, L. J., Chen, Y. Q., and Volwerk, M. (2020). Statistical Properties of Sub-Ion Magnetic Holes in the Solar Wind at 1 AU. *Journal of Geophysical Research (Space Physics)*, 125(10):e28320.

Wang, T., Alexandrova, O., Perrone, D., Dunlop, M., Dong, X., Bingham, R., Khotyaintsev, Y. V., Russell, C. T., Giles, B. L., Torbert, R. B., Ergun, R. E., and Burch, J. L. (2019). Magnetospheric Multiscale Observation of Kinetic Signatures in the Alfvén Vortex. *Astrophys. J. Lett.*, 871(2):L22.

Wang, X., Chapman, S. C., Dendy, R. O., and Hnat, B. (2023). Wavelet determination of magnetohydrodynamic range power spectral exponents in solar wind turbulence seen by Parker Solar Probe. *Astron. Astrophys.*, page in press.

Wicks, R. T., Horbury, T. S., Chen, C. H. K., and Schekochihin, A. A. (2010). Power and spectral index anisotropy of the entire inertial range of turbulence in the fast solar wind. *Monthly Notices of the Royal Astronomical Society*, 407(1):L31–L35.

Winterhalter, D., Neugebauer, M., Goldstein, B. E., Smith, E. J., Bame, S. J., and Balogh, A. (1994). Ulysses field and plasma observations of magnetic holes in the solar wind and their relation to mirror-mode structures. *J. Geophys. Res.*, 99(A12):23371–23382.

Wu, P., Perri, S., Osman, K., Wan, M., Matthaeus, W. H., Shay, M. A., Goldstein, M. L., Karimabadi, H., and Chapman, S. (2013). Intermittent Heating in Solar Wind and Kinetic Simulations. *Astrophys. J. Lett.*, 763(2):L30.

Yamauchi, Y., Moore, R. L., Suess, S. T., Wang, H., and Sakurai, T. (2004). The Magnetic Structure of H$\alpha$ Macrospicules in Solar Coronal Holes. *Astrophys. J.*, 605(1):511–520.

Zank, G. P., Nakanotani, M., Zhao, L. L., Adhikari, L., and Kasper, J. (2020). The Origin of Switchbacks in the Solar Corona: Linear Theory. *Astrophys. J.*, 903(1):1.

Zhdankin, V., Boldyrev, S., Mason, J., and Perez, J. C. (2012). Magnetic Discontinuities in Magnetohydrodynamic Turbulence and in the Solar Wind. *Phys. Rev. Lett.*, 108(17):175004.

Zhou, Y., Tsang, W. K., and Antonia, R. A. (1999). Vortical structures in a turbulent far-wake: effect of Reynolds number. *Fluid Dynamics Research*, 25(6):293–314.